Design and Implementation of a Wide-Input Reconfigurable Three-Level Dual Active Bridge Converter for High-Voltage On-Board Charging Applications

Design and Implementation of a Wide-Input Reconfigurable Three-Level Dual Active Bridge Converter for High-Voltage On-Board Charging Applications

By Rachit Pradhan, B.E.

A Thesis
Submitted to the Department of Electrical & Computer Engineering
and the School of Graduate Studies in Partial Fulfillment of the Requirements for the Degree of
Master of Applied Science

McMaster University

M.A.Sc (2023)

Hamilton, Ontario (Electrical and Computer Engineering)

TITLE: Design and Implementation of a Wide-Input Reconfigurable Three-Level Dual Active Bridge Converter for High-Voltage On-Board Charging Applications

AUTHOR: Rachit Pradhan

B.E. (Electronics), University of Mumbai, Mumbai, India

SUPERVISOR: Dr. Ali Emadi

Ph.D, Texas A&M University, U.S.A

Fellow, IEEE, SAE, and NAI

NUMBER OF PAGES: xxi, 132

To My Family

Abstract

A high degree of electrification in vehicles results in a reduced carbon-dioxide equivalent (CO_{2e}) footprint. Battery Electric Vehicle (BEV)s encompass the highest degree of electrification, which aids in a reduced global carbon footprint from transportation related Greenhouse Gas (GHG) emissions. Mass-manufactured commercial BEVs have their powertrain voltage levels set between 400 - 800 V. Increasing the powertrain voltages provide benefits such as lower DC fast charging times, lower runtime conduction losses in the powertrain, and thus higher runtime efficiency. One of the latest commercially available BEV, Lucid Air Dream, has a maximum powertrain voltage of 924 V, which is close to the limit of the Combined Charging System (CCS) connector, at 1 kV, and exhibits saturation of the powertrain voltage towards this limit.

Medium- and Heavy-Duty Vehicles (MHDV) requiring higher traction powers and a low DC fast charging time would penetrate the BEV market over time. Futuristic DC fast charging standards such as Megawatt Charging System (MCS) (1.25 kV/ 3000 A/ 3.75 MW) and ChaoJi/CHAdeMO 3.0 (1.5 kV/ 600 A/ 900 kW) have been introduced to harmonize the DC fast charging of MHDVs. In North America, the SAE J3068 standard has been proposed for three-phase AC, or Level 3 AC charging up to 166 kW. The North American power grid does not have an homogenous voltage, and has a range of 208 - 600 V in Canada, 220 - 480 V in Mexico, an 208 - 480 V in the United States of America. This encompasses the recommended voltage level by the SAE J3068 standard. With heavy economic dependency of cross-border freight within the country, it is important for Original Equipment Manufacturer (OEM)s to support on-board charging for a wide

AC input voltage range of 208 - 600 V, for the MHDV to be able to service all three countries. To support the increasing powertrain voltages lying beyond the reverse standoff voltages of automotive compatible Silicon Carbide (SiC) devices, multilevel power conversion is a suitable option.

This thesis studies the status quo of commercialized BEVs, DC fast charging standards, and their outlook for the next-generation of high-voltage electrfied BEVs. It also performs a comprehensive review of identifying system-level and use-case related challenges in transitioning on-board chargers to higher voltages compared to state-of-the-art, while considering the impact of newly introduced DC fast charging standards like MCS and ChaoJi/ CHAdeMO 3.0. The existing research in academia and proof-of-concept designs compatible for high-voltage on-board charging sub-systems, such as the Power Factor Correction (PFC) and isolated DC-DC conversion stages is consolidated. Due to the demand for integration driven by cost-optimization targets, single-stage, traction-integrated, and auxiliary power unit (APU) integrated on-board chargers are discussed.

The SAE J3068 standard, focused on 3-Φ AC charging recommends compatibility from 208Y/120 to 600Y/347 V, resulting in a large voltage variation of the PFC stage's DC link. To accommodate the voltage swing on the DC link of the PFC stage, this thesis proposes a reconfiguration method of a Neutral- point clamped (NPC) converter incorporated in a three-level Dual Active Bridge (DAB) converter. The Reconfigurable Three-Level Dual Active Bridge (R3L-DAB) converter topology is introduced, and its modes of operation are presented. The steady-state analysis and its soft-switching criterion are discussed. A power loss model and design optimization procedure for this converter is established to choose the Switching Frequency (f_{sw}), Secondary to Primary Turns Ratio (n), and DAB

Converter Leakage Inductance (L_k). Finally, the experimental results of a 15 kW R3L-DAB converter, with a power density of 3.25 kW/L and peak efficiency of 97.32% are presented.

Acknowledgements

I would like to express my deepest gratitude to my supervisor, Dr. Ali Emadi for all the guidance, encouragement, and growth opportunities at McMaster Automotive Resource Centre (MARC). He has developed a research group highly conducive to innovation and applied research, and it is my privilege to be able to pursue my doctoral studies at MARC.

I am thankful to Dr. Mehdi Narimani for his insightful teachings during the 'Power Converter Systems' course. It has had a significant impact in igniting my interest in multilevel power conversion, which is the foundation of this thesis.

I would like to thank the M.A.Sc Defense committee members, Dr. Babak Nahid-Mobarakeh and Dr. Shamsuddeen Nalakath for their feedback in the improvement of this thesis.

I have had the pleasure of collaborating with Dr. Nilou Keshmiri, Shreyas Shah, Dr. Mohamed Ibrahim and Zhenxuan (Walter) Wang, who have been instrumental in the development of this thesis. I am very grateful for their help with technical discussions, design, troubleshooting issues, hardware experiments, and reviewing our papers. I would like to express my sincere appreciation to current and past members in the industry sponsored project by Eaton Corporation; Dr. Alan Callegaro, Dr. Giorgio Pietrini, Guvanthi Abeysinghe, Kyle Kozielski, Linke Zhou, Parsa Beheshti, Sreejith Chakkalakkal, and Jiaqi Yuan.

I am grateful to my former mentors at Maxwell Energy Systems (ION Energy Inc.), Alexandre Collet and Puneet Arora, who have nurtured me during the early stage of my career, and their teachings continue to be useful to this day.

I dedicate this thesis to my late grandfather, Pravin, my grandmother, Madhavi, my parents, Anuradha and Himanshu, and my fiance, Isha. This thesis was not possible without their constant love and encouragement.

Contents

List of Figures

List of Tables

Acronyms

ρ Copper resistivity

A_c Core cross section area

C_{oss} MOSFET output capacitance

f_{sw} Switching Frequency

L_k DAB Converter Leakage Inductance

MLT Mean Length per Turn

n Secondary to Primary Turns Ratio

n_l Number of layers per winding

N_p Primary Winding Turns

N_s Secondary Winding Turns

t_{cu} Copper thickness

V_e Core effective volume

w_{pri} Primary winding PCB trace width

w_{sec} Secondary winding PCB trace width

BEV Battery Electric Vehicle

CAGR Compounded Annual Growth Rate

CCS Combined Charging System

DAB Dual Active Bridge

DUT Device Under Test

G2V Grid-to-Vehicle

GHG Greenhouse Gas

MCS Megawatt Charging System

MHDV Medium- and Heavy-Duty Vehicles

OEM Original Equipment Manufacturer

PFC Power Factor Correction

R3L-DAB Reconfigurable Three-Level Dual Active Bridge

RNPC Reconfigurable Neutral Point Clamped

SiC Silicon Carbide

Chapter 1

Introduction

1.1 Background and Motivation

A high degree of electrification in vehicles results in a reduced CO_{2e} footprint, since BEVs encompass the highest degree of electrification, which aids in a reduced global carbon footprint from transportation related GHG emissions [17]. A study conducted by the United States Department of Transportation shows that North American transborder freight accounted for \$ 1.325 trillion of economic activity, which was a +24 % rise from the year 2020. Out of \$ 1.325 trillion, truck freight accounted for \$ 828 billion of economic activity [18].

Fig. 1.1 shows the breakdown of North American freight based economic activity from United States to Canada and Mexico, where both have a 50 % share. Fig. 1.3 shows the distribution of North American freight based economic activity based on the mode of transportation, and it can be noticed that truck based freight has the largest share, equivalent to approximately 62 % of the total freight.

Mass-manufactured commercial BEVs have their powertrain voltage levels set between 400 - 800 V. Increasing the powertrain voltages provide benefits such as

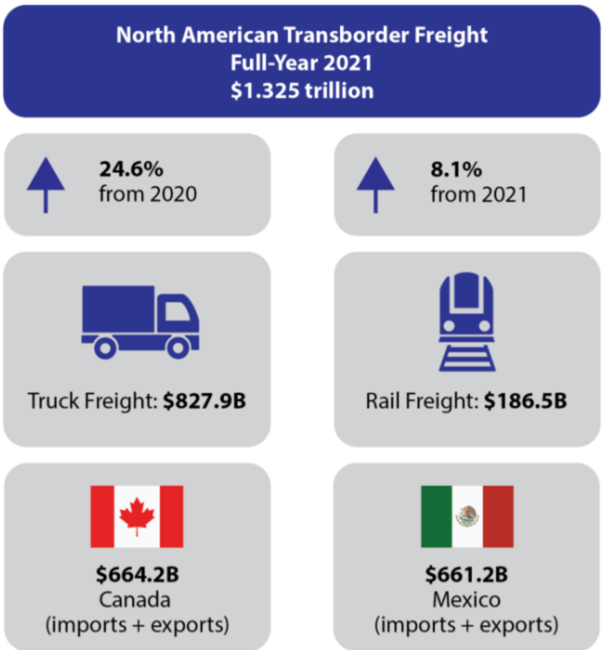

FIGURE 1.1: North American transborder freight (Source: U.S. Department of Transportation)

lower DC fast charging times, lower runtime conduction losses in the powertrain, and thus higher runtime efficiency [19]. One of the latest commercially available BEV, Lucid Air Dream, has a maximum powertrain voltage of 924 V, which is close to the limit of the Combined Charging System (CCS) connector, at 1 kV, and exhibits saturation of the powertrain voltage towards this limit.

The electric truck market is expected to grow at a Compounded Annual Growth Rate (CAGR) of 58 % between 2021 - 2026 [20]. Thus, Medium- and Heavy-Duty Vehicles (MHDV) requiring higher traction powers and a low DC fast charging time would penetrate the BEV market over time. Futuristic DC fast charging standards such as Megawatt Charging System (MCS) (1.25 kV/ 3000 A/ 3.75 MW) and ChaoJi/CHAdeMO 3.0 (1.5 kV/ 600 A/ 900 kW) have been introduced to harmonize the DC fast charging of MHDVs. In North America, the SAE J3068

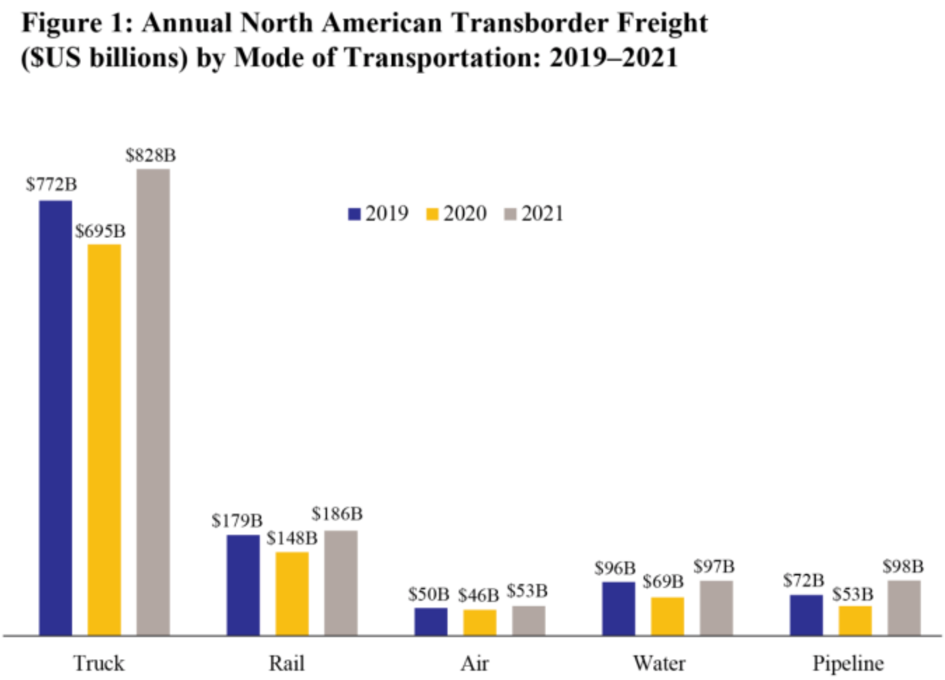

FIGURE 1.2: North American transborder freight by mode of transportation (Source: U.S. Department of Transportation)

standard has been proposed for three-phase AC, or Level 3 AC charging up to 166 kW. The North American power grid does not have an homogenous voltage, and has a range of 208 - 600 V in Canada, 220 - 480 V in Mexico, an 208 - 480 V in the United States of America. This encompasses the recommended voltage level by the SAE J3068 standard. With heavy economic dependency of cross-border freight within the country, it is important for Original Equipment Manufacturer (OEM)s to support on-board charging for a wide AC input voltage range of 208 - 600 V, for the MHDV to be able to service all three countries.

To support the increasing powertrain voltages lying beyond the reverse standoff voltages of automotive compatible Silicon Carbide (SiC) devices, multilevel power conversion is a suitable option.

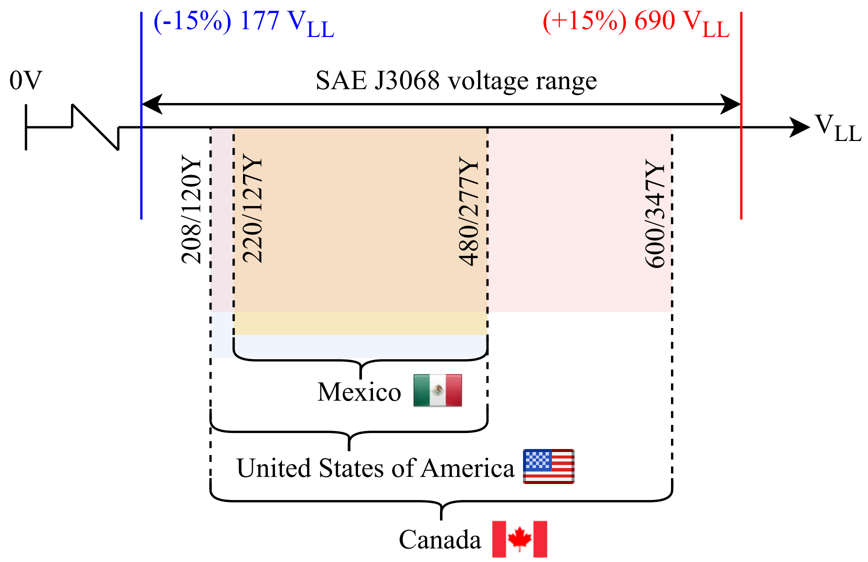

FIGURE 1.3: Three-phase grid voltage range in North America

This thesis studies the status quo of commercialized BEVs, DC fast charging standards, and their outlook for the next-generation of high-voltage electrfied BEVs. It also performs a comprehensive review of identifying system-level and use-case related challenges in transitioning on-board chargers to higher voltages compared to state-of-the-art, while considering the impact of newly introduced DC fast charging standards like MCS and ChaoJi/ CHAdeMO 3.0. The existing research in academia and proof-of-concept designs compatible for high-voltage on-board charging sub-systems, such as the Power Factor Correction (PFC) and isolated DC-DC conversion stages is consolidated. Due to the demand for integration driven by cost-optimization targets, single-stage, traction-integrated, and auxiliary power unit (APU) integrated on-board chargers are discussed.

The SAE J3068 standard, focused on 3-Φ AC charging recommends compatibility from 208Y/120 to 600Y/347 V, resulting in a large voltage variation of the PFC stage's DC link. To accommodate the voltage swing on the DC link of the PFC stage, this thesis proposes a reconfiguration method of a Neutral- point clamped (NPC) converter incorporated in a three-level Dual Active Bridge (DAB) converter. The Reconfigurable Three-Level Dual Active Bridge (R3L-DAB) converter topology is introduced, and its modes of operation are presented. The steady-state analysis and its soft-switching criterion are discussed. A power loss model and design optimization procedure for this converter is established to choose the Switching Frequency (f_{sw}), Secondary to Primary Turns Ratio (n), and DAB Converter Leakage Inductance (L_k). Finally, the experimental results of a 15 kW R3L-DAB converter, with a power density of 3.25 kW/L and peak efficiency of 97.32% are presented.

1.2 Thesis Contributions

The key contributions of this thesis are as follows:

1. A novel reconfiguration method is proposed for a full-bridge NPC converter, that aids in reduction of the conversion effort of a dual active bridge converter, by reducing the voltage swing observed by the high-frequency link. The proposed method aids in switching the bridge between the half-bridge or full-bridge mode, and eliminates the need of additional relays or contactors, which are limited by a fatigue life.

2. The steady-state analysis to derive the closed-form solution of instantaneous current stress, RMS current stress, voltage stress, and zero voltage switching (ZVS) conditions under the defined modulation scheme is defined.

3. The power loss model utilizing the steady-state analytical equations is proposed, to estimate the efficiency of the R3L-DAB converter under varying operating conditions, and a design optimization procedure to select the turns

ratio (n), leakage inductance (L_k) and switching frequency (f_{sw}) has been proposed.

4. The experimental verification of a 15 kW R3L-DAB converter under the defined specifications is performed, and its efficiency map is developed.

1.3 Thesis Outline

The thesis develops the prototype of a 15 kW Reconfigurable Three-Level Dual Active Bridge Converter for on-board charging of next-generation MHDVs with high-voltage powertrains. The prototype achieves a power density of 3.25 kW/L and a peak efficiency of 97.32 %.

Chapter 2 discusses the classification of electric vehicle charging, and its use cases. The status quo of powertrain voltages in existing BEVs has been discussed, to identify the future projection of powertrain voltage levels based on DC fast charging and on-board charging standards and their co-dependency.

Chapter 3 discusses the various architectures of on-board chargers, and their sub-systems such as the PFC stage and Bidirectional Isolated DC-DC Converter. A case study for comparing various topological variations of the dual active bridge converter is performed. The regulatory standards for qualification of on-board chargers are also discussed.

Chapter 4 introduces the Reconfigurable Three-Level Dual Active Bridge Converter. The operating principle of the Reconfigurable Neutral Point Clamped (RNPC) is discussed. The modulation technique of the R3L-DAB is defined, and the steady-state analysis solving the equations of the instantaneous currents, and RMS currents is developed and the accuracy of the modeled equations is verified.

Chapter 5 focuses on the design of the R3L-DAB converter compatible for 1.25 kV on-board charging applications. The requirements for the DC-DC converter are defined. The steady-state analysis is incorporated with a power loss model to estimate the efficiency of the DC-DC converter. A design optimization procedure to choose the f_{sw}, L_k, and n based on the battery charging profile is proposed. The implementation details of the RNPC, planar transformer and the power electronics packaging are presented.

Chapter 6 shows the experimental verification of the R3L-DAB converter for comparison with simulation and modeling results. The efficiency map of the R3L-DAB converter under varying load conditions are developed.

In the end, Chapter 7 discusses the conclusion and future work.

1.4 Publications

As contributions from this thesis, industry-sponsored research projects and research collaborations at McMaster University, the following papers have been published:

Thesis:

1. S. B. Shah, **R. Pradhan** and A. Emadi, "Physical Design Considerations for Three-Level Neutral-Point Clamped DC-DC Converters Using Discrete SiC MOSFETs," 2023 IEEE Transportation Electrification Conference & Expo (ITEC), Detroit, MI, USA, 2023, pp. 1-6, doi: 10.1109/ITEC55900.2023.10186921.

2. **R. Pradhan**, N. Keshmiri and A. Emadi, "On-Board Chargers for High-Voltage Electric Vehicle Powertrains: Future Trends and Challenges," in

IEEE Open Journal of Power Electronics, vol. 4, pp. 189-207, 2023, doi: 10.1109/OJPEL.2023.3251992.

3. **R. Pradhan**, M. Narimani and A. Emadi, "Converter Topology Comparison for a Two-Stage Level-2 Onboard Charger in 800-V EV Powertrains," IECON 2022 – 48th Annual Conference of the IEEE Industrial Electronics Society, Brussels, Belgium, 2022, pp. 1-6, doi: 10.1109/IECON49645-.2022.9968504.

Industry Sponsored Project:

1. K. Kozielski, G. A. Mudiyanselage, **R. Pradhan**, G. Pietrini, A. Solanki, P. Nayak, M. Narimani, and A. Emadi, "Investigation of a Kelvin-Source Connected SMD Silicon MOSFET and its Application in a High Current Full Bridge Synchronous Rectifier," 2023 IEEE Transportation Electrification Conference & Expo (ITEC), Detroit, MI, USA, 2023, pp. 1-6, doi: 10.1109/ITEC55900.2023.10187081.

2. **R. Pradhan** et al., "Design of a 20 kW Bidirectional Dual Active Bridge Converter for Aerospace Applications," 2023 IEEE Applied Power Electronics Conference and Exposition (APEC), Orlando, FL, USA, 2023, pp. 1024-1030, doi: 10.1109/APEC43580.2023.10131638.

3. **R. Pradhan**, M. I. Hassan, A. Dorneles Callegaro, P. Suntharalingam, M. F. Cruz and A. Emadi, "A Framework for Practical Design of Switching Nodes with Parallel-Connected MOSFETs," 2022 IEEE Transportation Electrification Conference & Expo (ITEC), Anaheim, CA, USA, 2022, pp. 331-336, doi: 10.1109/ITEC53557.2022.9813977.

Research Collaborations:

1. N. Keshmiri, **R. Pradhan**, M. I. Hassan and A. Emadi, "An Optimized GaN-Based DAB Converter for More Electric Aircraft," IECON 2022 – 48th Annual Conference of the IEEE Industrial Electronics Society, Brussels, Belgium, 2022, pp. 1-6, doi: 10.1109/IECON49645.2022.9968827.

2. J. Yuan, N. Keshmiri, M. Ibrahim, **R. Pradhan** and A. Emadi, "Optimized Minimum-Loss Hybrid Multiple Phase Shift Modulation Technique for Dual Active Bridge Converters for MEA Applications," IECON 2022 – 48th Annual Conference of the IEEE Industrial Electronics Society, Brussels, Belgium, 2022, pp. 1-6, doi: 10.1109/IECON49645.2022.9968503.

Chapter 2

Electric Vehicle Charging and Powertrain Voltage Trends

2.1 Electric Vehicle Charging

To meet the electric vehicle (EV) market goals set by the Global EV Outlook and governments around the world, expansion of the charging infrastructure is necessary. In 2021, the number of publicly available EV charging stations increased by 41% [21]. EV chargers fall under three categories: DC fast charging, on-board charging, and wireless charging. In this Section, an overview of charging methods is discussed.

DC fast Charging

DC fast charging permits the EV to be fully charged in less than an hour. Fast charging stations are installed on highway rest areas over the US and cities in North America and Europe, similar to a gas station. These systems typically derive power from the grid at voltages of 380 V or higher [22]. These chargers are off-board, meaning they require external installation and infrastructure. Since

Level 3 chargers operate at higher power levels (50 kW and higher), the chargers are larger in size, leading to the need for off-board infrastructure. Public stations typically use Level 2 or 3 chargers to permit rapid charging. However, high-power charging can increase the demand on the grid, impacting the local distribution infrastructure, especially at peak times [23]. In this case, a lower charge power is beneficial to minimize peak time impact. Since DC fast charging is analogous to filling the tank of an ICE vehicle, this method is the most appealing to consumers, in terms of convenience and efficiency. However, the higher cost associated with DC fast chargers and the long-term impact on the battery's state of health (SOH) act as a deterrent for some consumers from using these chargers [24]. Another drawback associated with fast chargers is the scarcity of DC fast charging infrastructure and the resultant range anxiety.

Conductive On-Board Charging

The on-board charger is an electronic sub-assembly (ESA) of the vehicle and is classified into Level 1/ Level 2/ Level 3 AC charging, and can be bidirectional or unidirectional in nature. Unidirectional charging from the grid to the EV is the most common type of charging. This method reduces the hardware requirements and lowers the cost. Battery degradation is also reduced with unidirectional charging, extending the battery lifetime [25]. Bidirectional charging permits charging of the EV from the grid while enabling power flow back to the grid from the EV battery, i.e. V2X operation. With on-board chargers, the power level is limited due to cost, space, and weight limitations. Integration of the OBC with the electric drive enables the design of power dense solutions [25]. OBCs can be further categorized into inductive and conductive chargers. Charging through direct contact between the charge inlet and connector is referred to as conductive on-board charging. The process through which power is transferred magnetically is known as inductively coupled on-board charging. Compared to DC fast chargers, an OBC permits the EV owner to charge their vehicle overnight at the convenience of their home. Since charging typically occurs outside of peak hours (overnight), the net cost of on-board charging is lower than that of DC fast charging. The risk of battery degradation is also reduced due to lower C-rates encountered by the battery pack [26].

Inductive (Wireless) On-Board Charging

In recent years, wireless charging has gained a lot of attention. As with consumer products, wireless charging of an EV permits more convenient charging. This process occurs via inductive coupling, where the electric current passing through a coil creates a magnetic field, transferring power between the primary and secondary coils [27]. The concept of wireless charging can take place in a parking lot or at a rest stop while the vehicle is parked. Instead of charging over extended periods of time, charging can take place prior to the EV battery reaching 100% charge and before the battery is drained to nearly 0%.

Charger Use Case Trends

The total number of publicly available fast chargers was about four times that of publicly available slow chargers, from 2015-2021 [28]. There are increasing concerns about the stability of the grid with the increased use of DC fast charging [29–32]. The low cost of residential electricity versus the cost of public charging stations as well as the cost of gas, makes home charging the most affordable charging option. In Canada, the cost comparison between OBC and DC fast chargers can be summarized as below [33]:

- In Quebec, the use of OBC is 30% less expensive than DC fast chargers and six times less expensive for driving 62 miles on electricity as opposed to gas.
- In Ontario, it is 65% less expensive to use an OBC than a DC fast charger and five times less expensive to drive 62 miles on electricity versus gas.
- In British Columbia, it is 30% cheaper to charge at home compared to using a fast charger and five times less expensive to drive 62 miles on electricity versus gas.

A consumer case study performed by *Morrissey et al.* shows that peak usage of DC fast charging happens in the evening, while it happens in the afternoon and night for the standard charging (on-board charging) [34]. When consumers park their vehicles, on-board charging is more suitable since there is ample time to top-up the vehicle. This data suggests that most EV consumers prefer on-board charging, and this trend is expected to stay the same, with increased deployment of DC fast chargers, due to the cost incentive of using on-board chargers.

2.2 Increasing Battery Pack Voltage

In a BEV, the high-voltage (HV) battery pack is the primary and sole source of energy for both propulsion and auxiliary functions of the vehicle. The battery pack is typically constructed using a combination of paralleled and serialized Li-ion cells. The cell configuration is generally denoted as $XsYp$, where X is the number of series-connected cells, and Y is the number of parallel-connected cells used to form the battery pack. There has been a general trend of vehicle manufacturers increasing the battery pack voltage. A high-voltage battery pack reduces the current required to transfer the same power at a lower voltage and thus offers benefits such

TABLE 2.1: List of BEVs (Sedans) in production indicating their Li-ion battery voltages, capacities, and OBC power levels [1–11]

Vehicle	Release	Origin	Max. Battery Voltage (V)	Cell	Cell Config.	Battery Capacity (kWh)	OBC Power Level (kW)	≈ Charge Time
Lucid Air Touring	2022	U.S	756	21700	180s30p	93	19.2	4h 51m
Audi e-Tron GT	2021	Germany	832	Pouch	198s2p	93	11*	8h 27m
Lucid Air Dream	2021	U.S	924	21700	220s30p	118	19.2	6h 09m
BYD Han	2020	China	420	BYD Blade	115s1p	76.9	6.6	11h 39m
Porsche Taycan Turbo S	2019	Germany	832	Pouch	198s2p	93.4	11*	8h 30m
Porsche Taycan	2019	Germany	706	Pouch	168s2p	79.2	11*	7h 12m
Tesla Model 3 LR	2018	U.S	403	21700	96s31p	82	11	7h 27m

* 22 kW Power Level is available as an optional upgrade. The default power level of 11 kW is specified.

as lower run-time ohmic losses, very low DC fast charging duration, and reduction in the overall weight of the powertrain conductors. Table 2.1 consolidates a list of production BEVs (Sedans) sorted as per their release/serial production date, indicating the above-mentioned trend of increasing battery pack voltages [1–11].

2.2.1 Projection of Battery Voltage Limits

The first standard indicating the connector specifications of a conductive coupling-based charging method was established in 2001 with the standard SAE J1772-2001 [35]. The first serial production BEV with a Li-ion battery pack was a Tesla Roadster, released in 2008 [36], seven years after the connector specification was first defined. Tesla and other consortiums have established their own charging standards as the BEV landscape evolved. Historically, the charging connector specification has attempted to be standardized ahead of its vehicle production timeline. Based on a study in the UK, DC fast charging installations have seen an average year-on-year (YoY) increase of 35% [37], indicating a heavy push to fast charging infrastructure. The U.S. Department of Transportation (U.S. DOT) and U.S. Department of Energy (U.S. DOE) have committed $5 Billion towards building a national EV charging network under the National Electric Vehicle Infrastructure (NEVI) formula program [38]. With ample capital expenditure budgets towards charging infrastructure, on-road and upcoming BEVs are required to be

TABLE 2.2: >1 kV DC fast charging connector specifications

DC fast charging Connector	Region	Voltage (V)	Current (A)	Power (kW)
CHAdeMO 3.0 / ChaoJi	Japan, China	1500	600	900
Megawatt Charging System (MCS)	North America, E.U	1250	3000	3750

compatible with the specifications of DC fast charging infrastructure.

The charging connector standards indicating the DC fast charging levels implemented worldwide have been listed in [22, 39]. As of 2022, the highest voltage offered by any DC fast charging connector is via the CHAdeMO 2.0 or CCS Combo 2 at 1000 V. The 2021 Lucid Air Dream has a battery operating at a maximum of 924 V, which is indicative of saturation towards the upper voltage limit offered by existing DC fast charging connectors [1]. In addition, regional variations of the charging connectors introduce additional stock-keeping units (SKUs) in a vehicle's grid-interface components and increase the cost overheads experienced by an Original Equipment Manufacturer (OEM), which percolates to the user. CharIN has defined the specifications of the Megawatt Charging System (MCS) capable of delivering up to 3.75 MW of power (1.25 kV/ 3000A) and is intended for global adoption for DC fast charging of trucks, buses, and perhaps aerospace, marine, and mining equipment as well [40]. This standard is also proposed for harmonization under SAE J3271, which is currently under development [41]. In Japan and China, the CHAdeMO 3.0/ChaoJi standard can provide DC fast charging up to 900 kW (1.5 kV/ 600 A) [42]. The definition of this standard opens up possibilities of increasing the battery pack's voltage level beyond the existing limit of 1 kV [43].

Fig. 2.1 shows the graphical representation of the battery pack voltages, and

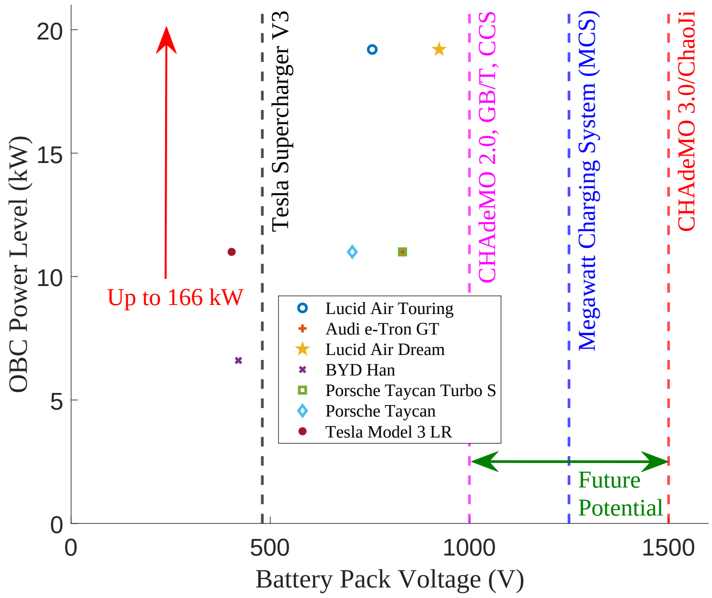

FIGURE 2.1: Current status of battery voltage and OBC power levels of BEVs in comparison to the DC fast charging connector voltage limits

OBC power levels of the vehicles discussed in Table 2.1. The voltage limits have been compared against existing DC fast charging connector capabilities [22, 42]. Table 2.1 shows that all vehicles have battery pack voltages limited to 1 kV. This opens up a new band of the vehicle's battery pack voltage level, where 1 kV < V_{batt} < 1.5 kV.

2.2.2 Challenges in Scaling the Battery Voltage

A high serialized cell count is required to increase the battery pack voltage. Based on the type of vehicle (Sedan/Hatchback/SUV/Van/Bus), the volume available for the battery pack is fixed. Increasing the allocated battery pack volume can compromise product-level features such as available passenger space, or reduction in maximum attainable speed. From Table 2.1, it can be observed that the general battery pack capacity of Sedans lies between 77-94 kWh, with an exception of Lucid Air Dream, which is the high-range variant of Lucid Air [1]. With the limit of the battery pack capacity in battery-operated Sedans being well established, a similar consolidation shall be foreseen in other vehicle types. Based on the existing cell configurations and in-production cells, a reconfiguration can be performed to increase the battery voltage, however, the following challenges are observed:

- Due to increased voltage, additional clearance and creepage distance are required to avoid insulation failure/partial discharge, while meeting the battery safety requirements as per UL 2580 [44]. This consumes unused volume in the battery pack's chassis and packaging the same number of cells as the lower voltage battery pack may not be possible.

- Scaling the voltage up to 1.5 kV requires reconfiguration of the cell count such that existing battery packs have their parallel cell count reduced, and serial cell count increased to achieve the desired string voltage. This is possible in cases where parallelling is performed , unlike the BYD Han, which utilizes the BYD Blade cell in a 1p configuration [6].

- The battery management system (BMS), which is responsible for the safety and state estimation of the battery, generally follows a functional safety development cycle, recommended by ISO 26262 due to its safety-critcal role in the vehicle powertrain [45, 46]. Measurements such as redundant battery string voltage and contactor weld detection circuits require isolation amplifiers with enhanced isolation to maintain isolation between the low-voltage and high-voltage circuitry [47].

- The high-voltage battery has a redundant disconnect mechanism as a functional safety requirement. The chemical pyrofuse is activated when the contactors are unable to open the battery circuit in the event of a critical safety

Table 2.3: Battery specifications of medium and heavy-duty BEVs [12–16]

Vehicle	Vehicle Type	Origin	Battery Voltage (V)	Battery Capacity (kWh)
Nikola Tre	Semi-Truck	U.S	800	753
Tesla Semi (300)	Class 8	U.S	800	≈ 600
Tesla Semi (500)	Class 8	U.S	800	≈ 1000
BYD K9M	40' Bus	China	693	313
BYD K11M	60' Bus	China	-	578
Scania Electric Truck	Electric Truck	Sweden	650	624

violation. The contactors are typically realized using the white-labeled versions of the TE Connectivity KILOVAC/GIGAVAC/EVC series automotive contactors, which are rated up to a maximum voltage of 900 V among all the above-mentioned series [48]. Switchgear manufacturers would require to work with OEMs to develop and validate a high-voltage series of automotive contactors and fuses to support voltages up to 1.5 kV.

2.2.3 Applications of > 1 kV Battery Voltage

The list of existing DC fast charging standards and their respective charging connector current and voltage limits are discussed by the authors in [39]. As the voltage increases, the ability to deliver higher power at a particular current limit increases. This will vary the C-rates at which the battery packs are being charged.

$$E_{batt(kWh)} = 400V.B_{cap(Ah)} = 1500V.\left(\frac{B_{cap(Ah)}}{3.75}\right) \tag{2.1}$$

To portray the impact of varying C-rates, a comparison between 400 V and 1500 V systems is made. As highlighted in the previous subsection, the maximum

C-rates for a Tesla Model 3 vary between 2.6 C-3.3 C at 195-250 kW. The total energy capacity of the battery pack $E_{batt(kWh)}$ is achieved by having a battery capacity of $B_{cap(Ah)}$ for a 400 V system, as seen in (2.1). In the case of a 1500 V system, the same energy capacity is achievable by having a battery capacity of $\frac{B_{cap(Ah)}}{3.75}$. Under a case where the resultant charging currents are the same (almost one fourth the charging power at 400 V compared to 1500 V), the C-rates for an assumed energy capacity of a battery will be 3.75 times at the 1500 V bus voltage level. Maintaining a moderate temperature rise at the higher C-rates will increase challenges on the thermal management significantly [49]. This means that as the battery pack voltage increases, it would be imperative to increase the battery pack capacity to keep the thermal management reasonable at higher power levels. As seen in Table 2.1, the average battery capacity of BEV Sedans is approximately 90 kWh. With increased voltage levels, and to fully utilize the benefits of higher voltage charging while maintaining existing C-rates, the battery pack capacity is required to be at least 4x, i.e. 360 kWh. This also aligns with the motivation of introducing the MCS and CHAdeMO 3.0/ChaoJi standard, that was to cater the medium to heavy vehicles DC fast charging segment. Table 2.3 shows the battery voltages and capacities of medium and heavy duty vehicles that are in production and due for release [12–16]. It can be observed that the battery capacities lie in the $>$ 300 kWh range. The voltages, however are still in the $<$ 1 kV range due to large deployment of CCS compliant DC fast chargers, lack of a charging connector standardization, and a lack of maturity of high-voltage DC fast charging standards [50] .

2.2.4 Power Level Classification

The three key markets in the world with high penetration of BEVs are the United States (U.S), European Union (EU), and China. Their regional electrical transmission networks operate at unique and incompatible voltage levels, which drives the power-conversion stage design based on regional need. It is notable that the EU and China have similar operating voltages, and hence the OBC can be designed for inter-compatibility between these regions. On-board charging can be classified into 3 levels.

AC Level 1 (L1) Charging ($<$ 3.7 kW)

This level is used in cases where very slow charging is acceptable. The general charging duration for a full charge varies between 3-4 days depending upon the power level and the vehicle's battery capacity. The United States supports two connectors for L1 charging, the SAE J1772 and the Tesla proprietary connector. As per SAE J1772, 1.92 kW L1 charging can be supported with a 120 V/16 A single-phase supply [51]. The Tesla proprietary connector supports a 1.4 kW L1 charging level with its mobile connector that plugs into a standard NEMA 5-15 wall outlet, drawing 12 A from a 120 V single-phase supply [52]. The L1 charging specification is not applicable to the EU and China.

AC Level 2 (L2) Charging (3.7 - 22 kW)

This level is used in cases where the vehicle is required to be fully charged under a 7-8 hour charging use case. In the United States, both the SAE J1772 and Tesla connectors support L2 charging up to 19.2 kW [51] and 11.5 kW [11] when powered up using a 240 V single phase (1 Φ) supply. In installation cases where the power is drawn between two phases of a three phase (3 Φ) Wye-connected rail, the available voltage is 208 V, and the power is limited to 16.6 kW, within the specification of SAE J1772. Tesla's OBC does not support the 208 V voltage level. In the EU, charging is supported by the IEC 62196 Type 2 connector. With 1 Φ 230 V, the power level is limited to 7.36 kW, while at 3 Φ 400 V, a charging power of 22 kW can be achieved. This power is limited by the connector contact's current rating of 32 A [53]. In China, the GB/T 20234 AC connector supports L2 charging. With 1 Φ 220 V, the power level is limited to 7.04 kW, while at 3 Φ 380 V, a charging power of 21.12 kW can be achieved. This power is also limited by the connector contact's current rating of 32 A [54].

AC Level 3 (L3) Charging (22 - 166 KW)

This level was originally considered for a range of 22 - 43.5 kW by the SAE J1772 standard, however was never implemented for light vehicles. As per Appendix M of the SAE J1772 standard, the SAE J3068 standard was referred for the development of three-phase on-board charging for medium to heavy-duty vehicles [51]. Since the SAE J1772 connector does not support three-phase charging, a modification of the IEC 62196-2 connector has been proposed for use under the SAE J3068 standard for use in North America [55]. The 3 Φ supply is available at distinct voltage levels such as 208/480/600 line-line voltage (V_{LL}). The power level is limited by the current capability of the IEC standard contacts at 63 A. SAE J3068 has also defined advanced contacts of 100 A, 120 A, and 160 A to further increase the power delivery to the OBC when heavy-duty vehicles such as buses, trucks, industrial machinery are manufactured with large battery packs. In the EU and China, the OBC levels are restricted to 43.5 kW and 40.92 kW, as originally defined under SAE J1772.

Table 2.4: Regional, voltage, and power based classification of OBCs

North America				
SAE J1772 Level	**Connector**	**Voltage (V)**	**Current (A)**	**Power (kW)**
AC Level-1 3.7 kW	J1772	1 Φ 120	16	1.92
	Tesla	1 Φ 120	12	1.4
AC Level-2 3.7-22 kW	J1772	3 Φ V_{LL} 208	80	16.6
		Split 1Φ 240	80	19.2
	Tesla	Split 1Φ 240	48	11.5
AC Level-3*	IEC 62196 Type 2	3 Φ 208Y/120	63/160†	22.7/57.6
		3 Φ 480Y/277	63/160†	52.3/133
		3 Φ 600Y/347	63/160†	65.6/166.5
Europe				
AC Level-1 3.7 kW	-	-	-	-
AC Level-2 3.7-22 kW	IEC 62196 Type 2	1 Φ 230	32	7.36
	IEC 62196 Type 2	3 Φ 400Y/230	32	22
AC Level-3 22-43.5 kW	IEC 62196 Type 2	3 Φ 400Y/230	63	43.5
China				
AC Level-1 3.7 kW	-	-	-	-
AC Level-2 3.7-22 kW	GB/T 20234 AC	1 Φ 220	32	7.04
		3 Φ 380Y/220	32	21.12
AC Level-3 22-43.5 kW	GB/T 20234 AC	3 Φ 380Y/220	64	40.92

* SAE J1772 was never implemented for L3 charging in the U.S, and was replaced by SAE J3068 [55]

† Maximum amperage of the Advanced Contact defined under SAE J3068.

2.2.5 Co-Dependency of DC fast and On-Board Charging Voltage Levels

The DC fast charging connector specification is one of the most significant factor in driving the battery voltage limits of a vehicle. The available on-board charging power is determined by the limits of the AC charging connector, which varies based on the geographical region of operation. The AC and DC fast charging connectors are often integrated into one connector (such as the CCS Combo). For moving to higher voltage levels, identifying the points of interaction betweeen DC fast and on-board charging is required. Fig. 2.2 discusses the various architectures and their relevant use cases that can be expected as an interaction between DC fast charging and conductive on-board charging.

< 1 kV Battery with a Lower Voltage DC fast Charger

The configuration shown in Fig. 2.2 (a) is representative of a case to support a DC fast charger with a lower voltage compared to the battery pack voltage. An intermediate stage of DC-DC conversion is required to match the voltage of the DC fast charger with that of the battery. In this case, the battery voltage range is 400 V - 1 kV, and the DC fast charger is rated up to 400 V. Matching the voltage between the output of the DC fast charger and the battery pack is typically achieved by operating the OBC in the DC-DC conversion mode. This can be done by bypassing the PFC stage, and only utilizing the DC-DC converter in the OBC. Lucid Air has this support for legacy 400 V chargers for its 924 V battery voltage, enabling legacy charging up to 50 kW due the 'Wunderbox', which acts as an active front end [56]. Vicor Power has launched the NBM6123, which is a 6 kW power module with a peak efficiency of 99.3% for assisting compatibility between 400 V DC fast charger and 800 V BEV architectures [57]. Matching the power level of the on-board DC-DC converter to that of the DC fast charger (up to 400 kW) is unrealistic due to associated cost and added weight in the vehicle. Due to this reason, the DC fast charging power is limited to the power level of the on-board DC-DC converter, and is the drawback of this use case.

< 1 kV Battery with a Compatible DC fast Charger

The configuration shown in Fig. 2.2 (b) is representative of a case to support a DC fast charger that is compatible with the battery pack voltage (<1 kV). The support of both 400 V and 800 V class vehicles can be done with the use of a wide-output voltage DC fast charger [58]. No additional DC-DC conversion stages are required in the case of DC fast charging, and hence charging power level is not compromised. CCS and SAE J3068, both have a DC connector voltage specification of 1 kV, and hence the battery voltage is limited by it. The charging infrastructure is currently tackling the inter-compatibility issue between 400 V and 800 V class vehicles [19, 59].

< 1 kV Battery with a Compatible DC fast Charger and Automated Connection Device (ACD) Support

The SAE J3105 standard defines the electrical and physical properties of an Automated Connection Device (ACD), that is used to enable conductive charging via an overhead pantograph [60]. The voltage level of this standard also matches that of CCS and SAE J3068, which is why the architecture represented in Fig. 2.2 (c) integrates an ACD network upon the architecture defined in Fig. 2.2 (b). Since the voltage levels are compatible, the ACD can be integrated by having a selection path between the DC fast charging and ACD input being routed to the battery pack [61].

1-1.5 kV Battery With a Lower Voltage DC fast Charger

This use case is similar to the one shown in Fig. 2.2 (b), with a difference being rated at a higher voltage. As seen in [28], the number of publicly available DC fast charging stations is increasing, and there is a large deployment of CCS compliant charging stations for light vehicles. It is also discussed in Section 2.2.3 that higher voltage powertrains would be advisable for medium to heavy-duty vehicles. The parking locations differ in size between light and medium to heavy-duty vehicles [62]. Due to this reason, the existing charging infrastructure would not be applicable for for higher voltage vehicle applications. Tesla Megachargers are being installed to support the charging of Tesla Semi [63]. To utilize the full potential of DC fast charging, the on-board DC-DC converter used to match the voltage level is required to be sized for the full power level, which is not feasible. Due to these reasons, the likelihood of mass adoption of the charging architecture shown in Fig. 2.2 (d) as a long term solution is not viable.

1-1.5 kV Battery With Independent DC fast and On-Board Charging Connectors

Both CCS and the combined AC and DC connector of SAE J3068 are limited up to 1 kV operation from the DC connector's specification. This is a major barrier in increasing the battery voltage beyond 1 kV for medium or heavy-duty vehicles, for which SAE J3068 is also the intended on-board charging standard. The SAE J3068 charging connector is a derivative of the IEC 62196-2 connector system, which is a reason for this limitation. Higher voltages cannot be achieved without changes in the connector geometry to accommodate suitable creepage and clearance limits for higher voltages [64]. The architecture shown in Fig. 2.2 (e) relies upon separated AC charging and DC charging connectors. AC Level 3 charging has a possibility

TABLE 2.5: Potential regional combination of AC Level 3 and DC fast charging connectors

Region	**AC L3 charging connector**	**DC fast charging connector**	**Max. Battery Voltage (V)**
North America	SAE J3068	MCS	1250
Europe	IEC 62196-2	MCS	1250
Japan/ China	GB/T 20234 AC	CHAdeMO 3.0/ ChaoJi	1500

to be scaled up to 166 kW. DC charging can be scaled up to 3.75 MW via the MCS, and 900 kW via CHAdeMO 3.0/ChaoJi, and there is no combined AC and DC charging connector currently planned. Taking an example of DC fast charging at 900 kW/ 1.5 kV, the current rating is 600 A. The weight of a compatible 1.5 meter DC fast charging cable will be about 26 kg [19]. Management of cable weight in combining a connector for both the DC fast and AC Level 3 charging power levels will be challenging, and thus acts as a catalyst to separate the charging connectors. Based on the planned region of operation, Table 2.5 discusses the possible combination of the AC Level 3 and DC fast charging connector and their relevant battery voltages.

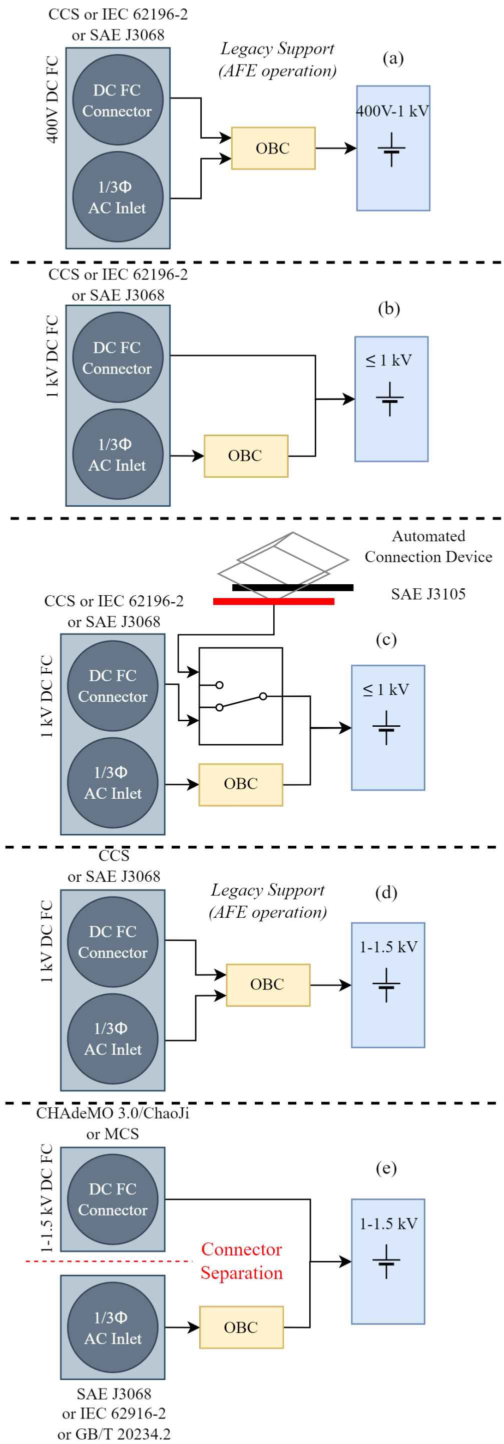

FIGURE 2.2: Co-dependency scenarios of DC fast and on-board charging (a) $<$ 1 kV Legacy DC fast charging (b) $<$ 1kV DC fast charging (c) $<$ 1kV DC fast charging with ACD support (d) 1-1.5 kV legacy DC fast charging (e) 1-1.5 kV with independent DC fast and on-board charging.

Chapter 3

High-Voltage On-Board Chargers

3.1 On-Board Charger Sub-Systems

In this Section, the sub-systems of a two-stage on-board charger have been discussed. Possible candidates of the AC-DC converter stage i.e the power factor correction (PFC) and the DC-DC converter stage have been presented. A consolidated comparison of all the relevant topologies has been discussed for each converter type.

3.1.1 Power Factor Correction (PFC) Stage

The PFC stage is encountered at the grid interface. It is required since the conventional AC-DC converters (rectifiers) lead to a poor power factor, and manifest as issues such as harmonic injection, voltage droop, flat-topping at the AC mains, that lead to poor power quality [65]. OBCs with high power levels, such AC Level 2 ($>$19.2 kW) and Level 3 require three-phase operation because of the limited power that can be drawn from a single phase supply. The variations of boost or buck type PFCs is discussed in detail in [66]. Since this thesis focuses on high-voltage charging, this discussion is limited to three-phase boost-type PFCs for

Table 3.1: OBC voltage range based on region and charging level

Region	**1 Φ Voltage Range (V)**	**L1**	**L2**	**L3**	**3 Φ Voltage Range (V)**	**L1**	**L2**	**L3**
North America	120-240	✓	✓		208-600			✓
Europe	230		✓		400		✓	✓
China	220		✓		380		✓	✓

the sake of brevity. As seen in Table 3.1, BEV applications in North America require support of a three-phase PFC capable of managing 208-600 V_{LL}, since the three-phase distribution voltage levels in the U.S. and Canada vary as 208Y/120, 480Y/277, 600Y/347, and are also under the purview of SAE J3068 [55]. It is also seen that Europe and China have one three-phase distribution voltage level at 400Y/230 V and 380Y/220 V respectively.

The three-phase full bridge (FB) PFC is shown in Fig. 3.1 (a). It is constructed using three inductors at the input of the bridge that act as the boost inductors, six active switches (Q_1 to Q_6), and a filter capacitor to develop the DC link. A 98.8% efficient Silicon Carbide (SiC) based 5 kW three-phase full bridge PFC is developed in [67]. The three phase three-level (3L) T-type PFC is shown in Fig. 3.1 (b). It is a boost type PFC constructed in the same philosophy as that of the full bridge PFC, however it has six additional switches ($Q_7 - Q_{12}$) connected to the netural point generated by a split-capacitor network on the DC link. The additional switches are used to develop a 3-level waveform that provides a reduced dv/dt and better control on the boost inductor current, resulting in improved electromagnetic interference (EMI) and total harmonic distortion (THD) performances of the PFC stage [68]. A 97.3% efficient SiC based 10 kW three-phase T-type PFC is developed in [69]. Due to the high power operation of three-phase PFC rectifiers, they typically operate in the continuous conduction mode (CCM) [70]. Operation

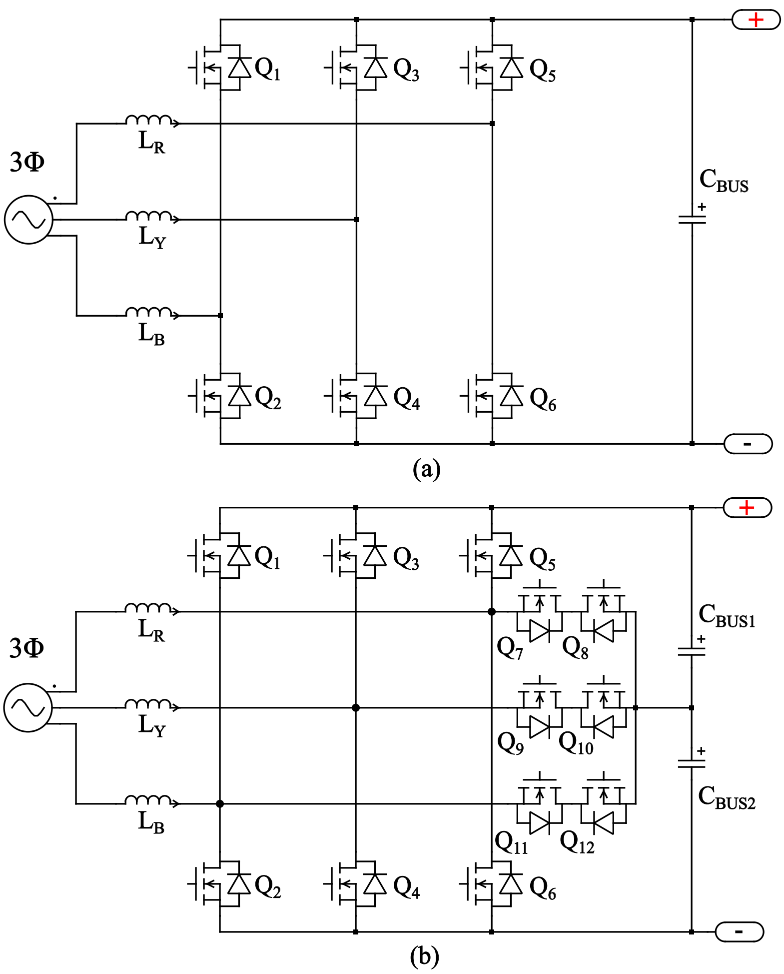

FIGURE 3.1: Three-phase (a) full bridge and (b) 3L T-type PFC converters

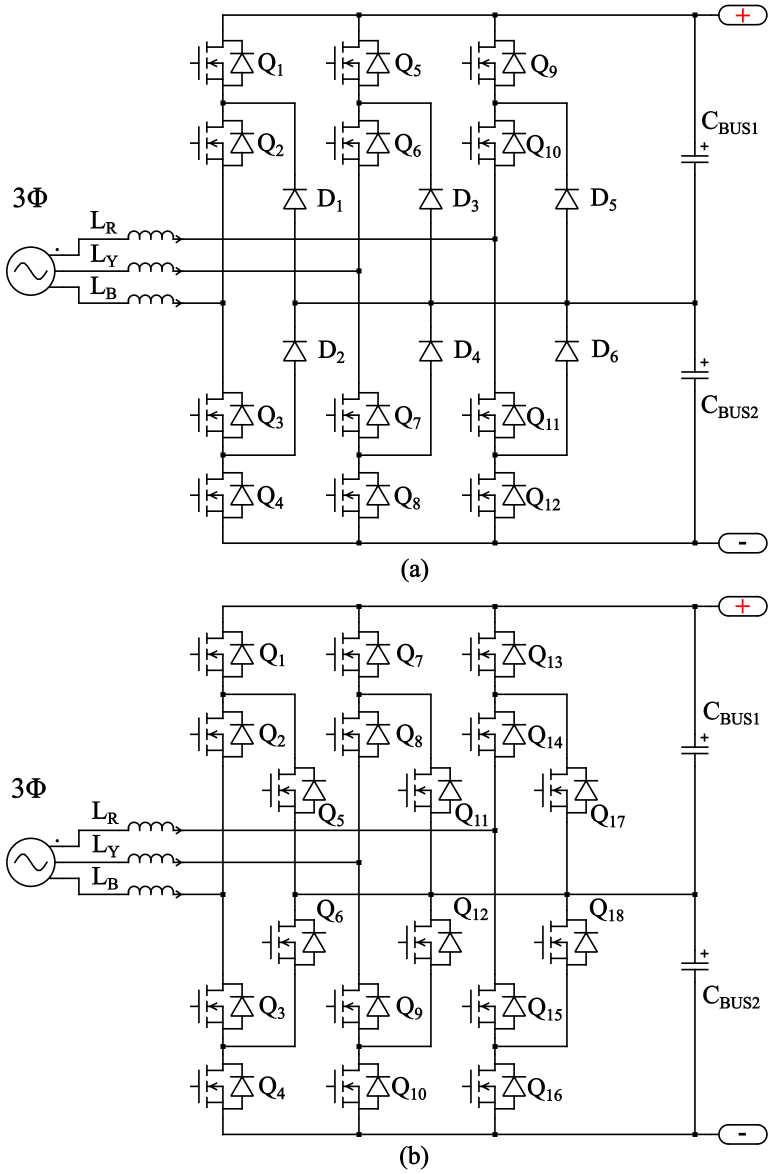

Figure 3.2: (a) 3L NPC and (b) 3L ANPC PFC converters

in CCM causes increased switching losses in the PFC rectifier and reduces its efficiency [71, 72]. The previously discussed PFC converters suffer with increased switching losses, that can be reduced using a neutral-point clamped (NPC) converter structure. Fig. 3.2 (a) shows the schematic of a 3L NPC PFC converter. It is constructed using three boost inductors, 12 switches ($Q_1 - Q_{12}$), six clamping diodes ($D_1 - D_6$) and a split DC bus using two capacitors. The 3L NPC PFC suffers from doubled conduction losses since two additional switches are included in every current conduction path [73]. An IGBT based 95.2% efficient NPC converter has been developed for EV charging station applications in [74]. The efficiency of this converter is low, due to the use of Si IGBTs, and can be further improved with the use of SiC MOSFETs [75]. To reduce the forward conduction losses in the diode, they can be replaced by active clamps, resulting in further improved efficiency with the implication of increased cost. A 98.5% efficient 11 kW Gallium Nitride (GaN) based 3L-ANPC PFC stage has been developed by the authors in [76]. It is worth mentioning that an additional leg is required for balancing the capacitor voltage of a three-level converter in case the applied modulation scheme cannot maintain balance [77].

Table 3.2 shows the tabulated count of HV field effect transistors (FETs), low-voltage (LV) FETs, diodes, gate drivers, and voltage sensors required to construct the discussed topologies. The data on existing work is available for varying frequencies, voltages, and device technologies. Identifying the most viable trade-off as an option for the PFC stage requires an extensive common-baseline comparison curated for this application.

TABLE 3.2: Summary of power factor correction (PFC) stage options

Topology	HV FETs	LV FETs	Diodes	Drivers	Voltage Sensors	Power	Switches	V_{dc}	f_{sw}	Eff.	Ref.
2L Full Bridge	6	0	0	6	4	5 kW	SiC	700 V	45 kHz	98.8%	[67]
3L T-type	6	6	0	9	5	10 kW	SiC	800 V	50 kHz	97.3%	[69]
3L NPC	12	0	6	12	5	2 kW	IGBT	460 V	25 kHz	95.2%	[74]
3L ANPC	12	6	0	18	5	11 kW	GaN	800 V	100 kHz	98.2%	[76]
						4.2 kW	Si+SiC	650 V	40 kHz	99.1%	[78]
						10 kW	Si+SiC	570 V	140 kHz	99%	[79]

3.1.2 Bidirectional Isolated DC-DC Converter

The isolated DC-DC converter is encountered after the PFC stage, and is the link between the battery and DC link of the PFC stage. Galvanic isolation between the battery pack and the grid is a requirement of the UL 2202 standard, and is the conventional form of developing the DC-DC converter [80]. The risk of a shock during the converter operation is also governed by the leakage current limits between the battery's negative terminal and the vehicle chassis. There are some advances in transformerless DC-DC converters, by forcing the common-mode voltage to zero and eventually reducing leakage current to earth [81]. However, they are susceptible to unsafe operation due to single-point faults in the power converters that can risk exposure of a direct connection between the grid and battery pack. Systematic failure analysis and counter-measures against the identified failures is required to make it viable for mass adoption. The most commonly used isolated DC-DC converter topologies such as the two-level (2L) dual active bridge (DAB), LLC, CLLC converter have been covered extensively in literature. The objective of this subsection is to focus on multi-level DC-DC converters that can be applied to the next-generation 800 V, 1.25 kV, and 1.5 kV classes of vehicles.

Fig. 3.3 shows a LCL-T resonant network based stacked half bridge (SHB) converter, which was proposed in [82]. This converter is fed from a constant voltage

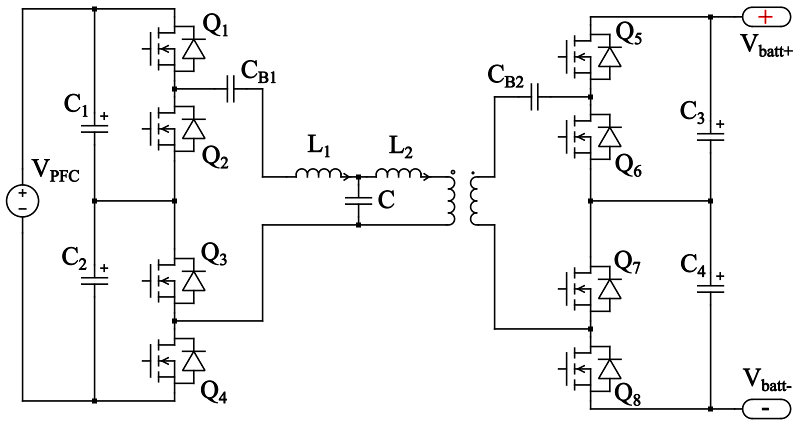

FIGURE 3.3: LCL-T network based stacked half-bridge converter.

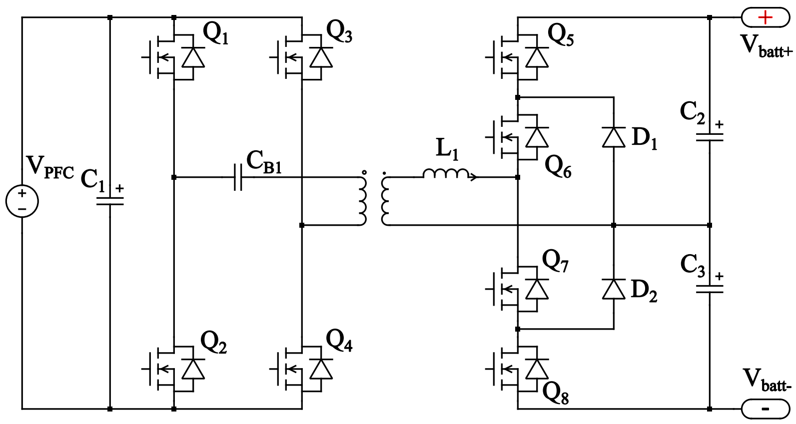

FIGURE 3.4: 2L FB - 3L NPC HB dual active bridge converter.

800 V universal PFC output, and is intended for use in universal DC fast charging (150 - 950 V) with the means of external reconfiguration contactors. The mode created using a stacked half bridge can be utilized for HV on-board charging applications. This converter is constructed using eight GaN high electron mobility transistors (HEMTs) ($Q_1 - Q_8$), an LCL-T network designed with a resonant frequency equal to the converter's switching frequency, and two DC blocking capacitors C_{B1} and C_{B2} to avoid transformer core saturation. This 6.6 kW converter exhibits a full-load efficiency of 97.4% at a battery voltage of 750 V.

Fig. 3.4 shows a dual active bridge converter constructed using a 2L full bridge

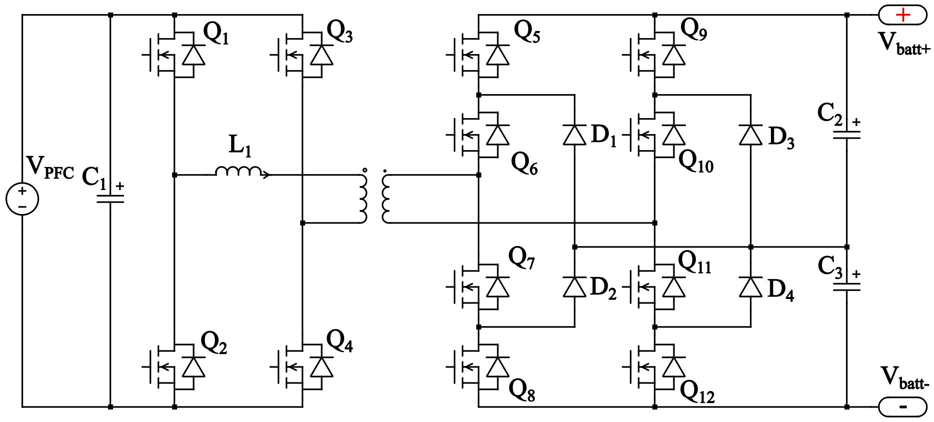

FIGURE 3.5: Multilevel dual active bridge converter.

(Q_1-Q_4), and isolation transformer, leakage inductance (L_1), and 3L NPC half bridge (HB) using (Q_5-Q_8, D_1, D_2) on the HV side, and is proposed in [83]. The intended use of this converter is in weight-sensitive aircraft applications with an 8 kV bus created using 4 serialized converters [84]. The output voltage of each converter is approximately 1.7 - 2 kV, and is thus useful in the HV on-board charging application as well. It is constructed using cascode-connected 1.7 kV SiC JFETs, operated at 100 kHz, and has an efficiency of 97%. Fig. 3.5 shows a multilevel dual active bridge converter constructed using a 2L full bridge on the LV side (Q_1-Q_4), a leakage inductance (L_1), isolation transformer, and a full bridge constructed using 3L NPC converters (Q_5-Q_{12}, D_1-D_4). This converter was first proposed by *Moonem et al.* for solar photovoltaic and DC microgrid applications in [85]. This converter is realized using IGBTs operated at 5 kHz, and exhibits a full load efficiency of 88%, while the transformer efficiency is at 93% [86]. Fig. 3.6 hows a 3L dual active bridge converter with blocking capacitors [87]. It is an extension of the previously discussed multilevel dual active bridge converter, with a 3L NPC bridge on both the interfaces, and DC blocking capacitors (C_{B1}, C_{B2}) to prohibit DC voltage generated by the 3L NPC bridges to be passed to the transformer. An SiC based 3.5 kW DC-DC converter operating at 50 kHz exhibits a full-load

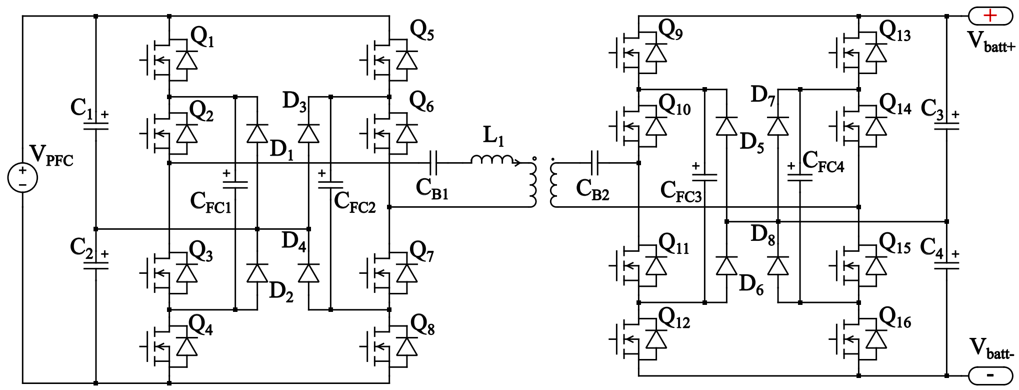

FIGURE 3.6: 3L dual active bridge converter with blocking capacitors.

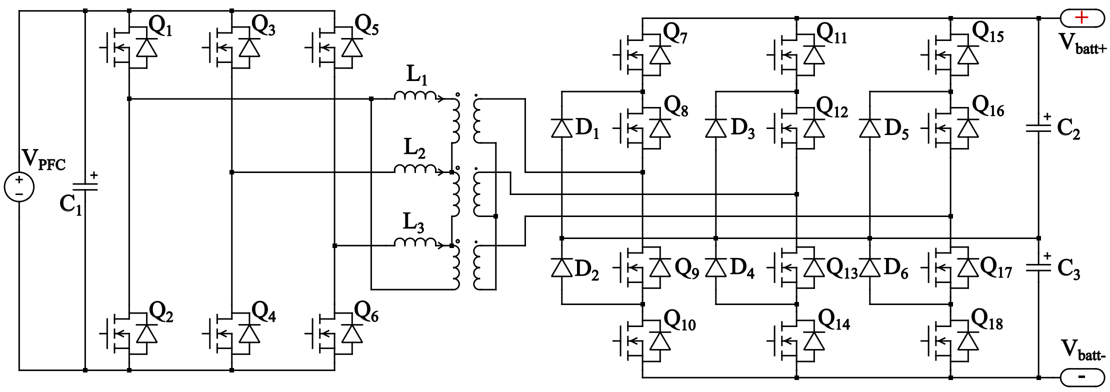

FIGURE 3.7: 2L-3L three-phase dual active bridge (DAB3).

efficiency of 95.5% at 700 V. Fig. 3.7 shows a 2L-3L three-phase dual active bridge converter (DAB3) for solid-state transformers (SST) applications [88]. It is constructed using a three-phase 2L bridge (Q_1-Q_6), three single-phase high-frequency transformers connected in a Δ-Y configuration, leakage inductance, and a three-phase 3L bridge on the high-voltage side. It has been tested for operation from 400 V to 1.5 kV, which makes it suitable for the HV on-board charger application. Efficiency data has not been reported for this configuration, however since the converter has a three-phase operation, it is suitable in building higher power building blocks of an on-board charger compared to all previously discussed topologies.

Table 3.3: Summary of suitable DC-DC converter candidates for high-voltage on-board charging

Bridge 1	Bridge 2	V_{in}	V_{out}	Power	f_{sw}	Eff.	Switches	Power Density	Ref.
3L SHB	3L SHB	800 V	750 V	6.60 kW	500 kHz	97.4%	GaN	7.3 kW/L	[82]
2L FB	3L NPC HB	750 V	1.7 - 2 kV	6.25 kW	100 kHz	97% *	SiC JFET	-	[83]
2L FB	3L NPC FB	292	1.68 kV	3.34 kW	5 kHz	88% †	IGBT	-	[86]
3L NPC FB	3L NPC FB	700 V	200 - 700 V	3.5 kW	50 kHz	95.5%	SiC	-	[87]
3 Φ FB	3 Φ NPC FB	400 V	1500 V	5 kW	50 kHz	-	SiC	-	[88]

* Modeled efficiency data, † 93% efficient transformer

3.1.3 Deployment Capable Designs

Table 3.4 shows the summary of commercial examples of either the sub-systems or the on-board charger. The current work does not cater to a battery voltage > 1 kV, and is limited up to approximately 800 V, and opportunities for commercialization are present. Wolfspeed has developed a 98.5% efficient 22 kW SiC based PFC stage at a 4.6 kW/L power density [89]. Wolfspeed has presented the concept of a SiC based 25 kW PFC stage [90]. Infineon has developed a 97.2% efficient CLLC resonant DC-DC converter for an 800 V class vehicle's on-board charger with a 4.1 kW/L power density [91]. Wolfspeed has developed a 98.5% efficient CLLC resonant DC-DC converter with a 8 kW/L power density [92]. Infineon and ETH Zürich have co-developed a GaN based OBC demonstrator, based on a vienna rectifier PFC and series-parallel dual-active bridge DC-DC conversion stage [93]. EDN and innoelectric have commercialized 800 V class vehicles compatible on-board chargers [94, 95]. It is observed that the commercialized on-board chargers have poor efficiencies compared to a combination of AC-DC and DC-DC converter's reference design efficiency, which can be attributed to need of slowing down the switching operation at the cost of EMI reduction for qualification of regulatory standards for commercialization.

Table 3.4: Summary of reference designs and commercialized on-board charger sub-systems

Converter	Maturity	Manufacturer	Power (kW)	Efficiency	AC Voltage	DC Voltage	Power Density	Reference
DC-DC	Ref. Design	Wolfspeed	22	98.5%	N/A	480-800	8 kW/L	[92]
DC-DC	Ref. Design	Infineon	11	97.2%	N/A	550-800	4.1 kW/L	[91]
AFE	Ref. Design	Wolfspeed	22	98.5%	305-450 V_{LL}	650-900	4.6 kW/L	[89]
AFE	Ref. Design	Wolfspeed	22	-	400-480 V_{LL}	800-900	-	[90]
OBC	Ref. Design	Infineon ETH Zürich	10	-	320-530 V_{LL}	250-1000	10 kW/L	[93]
OBC	Commercial	innoelectric	22	94%	380-480 V_{LL}	400-900	-	[94]
OBC	Commercial	EDN	22	94%	400-480 V_{LL}	up to 840	-	[95]

3.1.4 Regulatory Standards

Since the on-board charger is an electronic sub-assembly (ESA), it is required to comply with certain regulatory standards for safe vehicle operation, interoperability and acceptance to be integrated in the vehicle. Table 3.5 shows a summary of the standards required to be complied in case of the development of an on-board charger. IEEE 519 and IEC 61000-3-2 are power quality regulations to determine the total harmonic distortion (THD) limits beyond which it is forbidden to operate a power converter at a point of common coupling (PCC), which in the context of on-board chargers is an EVSE [66, 96]. CISPR 25, segregated as Class 1 (most lenient) to Class 5 (most stringent) governs the limits of conducted and radiated EMI during the operation of the on-board charger [97]. The scope of the CISPR 25 standard is limited for voltages up to 1 kV, and hence requires re-assessment to be applied for the the 1 - 1.5 kV battery voltage range. To verify the susceptibility of the on-board charger's operation under external EMI imposed on it, ISO 11452-1 to ISO 11452-11 covers the tests related to electromagnetic susceptibility, such as bulk current injection (BCI) and absorber-lined shielded enclosure (ALSE) methods [98, 99]. ISO 10605 describes the test procedures to evaluate

Table 3.5: Summary of regulatory standards applicable to on-board charger development

Standard	Description
IEEE 519 IEC 61000-3-2*	Limits of the harmonics injected into the grid from the EVSE
CISPR 25	Limits of radiated/conducted electromagnetic interference
ISO 11542	Test of the OBC's susceptibility to radiated /conducted electromagnetic interference
ISO 10605	Electrostatic discharge (ESD) susceptibility
ISO 16750	Environmental Stress for ESAs
ISO 26262	Development cycle recommendation for functional safety assessment and design
UL 2202	Electrical safety test for an on-board charger
ISO 15118	Vehicle to grid (V2G) operation's communication interface specifications

* Applicable in Europe [66]

the immunity of a module against electrostatic discharge (ESD) [100]. The environmental stresses such as thermal, humidity, vibration tests are defined by ISO 16750. To reduce the risk of systematic faults in the vehicle, a functional safety compliant development cycle can be utilized if the on-board charger is deemed to be safety-critical in nature based on the system's safety failure mode effects and analysis (S-FMEA) [46]. UL 2202 defines the electrical safety requirements of on-board battery chargers, and the subjected tests are in the category of leakage current, operational safety, vibration, and environmental stress [80]. ISO 15118 defines the requirements of vehicle to grid (V2G) communication for bidirectional discharging/charging of electric vehicles, determines the details of the application protocols requirements for interoperability [101].

3.2 Comparison of DC-DC Converter Topologies

3.2.1 DC-DC Converter Candidates

Two popular candidates for isolated soft-switched topologies are the Dual Active Bridge (DAB) and the LLC converter. These DC-DC converters are popular due to their simple control methods; Modulation of phase shift between the 2 bridges for the DAB and frequency variation in case of the LLC converter. It is found that DAB exhibits higher efficiency compared to the LLC converter at heavy loads, while it is vice versa for light load operation [102]. The converter shall operate under heavy load (>75%) for its entire operating time. Efficient light-load operation, which is one of the key advantages of an LLC converter is not fully exploited in a 800 V OBC application. The LLC converter also contains higher number of resonant components compared to a DAB, and contributes to a larger converter volume. Due to these aspects, various configurations of the DAB shall be evaluated in the further subsections. The Dual Active Bridge and the Multilevel-Dual Active Bridge (ML-DAB) DC-DC converters have been discussed in this section.

Fig. 3.8 and Fig. 3.9 depict the schematics of the topologies, along with the parasitic elements encountered during their construction. $R_{contact}$ is the contact resistance of the converter's termination and current carrying busbar. R_{PCB} is the AC resistance introduced due to the power-plane routing. R_s is the Equivalent Series Resistance (ESR) of the capacitors. R_{pri} and R_{sec} are the AC resistances of the transformer and its interface to the active bridges. The stray inductances on the secondary side of the transformer are lumped as L_k.

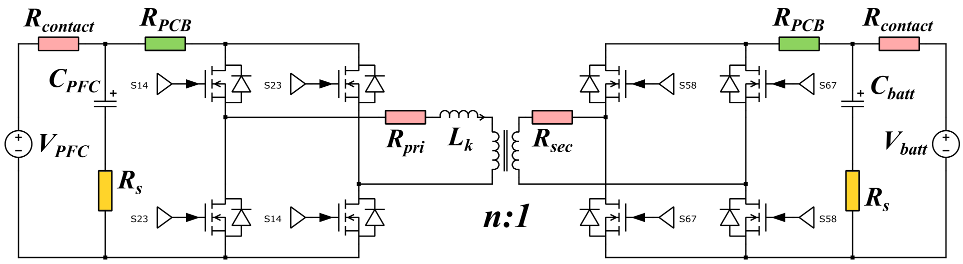

FIGURE 3.8: PLECS based Power Loss Model of a Dual Active Bridge

Dual Active Bridge (DAB) Converter

The Dual Active Bridge, introduced in [103] is a widely used topology for isolated soft-switched applications requiring bidirectional power flow. As shown in Fig. 3.8, it interfaces the output voltage of the PFC stage V_{PFC} and the battery voltage V_{batt} using two active bridges with a switching frequency f_{sw}, an isolation transformer with turns ratio n, and a leakage inductance L_k to enable power transfer across it. The power flow is controlled by the phase shift D_{op} between both the bridges. The expression for power transfer P_{SPS} under single-phase shift modulation is seen in (3.1). The normalized operating phase shift ($-0.5 < D_{op} < 0.5$), as seen in (3.2) is calculated by solving (3.1) for a defined operating point. The soft-switching criterion to ensure Zero-Voltage Switching (ZVS) on the PFC and battery-side bridges is seen in (3.3).

$$P_{SPS} = \frac{nV_{PFC}V_{batt}D_{op}(1 - D_{op})}{2f_{sw}L_k} \tag{3.1}$$

$$D_{op} = \frac{-1 \pm \sqrt{1 - \frac{8nP_{op}f_{sw}L_k}{V_{PFC}V_{batt}}}}{-2} \tag{3.2}$$

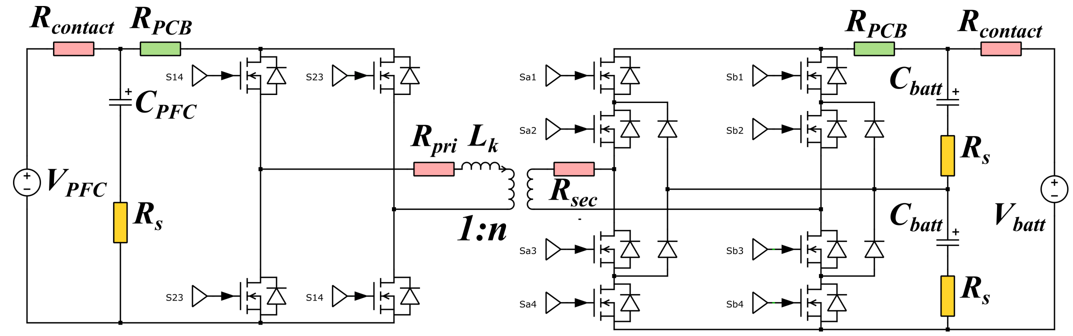

FIGURE 3.9: PLECS based Power Loss Model of a Multilevel-Dual Active Bridge (ML-DAB)

$$\begin{cases} I_1 = \frac{V_{PFC}+nV_{batt}(2D_{op}-1)}{4f_{sw}L_k} > 0 \textit{ (PFC-side ZVS)} \\ \\ I_2 = \frac{V_{batt}(2D_{op}-1)+nV_{PFC}}{4f_{sw}L_k} > 0 \textit{ (Battery-side ZVS)} \end{cases} \tag{3.3}$$

$$I_{L_k(RMS)} = \sqrt{\frac{1}{3}(I_1^2 + I_2^2 + (1-2D_{op})I_1 I_2} \tag{3.4}$$

The resultant RMS current through the leakage inductance $I_{L_k(RMS)}$ for a particular operating point can be calculated as seen in (3.4).

Multilevel-Dual Active Bridge (ML-DAB) Converter

The Multilevel-Dual Active Bridge has been introduced in [86], and is shown in Fig. 3.9. This is particularly used in applications having high conversion gains or for interfacing high-voltage DC buses. Two 3-level neutral-point clamped (3L-NPC) legs are used to generate a 5-level NPC bridge (5L-NPC) on the battery-side, and enables in reducing the switching losses due to reduced dV/dt across each switch. The generalized power transfer equation for the ML-DAB is seen in (3.5), where ϕ_{op} is the phase shift between the 2L and 5L-NPC bridges, and $\alpha + \beta$ is the phase shift between the 5L-NPC bridge's Leg-a and Leg-b. The conversion ratio m is seen in (3.7).

TABLE 3.6: Modulation criterion of a 5L-NPC bridge

Switch	Turn-On Criteria	Turn-Off Criteria
S_{a1}	$t > (t_\alpha + t_\beta)$	$t > (t_\pi + t_\beta)$
S_{a2}	$t > t_\alpha$	$t > (t_\pi + t_\alpha + t_)$
S_{b1}	$t > (t_\pi - t_\alpha)$	$t > (t_{2\pi} - t_\alpha - t_\beta)$
S_{b2}	$t > (t_\pi - t_\alpha - t_\beta)$	$t > (t_{2\pi} - t_\alpha)$

$$P_o = \frac{V_{PFC}V_{batt}}{2\pi f_{sw} n L_k}\left(\phi - \frac{\phi_{op}^2}{\pi} - \frac{\alpha^2}{2\pi} - \frac{\beta^2}{2\pi}\right) \tag{3.5}$$

$$\phi_{op} = \frac{-\pi \pm \pi\sqrt{1 - \left(\frac{8nf_{sw}L_kP_o}{V_{batt}V_{PFC}} - \frac{2\alpha^2}{\pi^2} - \frac{2\beta^2}{\pi^2}\right)}}{-2} \tag{3.6}$$

$$m = \frac{V_{batt}}{nV_{PFC}} \tag{3.7}$$

$$\begin{cases} m < \frac{\frac{\pi}{2}}{\frac{\pi}{2} - \phi_{op}} \ \textit{(PFC-side ZVS)} \\ m > \frac{\pi - 2(\phi_{op} + \beta)}{\pi - 2\beta} \ \textit{(5L-NPC Leg-a ZVS)} \\ m = \frac{\pi - 2(\phi_{op} - \alpha)}{\pi - (\alpha + \beta)} \ \textit{(5L-NPC Leg-b ZVS)} \end{cases} \tag{3.8}$$

Solving (3.5), we get the phase shift between the 2L and 5L-bridges $\left(-\frac{\pi}{2} < \phi_{op} < \frac{\pi}{2}\right)$, for a particular operating point and design configuration, as seen in (3.6). The viability of soft-switching for pre-defined operating points can be established based on (3.8). Since meeting the soft-switching criteria for the NPC Leg-b is challenging, it shall lead to asymmetrical loss distribution on the converter. Unlike the traditional modulation of the two 5L-NPC bridge, the criteria for developing its switching pattern for the is shown in Table 3.6, where $t = time \mod t_{sw}$.

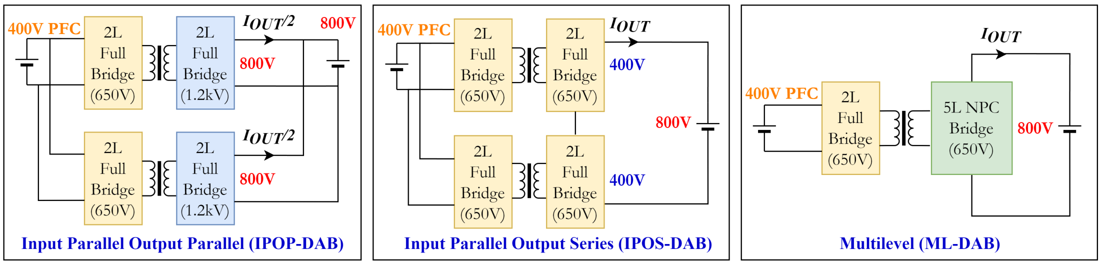

FIGURE 3.10: Possible configurations of the DAB and ML-DAB converters (a) IPOP (b) IPOS (c) ML-DAB

TABLE 3.7: Required components and their ratings for the construction of each DC-DC converter configuration

Converter	400 V PFC-stage				800 V Battery-stage						
	400 V Modules	***650 V FETs***	***Module Current***	***Current Sensors***	***Bridge Config.***	***650 V FETs***	***650 V Diodes***	***1.2 kV FETs***	***Module Current***	***Voltage Sensors***	***Current Sensors***
IPOP-DAB	2	8	$I_{total}/2$	2	FB	0	0	8	$I_{batt}/2$	1	2
IPOS-DAB	2	8	$I_{total}/2$	2	FB	8	0	0	$I_{batt}/2$	2	2
ML-DAB	1	4	I_{total}	1	5L-NPC	8	4	0	I_{batt}	2	1

3.2.2 Configurations of DAB and ML-DAB

This section discusses the viable configurations of the DC-DC converter topologies (DAB and ML-DAB), while considering the limitations of available switching technology, and restricting the total solution cost.

Switching Technology Limitations

The viable semiconductor options being Silicon (Si), Silicon-Carbide (SiC), and Gallium-Nitride (GaN) have their own operational domain limitations. The authors in [104] have summarized the the state-of-art MOSFETs in the market, and few of the key limitations highlighted further. Si MOSFETs available up to a blocking voltage of 900 V are unusable due to insufficient operational voltage margin, and will also limit the switching frequency of the converter. SiC MOSFETs and GaN HEMTs with a blocking voltage of 650 V are viable candidates for the PFC-side, and for the battery-side in a series-connected or multi-level configuration. SiC MOSFETs with a 1.2 kV blocking voltage can be directly used in a

2L configuration on the battery-side, while also providing a 44% margin on its operational voltage.

Total Solution Cost

Lowest manufacturing cost with high reliability is of importance in the automotive sector due to competitive pricing needs, and the push to lower the cost of BEVs. Addition of switches, gate drivers, voltage, and current sensors to achieve high efficiency increases the solution cost and can perhaps make it unusable in the market due to a missed target price point. While designing these configurations, an additional constraint is that the total switch count shall remain the same in all the configurations.

Hardware Redundancy and Modularity

Fault-tolerant operation of elements in the powertrain is an added advantage, if it can be offered at a insignificant cost to an OEM. It adds value to the vehicle operation in case of field failures, where the user can continue operation of the subsystem in a degraded mode. Assuming a DC-DC converter is constructed for its entire operating power, and there is a switching node failure, the converter shall remain out of service, and requires a full replacement. Designing the converter in a multi-module approach shall enable an alternate operational mode, where the DC-DC converter operates at a lower power, while serving its purpose until the user gets an opportunity to service the vehicle. The Tesla Model 3 Power Conversion System (PCS), that contains a 11.5 kW OBC that is constructed using three $\approx$ 4 kW modules [105]. It is showcased in [106] that modules up to $\approx$10 kW can be manufactured while maintaining reasonable cooling complexity. The configurations are hence, split either as one 11.5 kW or two 5.75 kW modules.

Considered Configurations of the DAB and ML-DAB

Fig. 3.10 depicts the potential configurations in which the DAB and the ML-DAB can be configured, while adhering to the above mentioned constraints. The Input Parallel Output Parallel (IPOP-DAB) configuration interfaces two 5.75 kW modules constructed using 650 V switches on the PFC-side, and 1.2 kV switches on the battery-side. Each module shall suffer higher switching losses, but needs to handle half the rated current load current leading to lower conduction losses. It also has the potential for interleaving that helps reducing the size of the battery-side capacitor, along with capability of fault-tolerant operation. The Input Parallel Output Series (IPOS-DAB) configuration interfaces two 5.75 kW modules constructed using 650 V switches on the PFC-side, and 650 V switches on the battery-side, that are serialized to form a DC-link. Fault-tolerant operation is not possible if either of the modules fail. The ML-DAB is constructed using a 11.5 kW module, which is fed by 650 V switches on the PFC-side, and a 5L-NPC bridge on thes battery-side. This configuration is not split into two modules, since the same switch count as the IPOP/IPOS-DAB configurations is maintained. Thus, it shall have higher heat concentration, and is also incapable of a fault-tolerant operation. This configuration suffers from increased currents on both the converter ports, leading to higher conduction losses. The design methods applied for each DC-DC converter is discussed in the next section.

3.2.3 Design Optimization of the DAB and ML-DAB

To have a fair comparison of the efficiency profile of each configuration, all of them shall operate at a switching frequency f_{sw} of 100 kHz. Their operating currents shall be matched to maintain similar conduction losses as well. To ensure this, the converter design parameters (turns ratio n, leakage inductance L_k, PFC-side

MOSFET, battery-side MOSFET) will be curated for each configuration, and the consolidated design parameters are presented in Table 3.8.

3.2.4 IPOP-DAB and IPOS-DAB

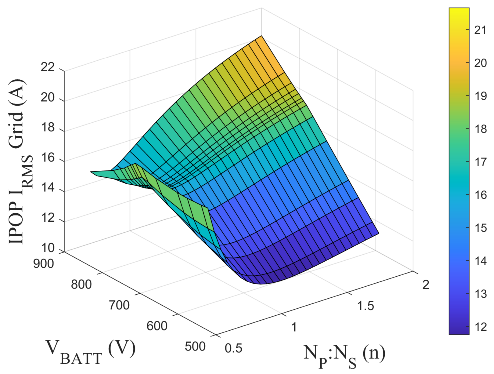

(A) RMS Current Trend (IPOP-DAB)

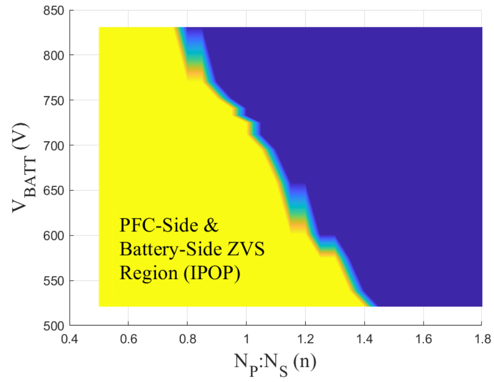

(B) ZVS Criteria (IPOP-DAB)

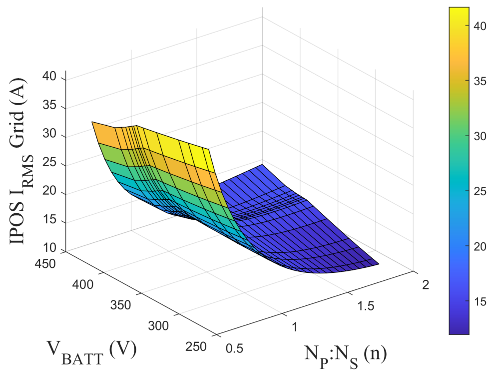

(C) RMS Current Trend (IPOS-DAB)

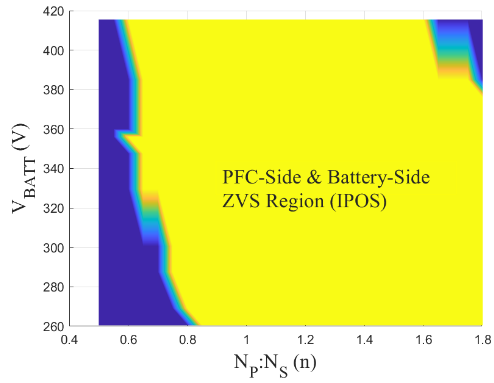

(D) ZVS Criteria (IPOS-DAB)

FIGURE 3.11: Trend of the RMS Current $I_{L_k(RMS)}$ through the Leakage Inductance L_k and soft-switching fulfillment across operating points

The currents handled by the DAB are a function of the operating point of interest, as well as the combination of the leakage inductance and turns-ratio. These operating currents change the profile of the conduction and switching losses within the converter. To minimize the currents, a design methodology based on the *fmincon* non-linear optimization algorithm has been proposed in [107]. This

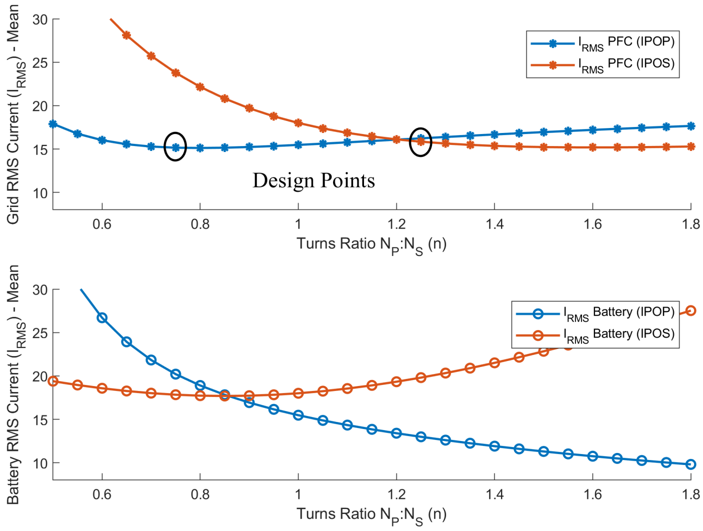

FIGURE 3.12: Mean of $I_{L_k(RMS)}$ for each n, L_k pair

methodology is particularly useful in applications where the loading profile is arbitrary. Since the battery charging profile is fixed, the operating points of interest are known. Using (3.1) and (3.2), the phase shift D_{op} is calculated for every operating point for values of n. The current through the leakage inductance $I_{L_k(RMS)}$ is calculated, and fulfilment of the ZVS criterion as seen in (3.3) is verified. The results of these trends is shown in Fig. 3.11. To decide the design points, the mean of the currents for each pair of n, L_k is taken, and is presented in Fig. 3.12. The configuration with minimum $I_{L_k(RMS)}$ for the PFC-side are chosen as the design points, and the resultant battery-side currents shall be observed. The advantage of paralleling/serialization of the battery-side port can thus be verified for this application.

3.2.5 Multilevel-DAB

As studied in [86], minimum current stress and ZVS of all the switches can be achieved in the ML-DAB when the conversion ratio m is fixed to 1. For the nominal operating voltages of the PFC-side (400 V) and battery-side (712 V), the

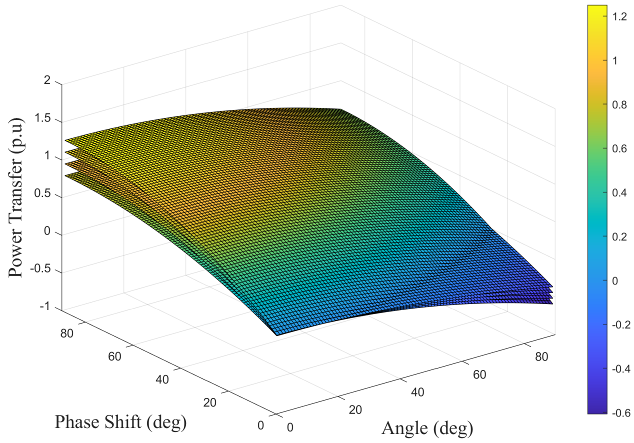

FIGURE 3.13: Relation between ϕ_{op}, β, P_o for α=10° for a ML-DAB

relation between ϕ_{op}, β, P_o for α=10° as seen in (3.5) is shown in Fig. 3.13. It can be observed, as β increases, the capability of the ML-DAB to deliver forward power reduces. For β=10° to β=40°, there is an advantage of one operating point for achieving ZVS on the PFC-side. Hence, β=10°, α=10° are chosen to solve for ϕ_{op} as seen in (3.6). Full-range ZVS across all determined operating points has been achieved on the on the PFC-side and 5L-NPC Leg-a.

Auxiliary Components & Loss-Generating Elements

To realize each of these configurations and evaluate the total solution cost, the following components have been assumed. The isolated half-bridge gate driver and its power supply are UCC21530-Q1 ($1.98), and R15P21503D ($9.22). The voltage and current sensing amplifiers are AMC3330-Q1 ($5.6), and AMC3330-Q1 ($5.6). The loss modelling resistances are $R_{contact}$ = 5mΩ, R_{PCB} = 5mΩ, R_s = 10mΩ, $R_{pri} = R_{sec}$ = 150mΩ, and have been accounted for in the simulation. The assumed transformer efficiency is 99%, and its construction cost is estimated at $150 for the 5.75 kW version, and $250 for the 11.5 kW version.

TABLE 3.8: Simulation parameters and efficiency results of the IPOP-DAB, IPOS-DAB, ML-DAB based 11.5 kW OBC

Config.	n	L_k	PFC-side MOSFET	Battery-side MOSFET, Diode	Elex. Cost @ 10 ku	Average Efficiency	Advantages	Disadvantages
IPOP DAB	0.75	33.1 μH	C3M0060065J	C3M0075120D, N/A	$662.3	96.12%	* Fault-Tolerance Capable * High Efficiency	* High Cost
IPOS DAB	1.25	27.6 μH	C3M0060065J	C3M0045065J1, N/A	$664.7	96.22%	* High Efficiency	* High Cost * No Fault-Tolerance * Needs Cap. Balancing
ML-DAB	1.3	17.2 μH	C3M0025065J1	C3M0045065J1, C3D12065A	$556.1	95.66%	* Low Cost (-16.3%) * Higher DOF	* Low Efficiency (-0.56%) * No Fault-Tolerance * Unequal Heat Distribution * Needs Cap. Balancing

3.2.6 Comparison Summary

This section focuses on defining the priority operating points of a 11.5 kW on-board charger for 800 V BEVs in the G2V mode, and aims in helping designers make quantified trade-offs in system design. A design process is presented for the IPOP-DAB, IPOS-DAB, ML-DAB to perform a comparison, and their simulated efficiency map for the identified priority operating regions is shown in Fig. 3.16. The loss contribution in each configuration from the semiconductors is shown in Fig. 3.15. Table 3.8 contains the qualitative comparison of all configurations. In summary, the IPOS-DAB and IPOP-DAB have a similar cost of electronics. The IPOS-DAB exhibits the highest average efficiency of 96.22% and the IPOP-DAB exhibits an average efficiency of 96.12 %. When fault tolerant operation is of higher priority compared to a 0.1% loss in efficiency, the IPOP-DAB is more suitable. The ML-DAB has the lowest efficiency of 95.66 % (-0.56 % lower), but is advantageous with a -16.3 % cost of electronics compared to the IPOP/IPOS-DAB.

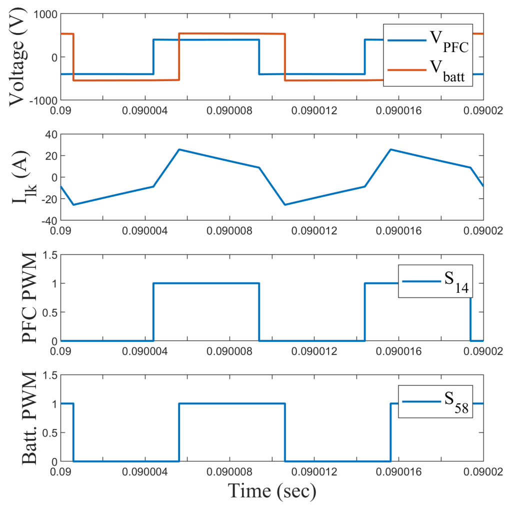

(A) IPOP-DAB

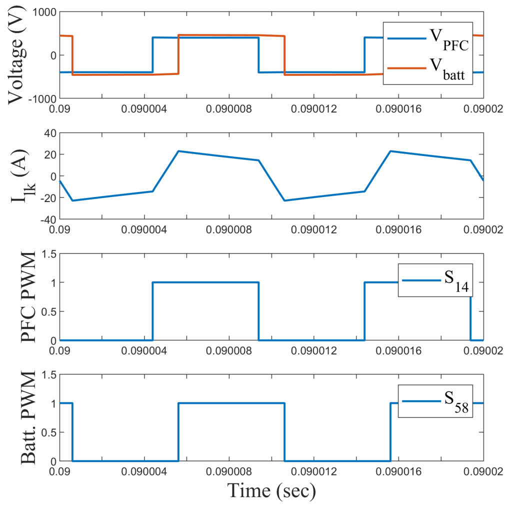

(B) IPOS-DAB

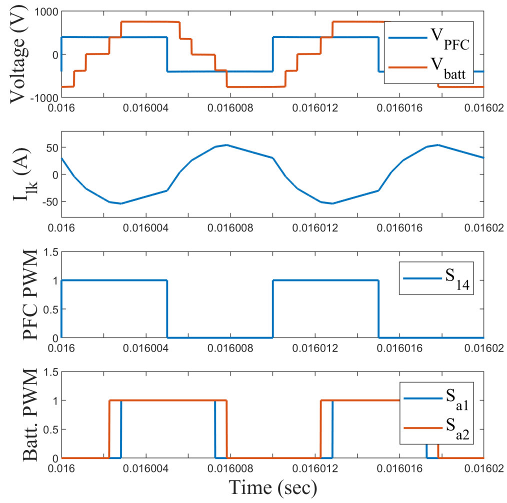

(C) ML-DAB

FIGURE 3.14: Simulation results of PFC-side & Battery-side Bridge Voltages, and Inductor Current at V_{batt} = 712 V, P_{batt}= 11.5 kW

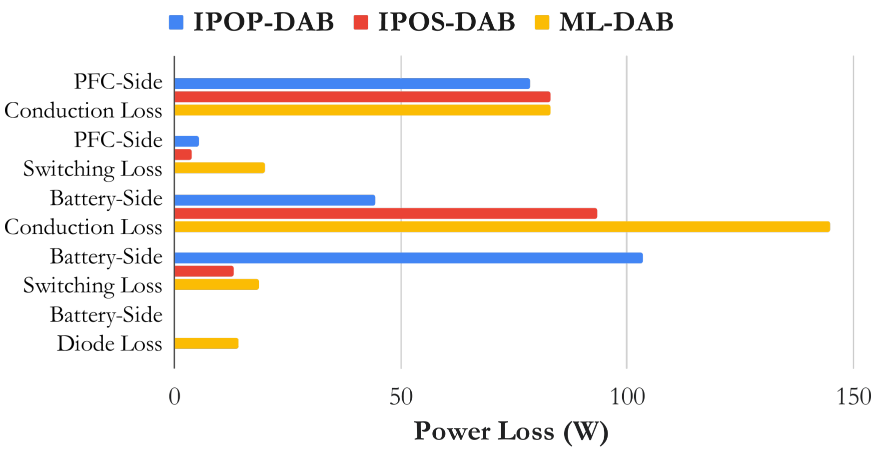

FIGURE 3.15: Loss distribution at V_{PFC}=400 V, V_{batt}=712 V, and P_{out}=11.5 kW

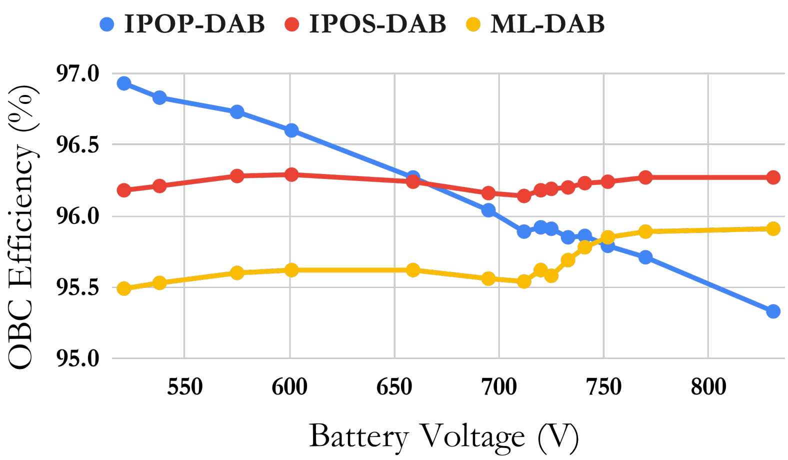

FIGURE 3.16: Efficiency maps of each DC-DC converter configuration

Table 3.9: Required standoff voltages based on number of levels

DC fast charging standard	**Max. Voltage (V)**	**Required Standoff Voltage (V)**		
		2L	3L	5L
ChaoJi/ CHAdeMO 3.0	1500	1950	975	488
Megawatt Charging System (MCS)	1250	1625	813	407

3.3 Challenges in Transition to High-Voltage On-Board Charging

This Section discusses the current gaps in technology to aid the development of performance focused and commercially viable high-voltage compatible on-board chargers while defining the of concern that need to be addressed. Challenges related to the readiness of automotive qualified semiconductors, wide three phase operation in North America, and integration of conductive and wireless charging are discussed.

3.3.1 Automotive Qualified High-Voltage Semiconductors

Table 3.9 shows the required semiconductor standoff voltage as a function of the maximum battery voltage and the number of levels of operation, assuming a 30% voltage derating. Since the on-board charger is an EV sub-system exposed to harsh vibrations, thermal stress, and varying humidity. AEC-Q101 certification of semiconductors is required to pass the reliability qualification requirements and reduce failure rates of deployed sub-systems [108]. In the context of SiC devices, major manufacturers supply devices rated at 650 V, 750 V, 900 V, 1 kV, 1.2 kV, and 1.7 kV [109–111]. Infineon and GeneSiC are the only manufacturers that support 2 kV and 3.3 kV SiC MOSFETs [112, 113]. SiC MOSFETs with standoff voltages up to 15 kV are available, however their maturity is limited to industrial applications. For 2-level operation of the DC-DC converter, focused development of a device class in the 2 kV range would be beneficial for mass adoption, since use of the 3.3 kV device class would provide an over designed safety margin for the said voltage levels. No manufacturers currently support AEC-Q101 qualified devices in the $>$ 1.2 kV device class, and further qualification is required in this segment. 3-level operation can be supported with existing devices.

Since the 1.7 kV device class is a viable candidate for MCS compliant on-board chargers, a comparison is performed based on state-of-the-art devices, and the viability of choosing between 2 or 3-level operation. Table 3.10 shows a comparison of 1.7 kV and 1.2 kV rated devices. Since zero voltage switching (ZVS) is easily possible in resonant converters, turn-on energies have been neglected for brevity. $E_{off(1700)}$ and $E_{off(1200)}$ are the turn-off energies, whereas $R_{ds(on),1700}$ and $R_{ds(on),1200}$ are the on-state resistances of the devices. $P_{loss,adv}$ is a metric that shows the advantage offered by using 1.2 kV devices in a 3-level operation, as compared to 1.7 kV devices in a 2-level operation for a 50% switching and conduction loss distribution, as seen in (3.9). The cost of constructing an M-level NPC bridge C_{ML}, where M is the number of voltage levels, C_{MOS}, C_{drv}, C_{PS}, C_D are the cost of the MOSFET, gate driver, gate driver power supply and clamping diodes quoted at 10,000 units, as seen in (3.10) [114].

$$P_{loss,adv} = 1 - \frac{1}{2}\left(\frac{2.E_{off,1200}}{E_{off,1700}} + \frac{R_{ds(on),1200}}{R_{ds(on),1700}}\right) \tag{3.9}$$

$$C_{ML} = 4(M-1)(C_{MOS} + C_{drv} + C_{PS}) + 4(M-2)C_D \tag{3.10}$$

Table 3.10: Cost and normalized loss comparison of a 2L and 3L converter based bridge for a 1.25 kV on-board charger

Manufacturer	1700 V Part	$R_{ds,1700}$	$E_{off,1700}$	1200 V Part	$R_{ds,1200}$	$E_{off,1200}$	$P_{loss,adv}$	C_{2L}	C_{3L}
GeneSiC	G3R20MT17K	20 $m\Omega$	300 μJ at V_{ds} = 1.2 kV I_{ds} = 30 A	G3R20MT12K	20 $m\Omega$	50 μJ at V_{ds} = 600 V I_{ds} = 30 A	33%	$433	$377
Wolfspeed	C2M0045170P	45 $m\Omega$	220 μJ at V_{ds} = 1.2 kV I_{ds} = 30 A	C3M0040120K	40 $m\Omega$	60 μJ at V_{ds} = 600 V I_{ds} = 30 A	28%	$364	$268

Table 3.10 shows a normalized power loss and cost comparison of choosing to construct a 1.25 kV compatible full bridge using a 2-level or 3-level NPC converter. On an average, the 3-level converter based option provides about 31% advantage in the total power losses. Despite the addition of added gate drivers and clamping diodes, the 3-level NPC based option costs about -20% lower. This also highlights the disparity in the switching energy and cost that needs to be addressed by SiC semiconductor manufacturers for OEMs to choose between 2-level and 3-level operation.

GaN HEMTs aid in increasing the converter's operating frequency, and thus reduce the size of the magnetics. Production GaN HEMTs are available at a maximum voltage of 900 V [104]. Hence in this case, a 3-level operation is not supported only in the MCS case, while a Chaoji compliant GaN based solution requires 5-level operation.

3.3.2 Wide Three-Phase Voltage in North America

As shown in Fig. 3.17, in the U.S., 208/120Y and 480/277Y are the common three-phase voltages, while in Canada, 208/120Y and 600/347Y are the common voltages for three-phase LV distribution [115]. Due to shared land borders and economic co-dependency between the U.S. and Canada, $828 billion of North American

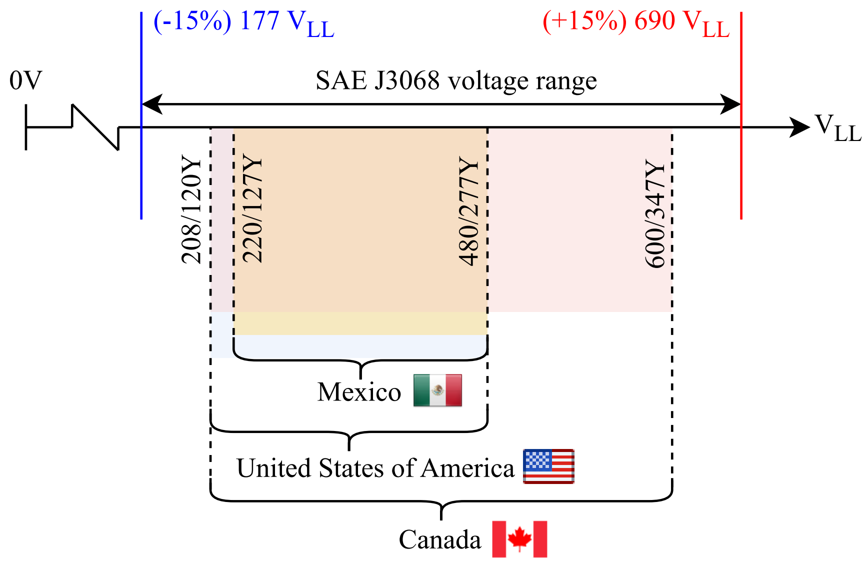

FIGURE 3.17: Three phase voltage ranges North America

transborder freight was accounted in the year 2021 [18]. Due to this reason, the on-board charger in medium and heavy-duty vehicles is required to support voltages from 208-600 V_{LL}, as shown in Table 3.1. The minimum line-line voltage is 208 V_{LL}, while the maximum line-line voltage is 600 V_{LL}. SAE J3068 requires the on-board charger to accept $\pm15\%$ voltage sag or swell on its input voltage capability communicated to the electric vehicle supply equipment (EVSE) [55]. This results in a required input voltage range of 177-690 V_{LL}, and the on-board charger must be designed to operate efficiently throughout this voltage range. *Zayed et al.* have proposed a reconfiguration mechanism for a partially-paralleled dual active bridge converter (P^2DAB) to improve the charging efficiency for a wide-output (200 V - 1000 V) DC fast charger [116]. The proposed converter is bidirectional in nature, and can be adopted in the reverse direction to address this challenge.

3.3.3 Integration with Wireless Charging

SAE J2954 is a standard developed for wireless power transfer (WPT) of power levels up to 3.3 kW, 7.7 kW, 11 kW, and 22 kW [117]. The standard mandates that vehicles compliant with SAE J2954 should also support conductive charging via SAE J1772. Recently, SAE has released an initial specification of SAE TIR J2954/2, which defines higher power levels up to 500 kW for both dynamic and static WPT of medium and heavy-duty electric vehicles [118]. This standard is an initial release, and does not recommend OEMs to comply to it as of now. Further updates to this version requires considering the voltage level compatibility with MCS and ChaoJi/ CHAdeMO 3.0. System integration of co-dependency considering wireless charging and on-board charging for high-voltage powertrain applications has significant research potential.

Chapter 4

Proposed Wide-Input Reconfigurable Three-Level Dual Active Bridge (R3L-DAB) Converter

4.1 Reconfigurable Neutral-Point Clamped Converter

As the conversion ratio of a dual active bridge converter deviates from unity, the circulating current in the converter increases, resulting in an increase in transformer and switch RMS and peak current, increased conversion effort (bucking or boosting operation) and a detrimental impact on efficiency [119]. Various modulation techniques have been proposed in literature to improve the ZVS range and peak current stress of the dual active bridge converter that result in improved efficiency [107]. Topology morphing control (TMC) is a method where the bridge of a dc/dc converter is switched between half- or full-bridge mode depending upon the DC link voltage, in order to reduce the extent of the voltage swing observed by the high-frequency link [120]. At lower DC link voltages, the bridge is configured in the full-bridge mode, while at higher DC link voltages, it is configured in the half-bridge mode, thus ensuring reduced voltage swing across the bridge output.

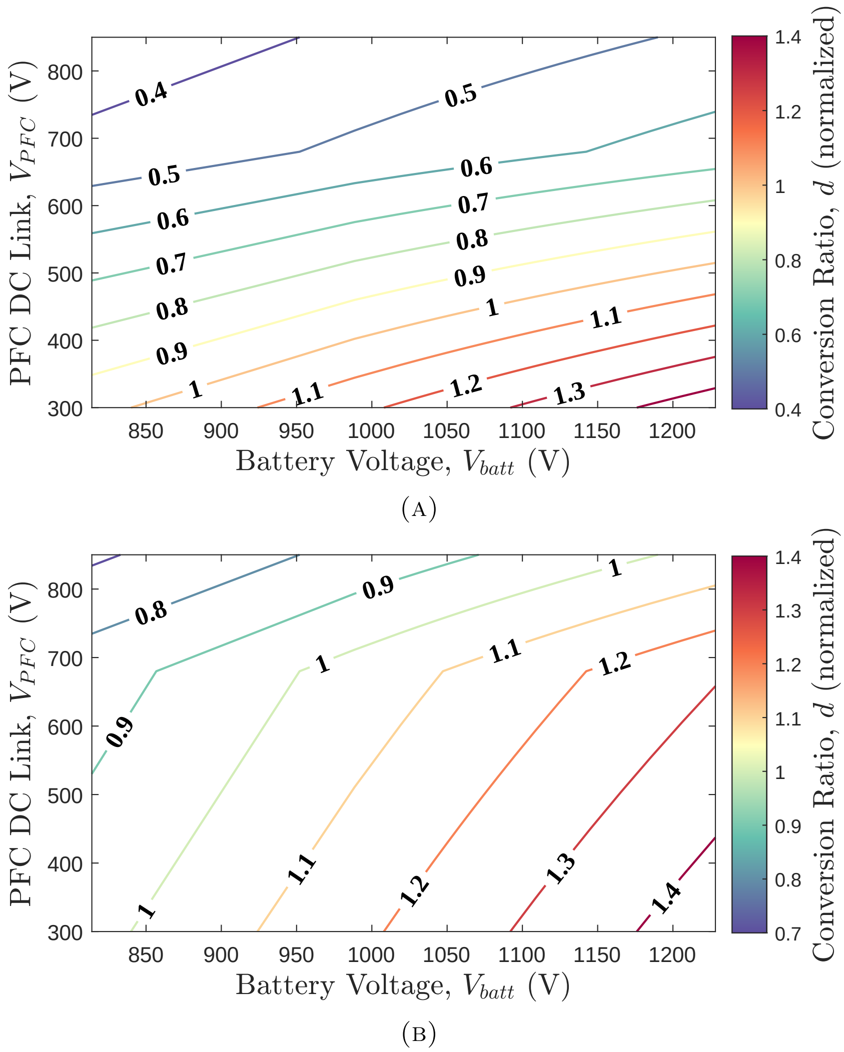

FIGURE 4.1: (a) Conversion gain without topology morphing control. (b) Conversion gain with topology morphing control.

$$d = \frac{V_B}{nV_P k_{config}} \tag{4.1}$$

TABLE 4.1: Vector matrix of the NPC and RNPC converters.

S_5	S_6	S_7	S_8	S_9	**Vector**	**Output referred to 'n'**	**Converter**
1	1	0	0	X	P	$+V_P/2$	NPC/ RNPC
0	1	1	0	X	O	0	NPC/ RNPC
0	0	1	1	X	N	$-V_P/2$	NPC/ RNPC
0	0	1	0	1	R	0	RNPC only

The conversion ratio d is defined by (4.1), and is a function of the output voltage V_B, input voltage V_P, secondary to primary turns ratio n, and the configuration factor k_{config}, which is set to 1 while operating in full-bridge mode, and is set to 0.5 while operating in half-bridge mode. Fig. 4.1(a) shows the contour map of d, when the converter's primary is operated in full-bridge mode, without any topology morphing control, and the range of d is 0.34 - 1.46. Fig. 4.1(b) shows the contour map of d, when the converter's primary is operated in full-bridge mode when $V_{PFC} = 300$ V, and in half-bridge mode when $V_{PFC} = 680/850$ V, and the range of d reduces to 0.68 - 1.46.

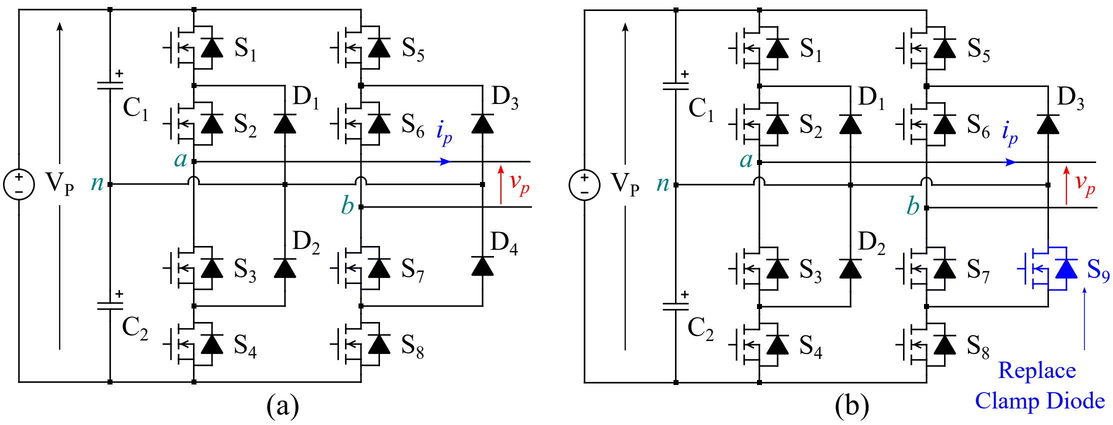

FIGURE 4.2: (a) Conventional neutral-point clamped converter (b) Reconfigurable neutral-point clamped (RNPC) converter

Fig. 4.2(a) shows a conventional three-level neutral point clamped (NPC) converter. C_1, C_2 are the DC link capacitors, S_1-S_8 are the MOSFETs, while D_1-D_4

are the clamped diodes. Considering leg B of the converter, $S_5 = \overline{S_7}$ and $S_6 = \overline{S_8}$, and are modulated with separation of dead-time. Fig. 4.2(b) shows the proposed three-level reconfigurable neutral-pointed clamped (RNPC) converter, and is created when D_4 in a conventional NPC converter is replaced with a MOSFET S_9. Table 4.1 shows the vector table of the conventional NPC converter and RNPC converter. It can be seen that the 'O' and 'R' vectors develop 0 V referenced to the 'n' potential, however the 'R' vector can be only developed in the RNPC converter, and their differences are highlighted further.

To operate either of the converters in the full-bridge mode, the modulation scheme representing the P/O/N vectors can be individually applied to either of the legs, and the output voltage swing $v(t) = \pm V_P$. To operate a NPC converter in the half-bridge mode, S_6 and S_7 are turned on, resulting in a 'O' vector on leg B, and limiting the output voltage swing $v(t) = \pm V_P/2$. The reconfiguration power loss in a NPC, $P_{hb(NPC)}$ is given by (4.2), where $i_{p(rms)}$ is the RMS current handled by the bridge, $R_{ds(on)}$ and R_d are the on-state resistances of the MOSFETs and clamp diodes, V_{T0} is the clamp diode threshold voltage.

$$P_{hb(NPC)} = i^2_{p(rms)} \left(R_{ds(on)} + R_d + \frac{\sqrt{2} V_{T0}}{i_{p(rms)}} \right) \tag{4.2}$$

To operate the RNPC converter in the half-bridge mode, S_7 and S_9 are turned on, resulting in a 'R' vector on leg B. The reconfiguration power loss in a RNPC, $P_{hb(RNPC)}$ is seen in (4.3).

$$P_{hb(RNPC)} = 2 i^2_{p(rms)} R_{ds(on)} \tag{4.3}$$

The reconfiguration power losses in an active neutral-point clamped (ANPC) converter, $P_{hb(ANPC)}$ is seen in (4.4) [121].

$$P_{hb(ANPC)} = i^2_{p(rms)} R_{ds(on)} \tag{4.4}$$

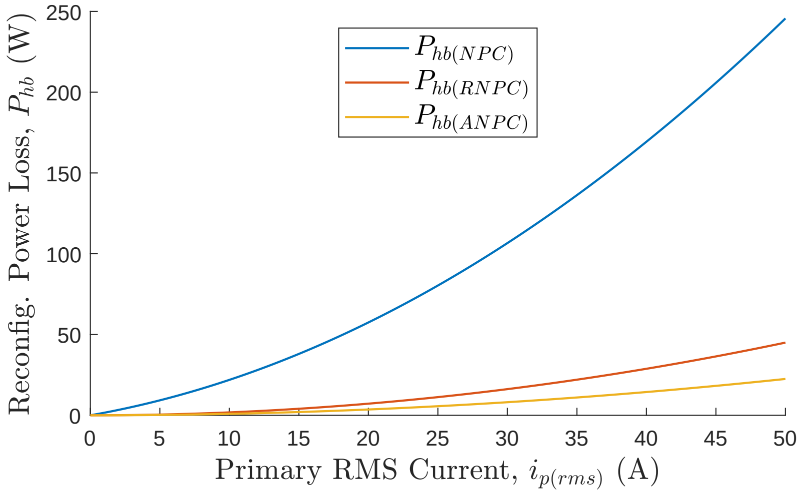

FIGURE 4.3: Reconfiguration power loss as a function of handled RMS current

Fig. 4.3 shows the comparison in the reconfiguration power loss of the NPC, RNPC and ANPC converters, when $R_{ds(on)} = 9$ mΩ, $R_d = 59$ mΩ, and $V_{T0} = 1.07$ V. Comparing the losses when $i_{p(rms)} = 50$ A, the losses are 245 W, 44 W, and 22 W, for the NPC, RNPC, ANPC converters, respectively. The losses of a conventional NPC converter are incomparable to the RNPC or the ANPC, and makes it unsuitable for topology morphing control at high RMS current levels. Multiple strategies have been proposed in literature to increase the voltage range of resonant power converters, however they utilize additional relays or contactors for reconfiguration [82, 122, 123]. The proposed reconfiguration method does not require any additional relays or contactors, and is solid-state in nature. This improves the reliability of the application, since utilization of electromechanical devices with a fatigue life affected by vehicle vibrations is a cause of concern in an on-board charger application. Additionally, the RNPC converter saves the cost of one gate driver and MOSFET compared to using an ANPC converter, and provides a reconfiguration option with a lower switch-count in its comparison, thus providing a trade-off for cost-sensitive applications.

4.2 Operating Principle of the Reconfigurable Three-Level Dual Active Bridge Converter

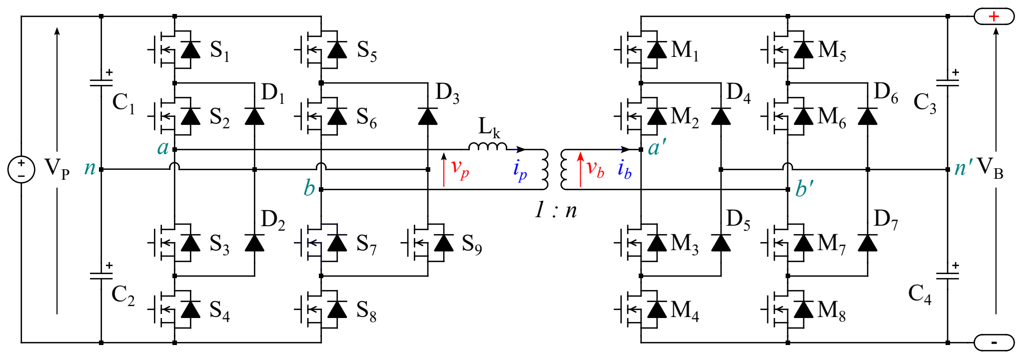

FIGURE 4.4: Topology of reconfigurable three-level dual active bridge converter (R3L-DAB) converter

Fig. 4.4 shows the construction of a reconfigurable three-level dual active bridge (R3L-DAB) converter topology. The stage fed by the input voltage, V_P, referred to as primary side is interfaced with a reconfigurable neutral-point clamped converter. The high-frequency link is generated using the system's total leakage inductance, L_k and isolation transformer with a secondary to primary turns ratio, n. The secondary winding of the transformer is interfaced with a full-bridge neutral-point clamped converter, that generates the output DC link, V_B, and is referred to as the secondary side. $C_1 - C_4$ are the DC link capacitors, $S_1 - S_9$ are the MOSFETs of the primary RNPC converter, $M_1 - M_8$ are the MOSFETs of the secondary NPC converter, $D_1 - D_7$ are the clamp diodes. The DC link with the larger voltage swing is intended to interface with the primary side with the RNPC converter stage, that is connected to V_P.

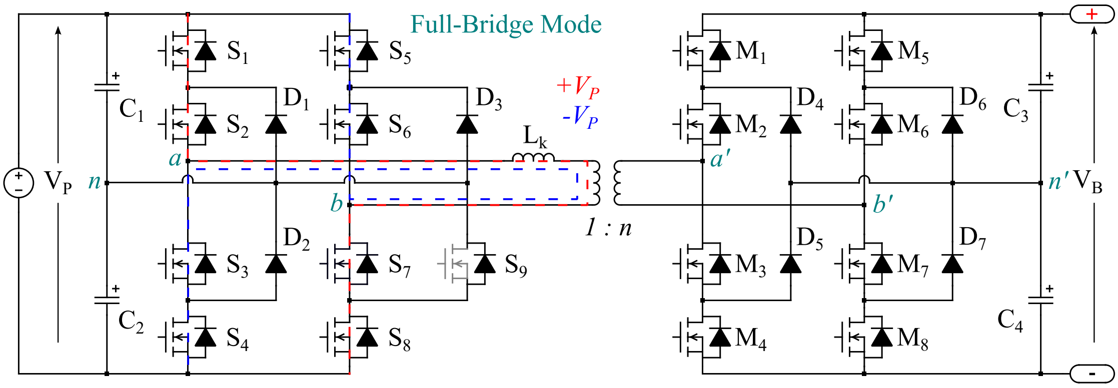

(A)

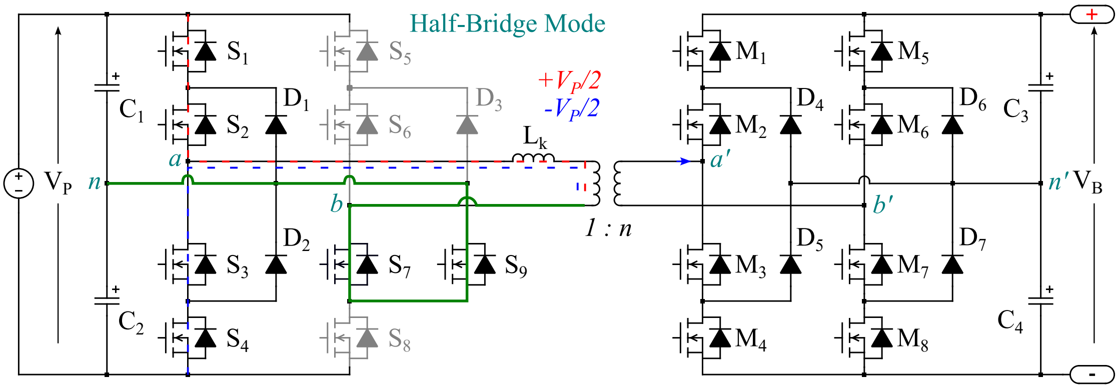

(B)

FIGURE 4.5: (a) Reconfigurable three-level DAB in full-bridge mode. (b) Reconfigurable three-level DAB in half-bridge mode.

Fig. 4.6 shows the operating modes of the R3L-DAB converter. The modulation scheme is defined as the following; the primary side can operate either in the full-bridge or the half-bridge mode, depending upon the state of the reconfiguration MOSFETs, S_7 and S_9. Fig 4.5(a) shows the R3L-DAB in the full-bridge mode. The gate command of switch S_9 is maintained at logic 0, to disable the MOSFET channel, and only let its body diode conduct to serve as a clamp diode. The voltage swing observed by the transformer primary, v_p is $\pm V_P$. Fig. 4.5(b) shows the R3L-DAB in the half-bridge mode, which is done by permanently turning on S_7

and S_9. This creates a permanent connection between nodes *'b'* and *'n'*, resulting in a maximum transformer voltage swing, v_p of $\pm V_P/2$. The primary excitation is limited to a two-level operation, however can be further extended to three-level (half-bridge) or five-level (full-bridge) operation to optimize the switching currents based on the available degrees of freedom [124]. The secondary excitation is controlled by two phase shifts, D_1 and D_2, and generates a five-level waveform $(+V_P, +V_P/2, 0, -V_P/2, -V_P)$. The power transfer between the two ports is controlled by the phase shift, φ between the primary and secondary bridge voltages, referenced to their zero position.

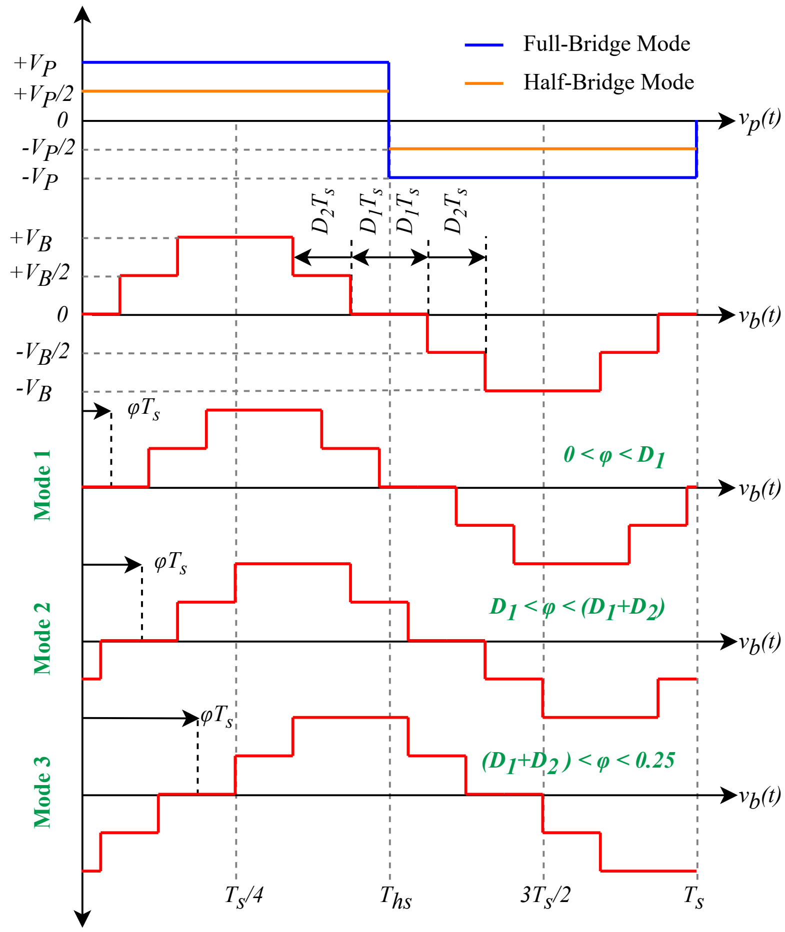

FIGURE 4.6: Operating modes of the R3L-DAB converter.

The normalized values of all control variables, 0 - 1 translates as 0 - T_s seconds, or 0 - 2π radians. These control variables are bound by the following conditions: $-0.25 < \varphi < 0.25$ ($\varphi > 0$ to transfer power from V_P to V_B and $\varphi < 0$ to transfer power from V_B to V_P). $D_1 + D_2 \leq 0.25$. In order to facilitate power transfer from V_P to V_B, $\varphi > 0$ has been assumed for the analysis. Mode 1 refers to a condition when $0 < \varphi < D_1$. Mode 2 refers to a condition when $D_1 < \varphi < (D_1 + D_2)$. Mode 3 refers to a condition when $(D_1 + D_2) < \varphi < 0.25$. Each of these modes are applicable when the R3L-DAB is operated either in the full-bridge or the half-bridge configuration.

The modulation technique of the R3L-DAB converter in operating mode 3, with the primary gating signals $S_1 - S_9$, secondary gating signals $M_1 - M_8$, transformer primary voltage v_p, inductor voltage v_L, secondary voltage v_b, and inductor current i_p are shown in Fig. 4.7. In the full-bridge mode, the relationship between the gating signals is as $S_1 = \overline{S_3}$, $S_2 = \overline{S_4}$, $S_5 = \overline{S_7}$, $S_6 = \overline{S_8}$, and is applicable for $M_1 - M_8$ in the same order. The complementary signals are separated by the dead time t_{dead} at the turn-off interval, and is depicted in the intervals $t'_x - t_x$, where $x \in \{0..12\}$. t_6 is represented by the half-cycle period T_{hs} and t_{12} is represented by switching period T_s. The primary side, connected to the RNPC converter can be operated either in full-bridge or half-bridge mode, and generates a 2-level waveform. The secondary side, connected to the NPC converter is operated in the full-bridge mode, and generates a five-level waveform.

The modulation criterion for the R3L-DAB converter in operating mode 3 for both full-bridge and half-bridge operation is summarized in Table 4.2. The relationship to the complementary switches in the bridge have been summarized in the previous subsection. The specified modulation criterion is valid for mode 3 in the

TABLE 4.2: Switching conditions of the R3L-DAB converter in Mode 3.

Switch	**Turn-on instance t_{on}**	**Turn-off instance t_{off}**
$S_{1,2}$	0	T_{hs}
$S_{5,6}$	T_{hs}	T_s
$S_{5,6,8}$	Always off (half-bridge)	
$S_{7,9}$	Always on (half-bridge)	
M_1	$(\varphi + D_1 + D_2)T_s$	$(2\{\varphi + D_1\} + 1)T_{hs}$
M_2	$(\varphi + D_1)T_s$	$(2\{\varphi + D_1 + D_2\} + 1)T_{hs}$
M_5	$(2\{\varphi - D_1\} + 1)T_{hs}$	$(\varphi - D_1 - D_2)T_s$
M_6	$(2\{\varphi - D_1 - D_2\} + 1)T_{hs}$	$(\varphi - D_1)T_s$

forward power mode ($0 < \varphi < 0.25$), however can be mapped for realization on a digital signal processor (DSP) or field programmable gate array (FPGA) for modes 1, 2, and reverse power mode ($-0.25 < \varphi < 0$) provided the necessary overflow conditions of the PWM modules are managed according to the implementation platform.

The current paths of the R3L-DAB in a full-bridge mode 3 operation are shown in Fig. 4.8(a)-(j) and Fig. 4.9(a)-(j). The direction of currents and the switches undergoing ZVS at various instances have been shown in the figures. The secondary side current paths and their intervals during the half-bridge mode 3 operation remains the same as Fig. 4.8(a)-(j) and Fig. 4.9(a)-(j), however the primary bridge current paths are shown in Fig 4.10(a)-(d).

The modulation scheme of the R3L-DAB converter in Mode 1 and Mode 2 operation are shown in Fig. 4.11 and Fig. 4.12. The modulation schemes highlighted in this section are used to derive the steady-state currents in the next subsection.

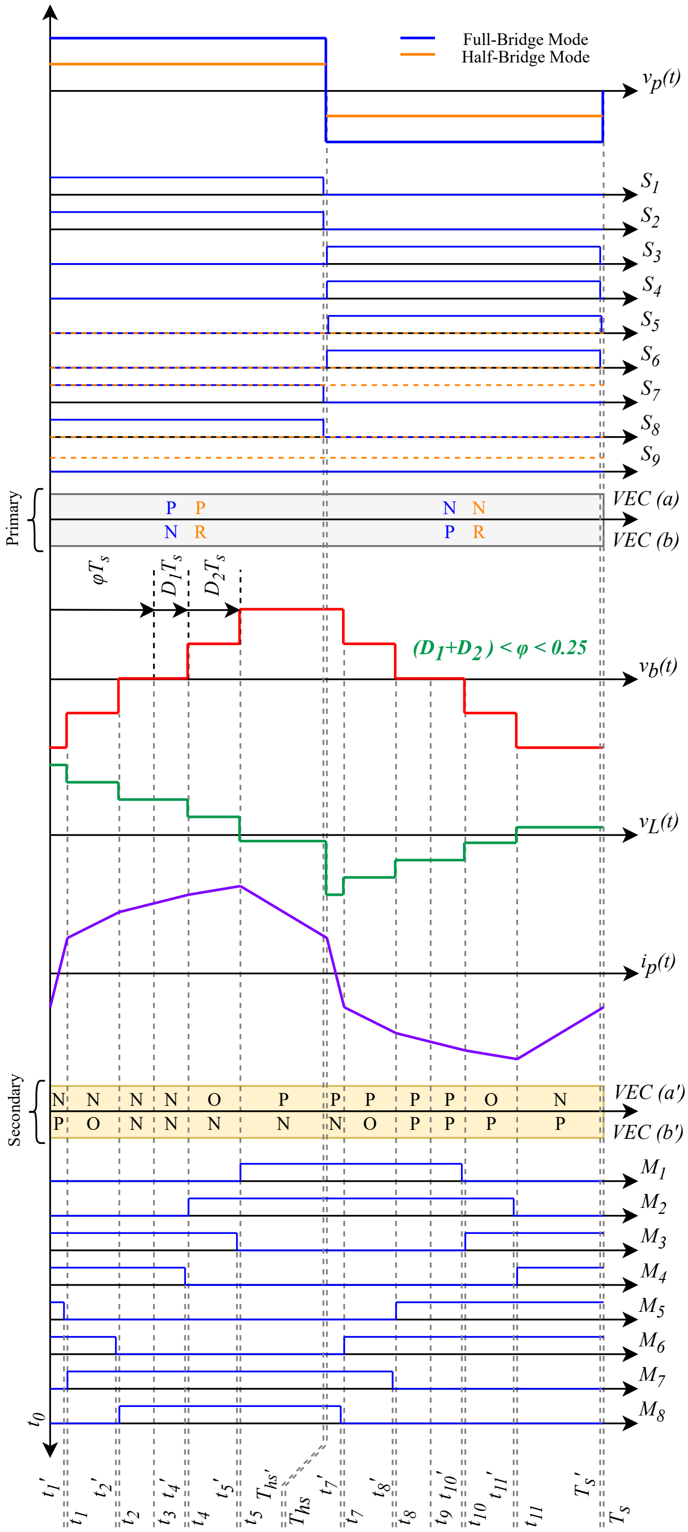

FIGURE 4.7: Modulation scheme of the R3L-DAB converter in mode 3.

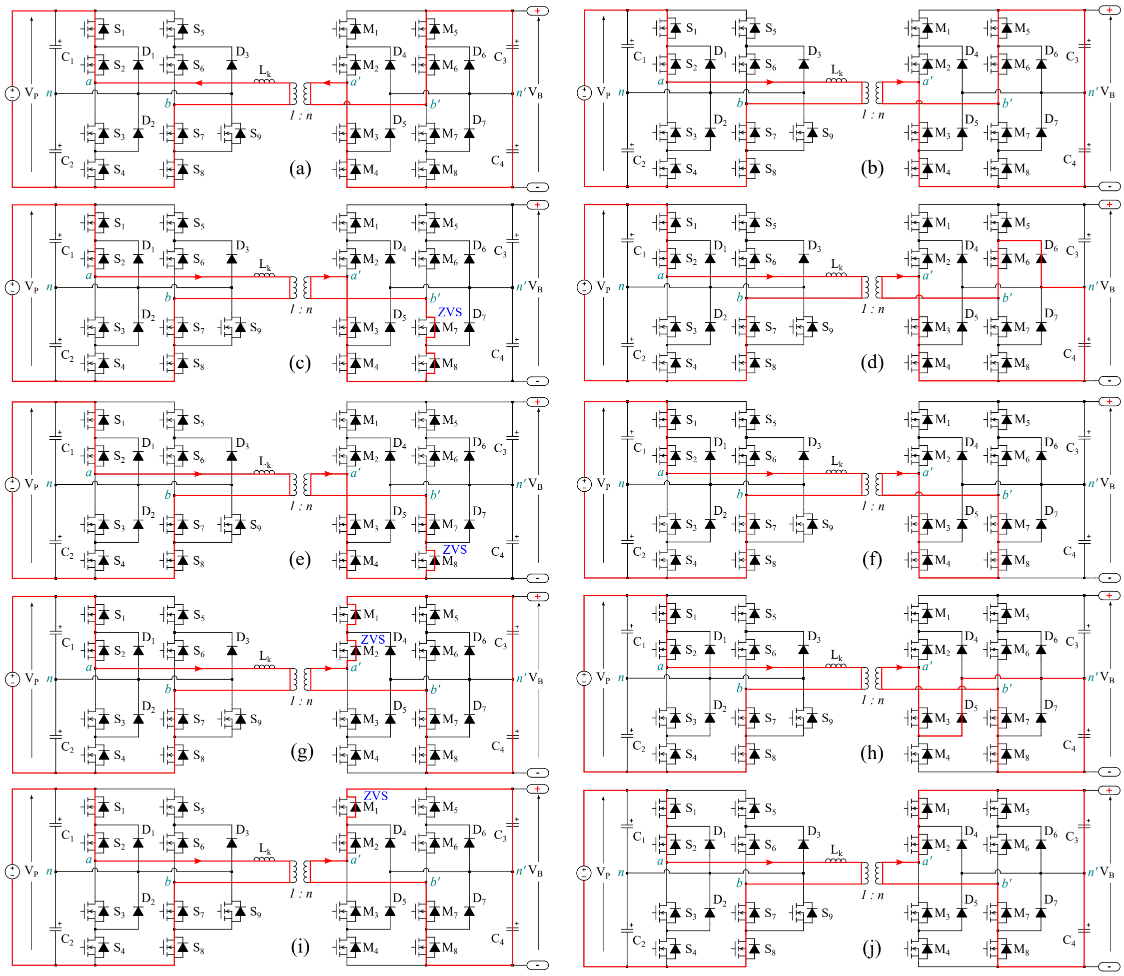

FIGURE 4.8: Operation of the R3L-DAB in full-bridge Mode 3 $(D_1 + D_2) < \varphi < 0.25$; (a) and (b) Current path from $t_0 - t_1'$, (c) Current path from $t_1' - t_1$, (d) Current path from $t_1 - t_2'$, (e) Current path from $t_2' - t_2$, (f) Current path from $t_2 - t_4'$, (g) Current path from $t_4' - t_4$ (h) Current path from $t_4 - t_5'$, (i) Current path from $t_5' - t_5$, (j) Current path from $t_5 - T_{hs}'$

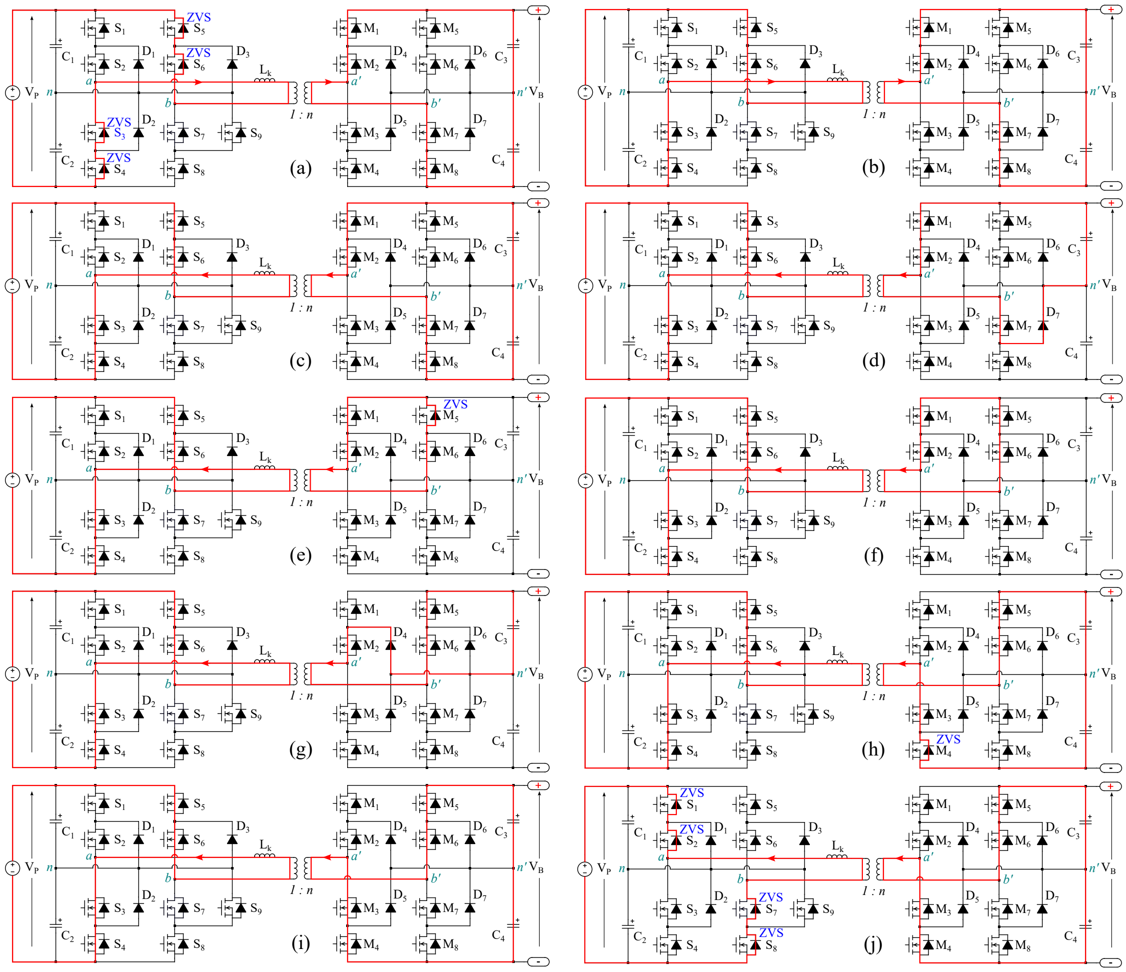

FIGURE 4.9: Operation of the R3L-DAB in full-bridge Mode 3 $(D_1 + D_2) < \varphi < 0.25$; (a) Current path from $T'_{hs} - T_{hs}$, (b) and (c) Current path from $T_{hs} - t'_7$, (d) Current path from $t'_7 - t'_8$, (e) Current path from $t'_8 - t_8$, (f) Current path from $t_8 - t'_{10}$, (g) Current path from $t'_{10} - t'_{11}$, (h) Current path from $t'_{11} - t_{11}$, (i) Current path from $t_{11} - T'_s$, (j) Current path from $T'_s - T_s$,

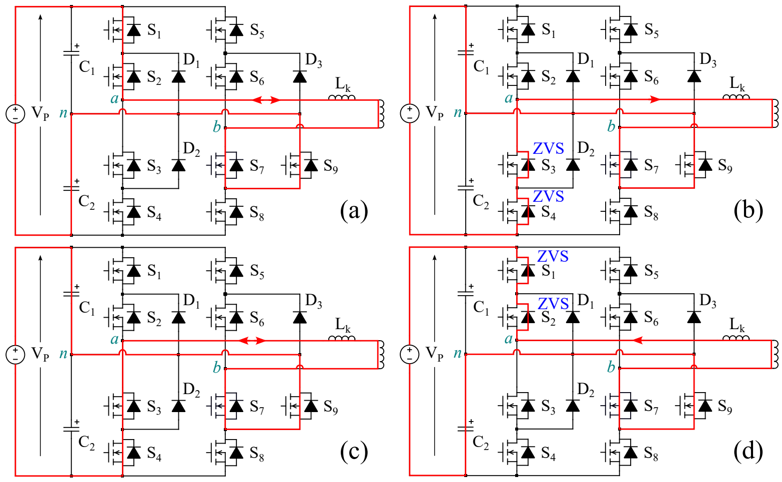

FIGURE 4.10: Operation of the R3L-DAB in half-bridge Mode 3 $(D_1+D_2) < \varphi < 0.25$, $k_{config} = 0.5$; (a) Current path from $t_0' - T_{hs}'$, (b) Current path from $T_{hs}' - T_{hs}$, (c) Current path from $T_{hs} - T_s'$, (d) Current path from $T_s' - T_s$.

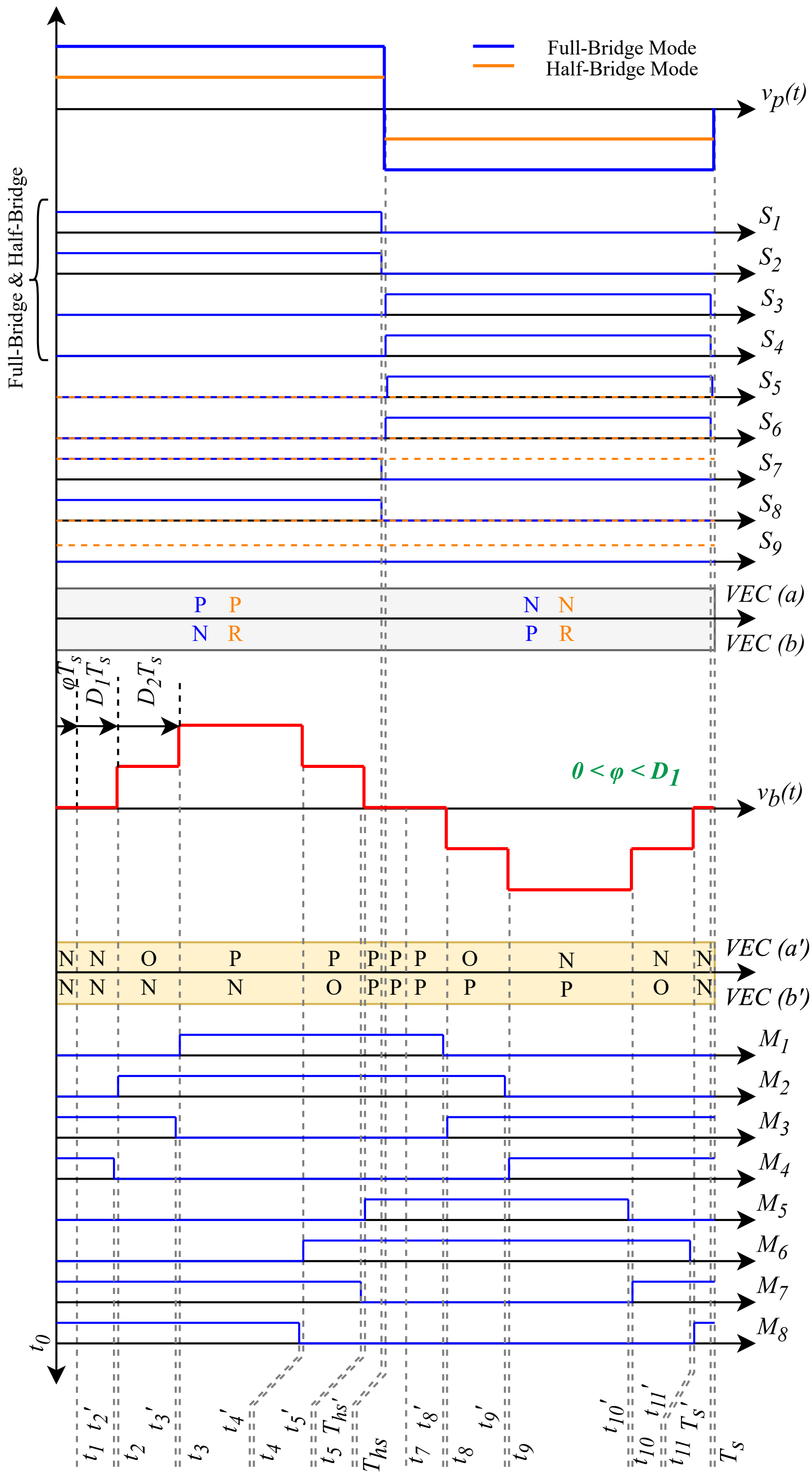

FIGURE 4.11: Mode 1 modulation of the R3L-DAB converter.

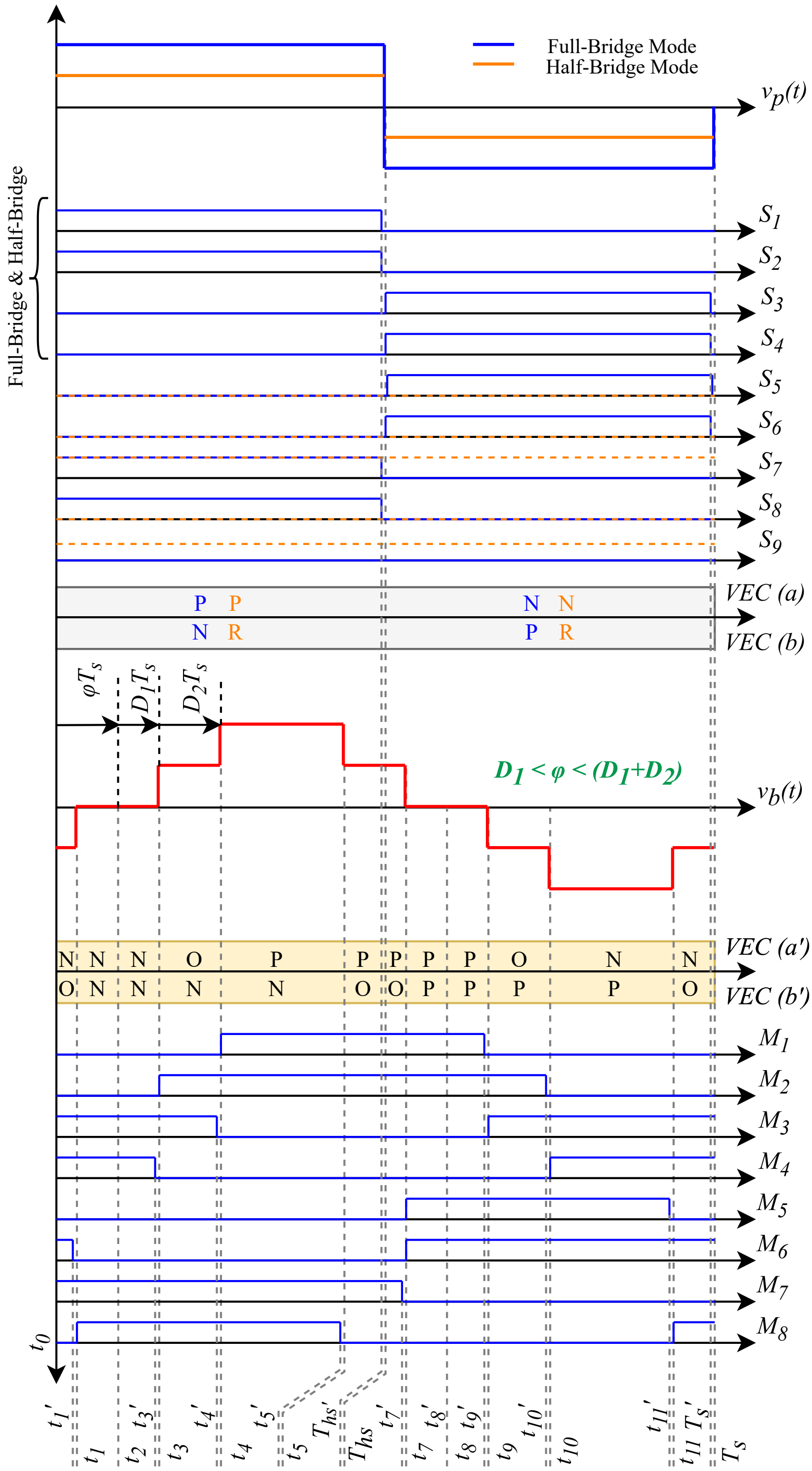

FIGURE 4.12: Mode 2 modulation of the R3L-DAB converter.

4.3 Steady-State Analysis of the Reconfigurable Three-Level Dual Active Bridge Converter

This section discusses the steady-state analysis of the R3L-DAB converter in all modes of operation. The closed-form solution of the steady-state instantaneous currents in the leakage inductance $i_p(t)$, the RMS current in the leakage inductance $i_p(rms)$, the RMS currents in the various switches of the R3L-DAB based on the above mentioned modulation schemes are derived in this section.

Due to the modulation of the R3L-DAB converter, there are discontinuities observed in the voltages seen by the primary and secondary bridges. The time instance t_x, where $x \in \{1..12\}$ are unique in all modes of operation. In all modes of operation, the time instances are defined as a function of D_1, D_2, φ and T_s are seen in (4.5), (4.6), (4.7). These equations compute the value of time instances $t_0 - t_6$. The waveforms follow half-wave symmetry and $t_7 - t_{12}$ can be further calculated based on this relation.

$$t_x(\text{Mode 1}) = \begin{cases} t_0 = 0 \\ t_1 = \varphi T_s \\ t_2 = (D_1 + \varphi)T_s \\ t_3 = (D_1 + D_2 + \varphi)T_s \\ t_4 = (1 - 2(D_1 + D_2 - 2\varphi))0.5T_s \\ t_5 = (2\varphi - 2D_1 + 1)0.5T_s \\ t_6 = T_{hs} \end{cases} \tag{4.5}$$

$$t_x(\text{Mode 2}) = \begin{cases} t_0 = 0 \\ t_1 = (\varphi - D_1)T_s \\ t_2 = \varphi T_s \\ t_3 = (D_1 + \varphi)T_s \\ t_4 = (D_1 + D_2 + \varphi)T_s \\ t_5 = (1 - 2(D_1 + D_2 - 2\varphi))0.5T_s \\ t_6 = T_{hs} \end{cases} \tag{4.6}$$

$$t_x(\text{Mode 3}) = \begin{cases} t_0 = 0 \\ t_1 = (\varphi - D_1 - D_2)T_s \\ t_2 = (\varphi - D_1)T_s \\ t_3 = \varphi T_s \\ t_4 = (\varphi + D_1)T_s \\ t_5 = (\varphi + D_1 + D_2)T_s \\ t_6 = T_{hs} \end{cases} \tag{4.7}$$

The instantaneous voltage across the inductance $v_L(t)$ is seen in (4.8). The piecewise function of the inductor voltage in all modes of operation is shown in (4.9), (4.10), (4.11).

$$v_L(t) = v_p(t) - \frac{v_b(t)}{n} \tag{4.8}$$

$$V_L(t)(\text{Mode 1}) = \begin{cases} V_P & (t_0 < t < t_1) \\ V_P & (t_1 < t < t_2) \\ V_P - \frac{V_B}{2n} & (t_2 < t < t_3) \\ V_P - \frac{V_B}{n} & (t_3 < t < t_4) \\ V_P - \frac{V_B}{n} & (t_4 < t < t_5) \\ V_P & (t_5 < t < T_{hs}) \end{cases} \tag{4.9}$$

$$V_L(t)(\text{Mode 3}) = \begin{cases} V_P + \frac{V_B}{2n} & (t_0 < t < t_1) \\ V_P & (t_1 < t < t_2) \\ V_P & (t_2 < t < t_3) \\ V_P - \frac{V_B}{2n} & (t_3 < t < t_4) \\ V_P - \frac{V_B}{n} & (t_4 < t < t_5) \\ V_P - \frac{V_B}{2n} & (t_5 < t < T_{hs}) \end{cases} \tag{4.10}$$

$$V_L(t)(\text{Mode 3}) = \begin{cases} V_P + \frac{V_B}{n} & (t_0 < t < t_1) \\ V_P + \frac{V_B}{2n} & (t_1 < t < t_2) \\ V_P & (t_2 < t < t_3) \\ V_P & (t_3 < t < t_4) \\ V_P - \frac{V_B}{2n} & (t_4 < t < t_5) \\ V_P - \frac{V_B}{n} & (t_5 < t < T_{hs}) \end{cases} \tag{4.11}$$

The instantaneous value of the current through an inductor can be expressed by solving (4.12), (4.13), (4.14).

$$\frac{V_L(t)}{L_k} = \frac{\mathrm{d}i_p(t)}{\mathrm{d}t} \tag{4.12}$$

$$\frac{V_L}{L_k} = \frac{i_p(t_{x+1}) - i_p(t_x)}{t_{x+1} - t_x} \tag{4.13}$$

$$i_p(t_{x+1}) = i_p(t_x) + \frac{V_L}{L_k}(t_{x+1} - t_x) \tag{4.14}$$

Under steady-state condition of the R3L-DAB converter, the average value of current through the inductor is zero, and is given by (4.15).

$$\Big\langle i_p \Big\rangle_{t=t_0}^{T_s} = 0 \tag{4.15}$$

Since the current through the inductor is half-wave symmetric, the condition shown in (4.16) is satisfied.

$$i_p(t_0) = -i_p(T_{hs}) \tag{4.16}$$

The value of the inductor currents at various instances ($t_1 - t_6$) can be calculated by solving the simultaneous equations at $x = 0..6$ in (4.14), using the equality shown in (4.16). The solution of instantaneous inductor currents in all modes of operation is seen in (4.17), (4.18), (4.19).

$$i_p(t_x)(\text{Mode 1}) = \begin{cases} i_p(t_0) = -\frac{T_s(nV_P - V_B + 4D_1V_B + 2D_1V_B)}{4nL_k} \\ i_p(t_1) = -\frac{T_s(nV_P - V_B + 4D_1V_B + 2D_2V_B - 4nV_P\varphi)}{L_k} \\ i_p(t_2) = -\frac{T_s(V_B - nV_P - 4D_1V_B - 2D_2V_B + 4nD_1V_P + 4nV_P\varphi)}{4nL_k} \\ i_p(t_3) = \frac{T_s(V_B - nV_P - 4D_1V_B - 4D_2V_B + 4nD_1V_P + 4nD_2V_P + 4nV_P\varphi)}{4nL_k} \\ i_p(t_4) = \frac{T_s(nV_P - V_B + 4D_1V_B + 4D_2V_B - 4nD_1V_P + 4nD_2V_P + 4nV_P\varphi)}{4nL_k} \\ i_p(t_5) = \frac{T_s(nV_P - V_B + 4D_1V_B + 2D_2V_B - 4nD_1V_P + 4nV_P\varphi)}{4nL_k} \\ i_p(T_{hs}) = \frac{T_s(nV_P - V_B + 4D_1V_B + 2D_1V_B)}{4nL_k} \end{cases} \tag{4.17}$$

$$i_p(t_x)(\text{Mode 2}) = \begin{cases} i_p(t_0) = -\frac{T_s(nV_P - V_B + 2V_B\varphi + 2D_1V_B + 2D_2V_B)}{4nL_k} \\ i_p(t_1) = -\frac{T_s(nV_P - V_B + 4D_1V_B + 2D_2V_B + 4nD_1V_P - 4nV_P\varphi)}{L_k} \\ i_p(t_2) = -\frac{T_s(nV_P - V_B + 4D_1V_B + 2D_2V_B - 4nV_P\varphi)}{4nL_k} \\ i_p(t_3) = \frac{T_s(V_B - nV_P - 4D_1V_B - 2D_2V_B + 4nD_1V_P - 4nV_P\varphi)}{4nL_k} \\ i_p(t_4) = \frac{T_s(V_B - nV_P - 4D_1V_B - 4D_2V_B + 4nD_1V_P + 4nD_2V_P + 4nV_P\varphi)}{4nL_k} \\ i_p(t_5) = \frac{T_s(nV_P - V_B + 4D_1V_B - 4D_2V_B - 4nD_1V_P - 4nD_2V_P + 4nV_P\varphi)}{4nL_k} \\ i_p(T_{hs}) = \frac{T_s(nV_P - V_B + 2V_B\varphi + 2D_1V_B + 2D_2V_B)}{4nL_k} \end{cases} \tag{4.18}$$

$$i_p(t_x)(\text{Mode 3}) = \begin{cases} i_p(t_0) = -\frac{T_s(nV_P - V_B + 4V_B\varphi)}{4nL_k} \\ i_p(t_1) = -\frac{T_s(V_P + \frac{V_B}{n})(D_1 + D_2 - \varphi)}{L_k} - \frac{T_s(nV_P - V_B + 4V_B\varphi)}{4nL_k} \\ i_p(t_2) = -\frac{T_s(nV_P - V_B + 4D_1V_B + 4nD_1V_P + 2D_2V_B - 4nV_P\varphi)}{4nL_k} \\ i_p(t_3) = -\frac{T_s(nV_P - V_B + 4D_1V_B + 2D_2V_B - 4nV_P\varphi)}{4nL_k} \\ i_p(t_4) = \frac{T_s(V_B - nV_P - 4D_1V_B - 2D_2V_B + 4nD_1V_P + 4nV_P\varphi)}{4nL_k} \\ i_p(t_5) = \frac{T_s(V_B - nV_P - 4D_1V_B - 4D_2V_B + 4nD_1V_P + 4nD_2V_P + 4nV_P\varphi)}{4nL_k} \\ i_p(T_{hs}) = \frac{T_s(nV_P - V_B + 4V_B\varphi)}{4nL_k} \end{cases} \tag{4.19}$$

The average power transferred across the high-frequency link of a R3L-DAB is given by 4.20. The closed-form solution of power transfer in all modes of operation can be determined by solving the piecewise definite integral of (4.20). The solution of the definite integral to obtain the power transfer expression in all modes of operation is shown in (4.21), (4.22), (4.23).

$$P_{out} = \frac{1}{T_{hs}} \int_{t_0}^{T_{hs}} v_p(t) i_p(t) \mathrm{d}t \tag{4.20}$$

$$P_{out,1} = \frac{V_P V_B}{n f_{sw} L_k} (\varphi - 4D_1\varphi - 2D_2\varphi) \tag{4.21}$$

$$P_{out,2} = \frac{V_P V_B}{n f_{sw} L_k} (\varphi - \varphi^2 - 2D_2\varphi - 2D_1\varphi - D_1^2) \tag{4.22}$$

$$P_{out,3} = \frac{V_P V_B}{n f_{sw} L_k}(\varphi - 2\varphi^2 - 2D_1^2 - 2D_1 D_2 - D_2^2) \tag{4.23}$$

The solution of the operating phase shifts in all modes of operation is shown in (4.24), (4.25), (4.26).

$$\varphi(\text{Mode 1}) = -\frac{n L_k P_{out}}{T_s V_P V_B (4D_1 - 2D_2 - 1)} \tag{4.24}$$

$$\varphi(\text{Mode 2}) = \frac{\pm\sqrt{\begin{array}{r} T_s V_P V_B (T_s V_P V_B - 4nL_k P_{out} + 4D_2^2 T_s V_P V_B \\ -4D_1 T_s V_P V_B - 4D_2 T_s V_P V_B + 8D_1 D_2 T_s V_P V_B) \end{array}}}{2T_s V_P V_B} + \frac{+T_s V_P V_B - 2D_1 T_s V_P V_B - 2D_2 T_s V_P V_B}{2T_s V_P V_B} \tag{4.25}$$

$$\varphi(\text{Mode 3}) = \frac{\pm\sqrt{\begin{array}{c} T_s V_P V_B (16 T_s V_P V_B D_1^2 + 16 T_s V_P V_B D_1 D_2 + \\ 8 T_s V_P V_B D_2^2 - T_s V_P V_B + 8nL_k P_{out}) \end{array}} + T_s V_P V_B}{2T_s V_P V_B} \tag{4.26}$$

The power transfer capability of the R3L-DAB converter reduces when $D_1 \neq 0$ or $D_2 \neq 0$. The mode of operation is determined based on the value of D_1, D_2 and φ. The value of these variables can be any combination meeting the criteria $(D_1, D_2, \varphi) \leq 0.25$. To observe the trend of operating modes, and the power transfer capability of the R3L-DAB, $(D_1 = D_2) \leq 0.125$. The variation in the output power capability of the R3L-DAB converter is shown in Fig. 4.13(a). The maxima of the output power is observed at $D_1 = D_2 = 0$ and $\varphi = 0.25$. The trajectory of the modes of operation is shown in Fig. 4.13(b).

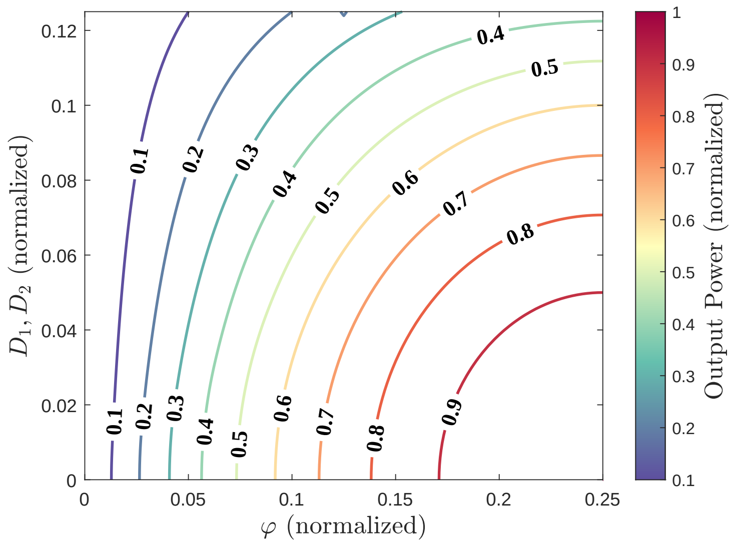

(A)

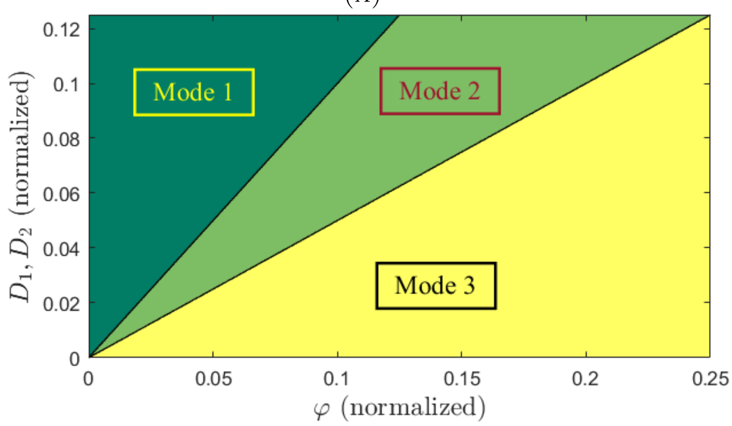

(B)

FIGURE 4.13: (a) Output power variation of the R3L-DAB as a function of D_1, D_2, φ. (b) Mode trajectory of the R3L-DAB as a function of D_1, D_2, φ.

The closed-form solution of the RMS current flowing through the leakage inductor $i_{p(rms)}$ can be obtained by solving the piecewise definite integral of (4.27).

$$i_{p(rms)} = \sqrt{\frac{1}{T_s}\int_{t_0}^{T_s} i_p^2(t)\mathrm{d}t} \tag{4.27}$$

The inductor RMS current in Mode 3 operation is seen in (4.28).

$$\begin{aligned} i_{p(rms)} = \Big\{ \big[& 192(D_1^2 D_2 V_B^2 - nD_1^2 V_P V_B \varphi - nD_1 D_2 V_P V_B \varphi) + 144 D_1 D_2^2 V_B^2 + 128 D_1^3 V_B^2 \\ & -96 n D_2^2 V_P V_B \varphi - 64 n V_P V_B \varphi^3 + 48(nD_1^2 V_P V_B - D_1^2 V_B^2 + nD_1 D_2 V_P V_B - D_1 D_2 V_B^2 \\ & +D_2^3 V_B^2 + n V_P V_B \varphi^2) + 24(nD_2^2 V_P V_B - D_2^2 V_B^2) + n^2 V_P^2 - 2nV_P V_B + V_B^2 \big] \\ & /(48^2 n^2 f_{sw}^2 L_k^2) \Big\}^{1/2} \end{aligned} \tag{4.28}$$

$$i_{S/M/D(rms)} = \sqrt{\frac{1}{T_s}\int_{t_{start}}^{t_{stop}} i_{S/M/D}^2(t)\mathrm{d}t} \tag{4.29}$$

The closed-form solution of the various RMS currents in the R3L-DAB converter are evaluated using the general form shown in (4.29), and the intervals shown in Table 4.4. Fig. 4.14 and Table 4.4 shows the comparison of the analytically modeled and simulated values of the RMS current stress in the R3L-DAB converter at the operating point where $D_1 = 0.028$, $D_2 = 0.028$, $\varphi = 0.12$, $P_{out} = 15$ kW, $V_{PFC} = 300$ V, $V_{batt} = 1.25$ kV. The mean value of the modeling error $\bar{\epsilon}$ = -0.26%, while the standard deviation of the modeling error $\sigma_\epsilon = 2.9\%$.

Table 4.3: Zero Voltage Switching (ZVS) criterion of the R3L-DAB in all modes of operation.

Switch	Mode 1	Mode 2	Mode 3
	Soft-Switching Criterion		
$S_{1,2,7,8}$	$i_p(t_0) < 0$		
$S_{3,4,5,6}$	$i_p(T_{hs}) > 0$		
$M_{1,4}$	$i_p(t_3) > 0$	$i_p(t_4) > 0$	$i_p(t_5) > 0$
M_2	$i_p(t_2) > 0$	$i_p(t_3) > 0$	$i_p(t_4) > 0$
M_3	$i_p(t_8) < 0$	$i_p(t_9) < 0$	$i_p(t_{10}) < 0$
$M_{5,8}$	$i_p(t_5) < 0$	$i_p(t_7) < 0$	$i_p(t_8) < 0$
M_6	$i_p(t_4) < 0$	$i_p(t_5) < 0$	$i_p(t_7) < 0$
M_7	$i_p(t_{10}) > 0$	$i_p(t_{11}) > 0$	$i_p(t_1) > 0$

Table 4.4: Comparison of the analytically modeled and simulated RMS currents of the R3L-DAB converter in operating mode 3.

Section	t_{start}	t_{stop}	Analytical i_{rms}	Simulation i_{rms}	Error ϵ (%)
L_k	t_0	T_s	55.41	55.24	+0.31
$S_{1..8}$	t_0	T_{hs}	39.17	36.79	+6.47
M_1, M_4	t_5	t_{10}	12.60	13.14	-4.07
M_2, M_3	t_5	t_{11}	13.92	13.99	-0.50
D_4, D_5	t_{10}	t_{11}	4.63	4.82	+0.22
M_5, M_8	t_0 & t_8	t_1 & t_{12}	13.36	13.67	-2.27
M_6, M_7	t_0 & t_7	t_2 & t_{12}	13.96	13.99	-0.21
D_6, D_7	t_7	t_8	2.90	2.96	-2.03

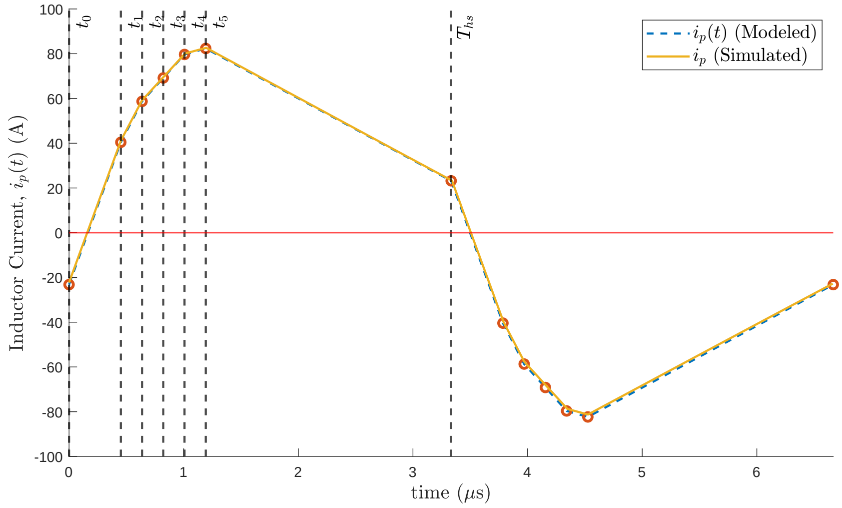

(A)

FIGURE 4.14: Comparison of analytically modeled and simulated steady-state inductor current $i_p(t)$, ($D_1 = 0.028$, $D_2 = 0.028$, $\varphi = 0.12$, $P_{out} = 15$ kW, $V_{PFC} = 300$ V, $V_{batt} = 1.25$ kV.

4.4 Soft-Switching Criterion

The dual active bridge converter, due to the nature of its power decoupling impedance does not contain a resonant tank, and hence deprives the ability to naturally perform zero current switching (ZCS) without using advanced modulation techniques. However, ZVS can be achieved by having a lagging current prior to the turn-on instant of the switch under consideration. The action of forward-biasing the body-diode of a MOSFET prior to turn-on enables a zero voltage turn-on. The ZVS criterion of all the switches in the R3L-DAB is shown in Table. 4.5. The mentioned inequalities are required to be satisfied based on the mode of operation as the first step for achieving ZVS.

The action of ZVS, caused by the forward-biased body diode of the MOSFET is due to the resonance between the leakage inductance, and the MOSFET output capacitance (C_{oss}). Depending upon the state of the bridge, and whether

Table 4.5: Zero Voltage Switching (ZVS) criterion of the R3L-DAB in all modes of operation.

Switch	**Mode 1**	**Mode 2**	**Mode 3**
	Soft-Switching Criterion		
$S_{1,2,7,8}$	$i_p(t_0) < 0$		
$S_{3,4,5,6}$	$i_p(T_{hs}) > 0$		
$M_{1,4}$	$i_p(t_3) > 0$	$i_p(t_4) > 0$	$i_p(t_5) > 0$
M_2	$i_p(t_2) > 0$	$i_p(t_3) > 0$	$i_p(t_4) > 0$
M_3	$i_p(t_8) < 0$	$i_p(t_9) < 0$	$i_p(t_{10}) < 0$
$M_{5,8}$	$i_p(t_5) < 0$	$i_p(t_7) < 0$	$i_p(t_8) < 0$
M_6	$i_p(t_4) < 0$	$i_p(t_5) < 0$	$i_p(t_7) < 0$
M_7	$i_p(t_{10}) > 0$	$i_p(t_{11}) > 0$	$i_p(t_1) > 0$

inner-phase shifts are present based on the modulation scheme, the equivalent capacitance changes [125].

$$0.5L_kI_{on}^2 > 0.5C_{eq}V_{eq}^2 \tag{4.30}$$

The energy inequality seen in (4.30) should be satisfied as the second layer of check, to ensure that there is sufficient energy in the inductance to cause ZVS, else it would result in a partial ZVS condition.

Chapter 5

Design of a Reconfigurable Three-Level Dual Active Bridge Converter for 1.25 kV On-Board Charging Applications

5.1 DC-DC Converter Requirements for a 1.25 kV On-Board Charger

As established in Chapter 3, the unique 3-Φ voltages in North America are 208/120Y, 220/127Y, 480/277Y, and 600/347Y. The SAE J3068 standard has variation in the amperage of the current carrying contacts, that determine the power delivery limit of a charging connector. The standard contacts are rated at 63 A, while advanced contacts (AC_6) are rated at 100 A, 120 A, 160 A. Table 5.1 shows the values of the charging power vector $\vec{P_{charge}}$ for varying values of grid phase voltage $\vec{V_{ph}}$, charging contact current $\vec{I_{ph}}$, and displacement power factor $\cos\phi = 1$, as seen

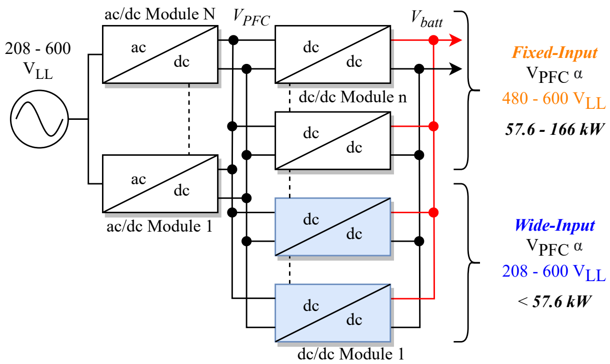

FIGURE 5.1: Multi-module IPOP two-stage on-board charger structure.

TABLE 5.1: Charging Power (kW) as a function of varying AC input voltage and SAE J3068 contacts

Contact Current			63 A	100 A*	120 A*	160 A*
V_{ph} (V)	V_{LL} (V)	$V_{PFC(min)}$ (V)	Power (kVA)			
120	208	294	22.7	36	43.2	57.6
127	220	311	24	38.1	45.7	61
277	480	679	52.4	83.1	99.7	133
347	602	851	65.6	104.1	124.9	166.6

in (5.1).

$$P_{\vec{charge}}(\mathrm{kW}) = \eta 3 \vec{V_{ph}} \vec{I_{ph}} \cos\phi \tag{5.1}$$

A conventional PFC converter stage can be classified as buck, boost, or buck-boost types. Since the battery voltage is higher than the AC input voltage, the an example of boost PFC, such as the six-switch PFC rectifier or the Vienna rectifier is assumed. The minimum DC link voltage of the PFC $V_{PFC(min)}$ below which regulation is not possible is given by (5.2).

$$V_{PFC(min)} = \sqrt{6} V_{ph} \tag{5.2}$$

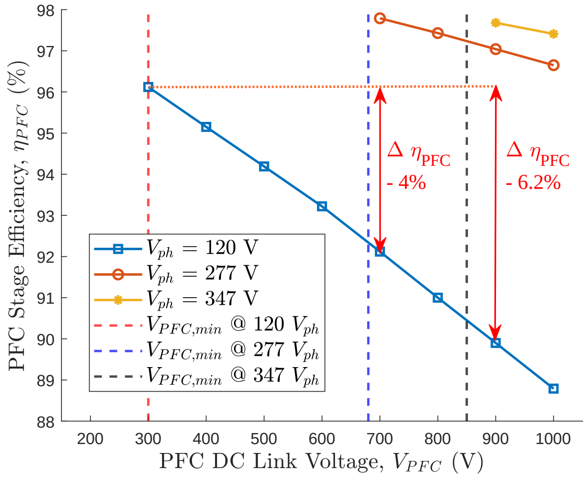

FIGURE 5.2: Simulated efficiency of a 3-Φ boost PFC converter operating at 15 kW, with varying V_{PFC} and V_{ph}.

A 3-Φ PFC converter is preferred to be operated in the continuous conduction mode (CCM) due to high power-handling requirements [66]. This causes hard-switching in the PFC converter, resulting in higher switching losses, and thus, a lower efficiency [126]. In a conventional two-level boost PFC converter, the switch's voltage stress is the DC link voltage, while, the current stress is a sinusoidal input current. As the PFC's DC link voltage is raised beyond $V_{PFC(min)}$, the converter's efficiency diminishes based on the trajectory of rise in switching energy. That being said, the lowest losses will be experienced on the PFC converter when $V_{PFC} = V_{PFC(min)}$. The on-board charger must operate from 208/120Y to 600/347Y to fully cater across North America's varying grid voltage, referring to a voltage swing between $300 < V_{PFC} < 850$ V, to enable minimal reduction in efficiency of the PFC converter. Fig. 5.2 shows the simulated efficiency map of a 3-Φ boost PFC converter in the PLECS environment, operating at a load of 15 kW, $f_{sw} = 100$ kHz, and utilizing Wolfspeed's C3M0016120D (1.2 kV/ 16 mΩ) SiC MOSFETs. The simulation confirms that the efficiency drop is detrimental as the DC link voltage of the PFC stage increases, especially at lower input phase voltages.

Table 5.2: Electrical design targets of the R3L-DAB converter

Design Variable	**Description**	**Specification**
$V_{PFC}(V_P)$	PFC DC link range	300 - 850 V
$V_{batt}(V_B)$	Battery voltage range	890 - 1250 V
P_{out}	Power rating	15 kW

A Li-ion NMC cell varies from 3 - 4.2 V representing 0 - 100% state of charge. A 1.25 kV battery pack would require serialization of 296 cells, resulting in a total battery voltage swing from 890 - 1250 V. The maximum power defined in SAE J3068 is 166 kW, and the R3L-DAB converter is expected to operate in a multi-module IPOP architecture, as shown in Fig. 5.1. The power level of the R3L-DAB is approximately $1/10^{\text{th}}$ of the maximum power, and is set to 15 kW. The design requirements are summarized in Table 5.2.

5.2 R3L-DAB Power Loss Model

The efficiency of the R3L-DAB based on its operating point can be estimated analytically or in simulation. In the context of this thesis, an analytical model has been constructed. This section describes the set of equations used to estimate the losses of the R3L-DAB at a particular operating point, that is further used for the optimization of efficiency and power density.

The power loss equations of various components in the R3L-DAB are defined in Table 5.3. The symbols encountered for the first time are as follows; ZVS is a boolean, and is 0 when ZVS the above mentioned conditions for the operating point are true, and is 1 when ZVS condition is false. E_{on} and E_{off} are 2-dimension look up tables, and are defined as a function of switched voltage and current. t_{dead} is the converter dead time between complementary switches. V_{SD} is the forward voltage of the MOSFET's body-diode. V_F is the forward voltage of the clamp

Table 5.3: Power loss equations of the R3L-DAB

Component	Power Loss	Loss Symbol	Loss Equation (W)
S_x/M_y	MOSFET Conduction	$P_{cond(M)}$	$i_{rms}^2 R_{ds(on)}$
	MOSFET Turn-on	P_{on}	ZVS.$f_{sw}E_{on}(V_{ds}, I_{on})$
$x \in 1..9$	MOSFET Turn-off	P_{off}	$f_{sw}E_{off}(V_{ds}, I_{off})$
$y \in 1..8$	Diode Conduction	$P_{cond(D)}$	$f_{sw}t_{dead}V_{SD}I_{on}$
D_x	Diode Conduction	P_d	$V_F I_{D(av)}$
$x \in 1..7$	Diode Reverse Recovery	P_{rr}	Neglected
Transformer	Winding	P_{cu}	$i_{p(rms)}^2 R_p + (i_{p(rms)}/n)^2 R_s$
	Core Loss	P_{core}	$k_{fe} f_{sw}^{\alpha} \Delta B^{\beta} V_e$
Passive	Inductor	P_L	$i_{p(rms)}^2 ESR_L$
	Capacitor	P_C	$i_{c(rms)}^2 ESR_C$

diodes, $I_{D(av)}$ is the average forward current through the clamp diode. R_p and R_s are the AC resistances of the transformer winding. k_{fe}, α, and β are the Steinmetz coefficients of the core, V_e is the total core volume. $i_{c(rms)}$ is the capacitor RMS current. ESR_C and ESR_L are the equivalent series resistances of the capacitor and inductor.

$$\begin{aligned} P_{total}(\text{F.B}) = {} & 8(P_{cond(M)} + P_{on} + P_{off} + P_{cond(D)})\big|_{M_1}^{M_8} + 4(P_d + P_{rr})\big|_{D_1}^{D_3} \\ & +8(P_{cond(M)} + P_{on} + P_{off} + P_{cond(D)})\big|_{S_1}^{S_8} + 4(P_d + P_{rr})\big|_{D_4}^{D_7} \\ & +P_{cu} + P_{core} + P_L + P_C \end{aligned} \tag{5.3}$$

$$\begin{aligned} P_{total}(\text{H.B}) = {} & 4(P_{cond(M)} + P_{on} + P_{off} + P_{cond(D)})\big|_{M_1}^{M_4} + 2(P_d + P_{rr})\big|_{D_1}^{D_2} \\ & +8(P_{cond(M)} + P_{on} + P_{off} + P_{cond(D)})\big|_{S_1}^{S_8} + 4(P_d + P_{rr})\big|_{D_4}^{D_7} \\ & +P_{cu} + P_{core} + P_L + P_C + \underbrace{2P_{cond(M)}\big|_{M_7}^{M_9}}_{\text{Reconfiguration Loss}} \end{aligned} \tag{5.4}$$

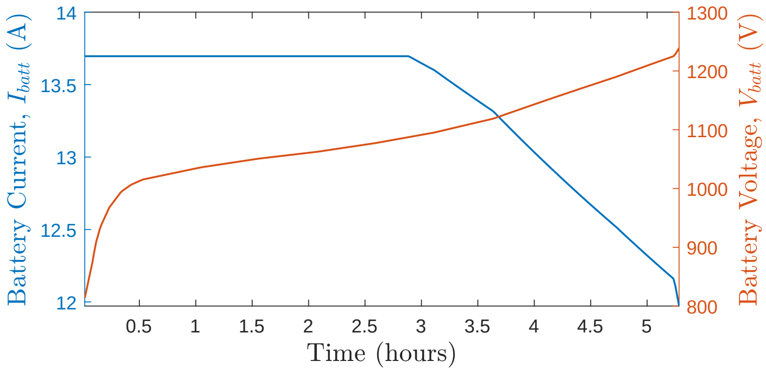

FIGURE 5.3: Charging Profile of a 1.25 kV Battery.

The total power loss in the R3L-DAB's full-bridge and half-bridge operation are given by (5.3) and (5.4). The efficiency of the R3L-DAB is calculated using (5.5).

$$\eta(V_P, V_B, P_{out}) = \frac{P_{out} - P_{loss(total)}}{P_{out}} \times 100\% \tag{5.5}$$

5.3 Efficiency and Power Density Optimization

The priority operating regions of a R3L-DAB operating in the Grid-to-Vehicle (G2V) operating modes can be determined based on the battery charging profile. The assumed charging profile for a 1.25 kV/ 500 Ah battery pack is shown in Fig. 5.3. The operating point vector $\vec{OP} = f(V_{PFC}, V_{batt}, P_{batt})$ and is discretized based on finite time intervals in the charging profile.

Selection of the turns ratio n, switching frequency f_{sw}, and leakage inductance L_k affects the average efficiency of the R3L-DAB converter. The mean RMS current $\bar{i}_{p(rms)}$ is calculated using (4.28) for variations in n and V_{PFC}. Lower RMS current is an indicator of the highest utilization of the high-frequency link, and minimum deviation in the conversion ratio of the converter away from its nominal value. The mean value of the RMS current for all variations of the PFC input

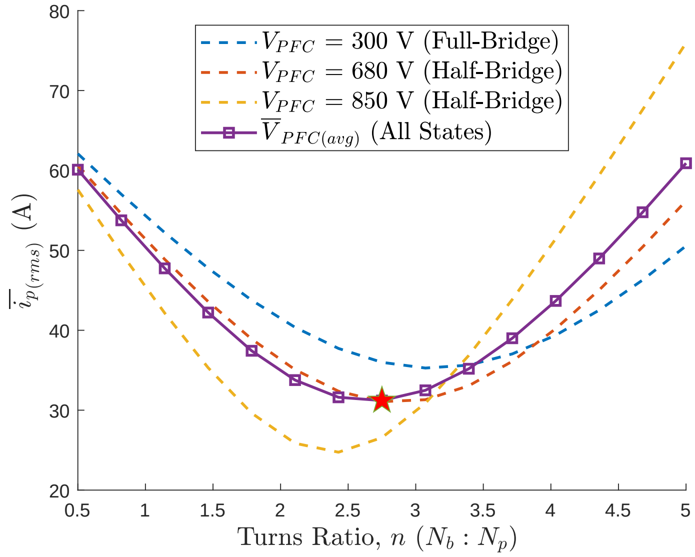

FIGURE 5.4: Average primary RMS current as a function of turns ratio.

voltage is consolidated, and its minima is observed at $n = 2.8$.

Fig. 5.5 shows the algorithm used for selection of the switching frequency and leakage inductance. The turns ratio of the converter is fixed as a result of the previously mentioned parameter sweep.

For brevity, and to limit the number of variables of the optimization problems, D_1 and D_2 are set to 0, thus defining the scope of optimization to a two-level modulation scheme on the secondary bridge. The maximum leakage inductance $L_{k(max)}$ evaluated at a certain switching frequency f_{sw} is given by (5.6).

$$L_{k(max)}|_{f_{sw}} = \frac{V_{P(min)}V_{B(min)}}{nf_{sw}P_{out(max)}}(\varphi_{max} - 2\varphi_{max}^2) \tag{5.6}$$

The key components apart from the converter parameters are sized using initial parameter sweeps regarding the switched current, RMS current while maintaining

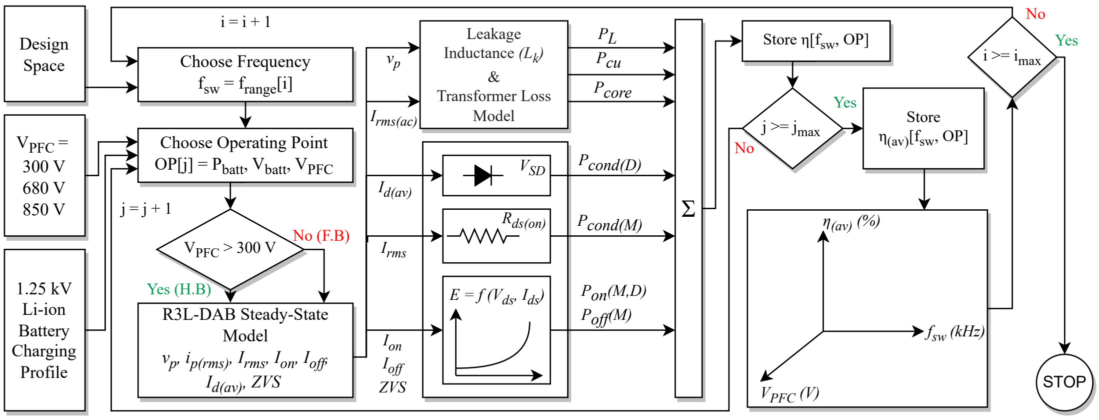

FIGURE 5.5: Weighted efficiency algorithm.

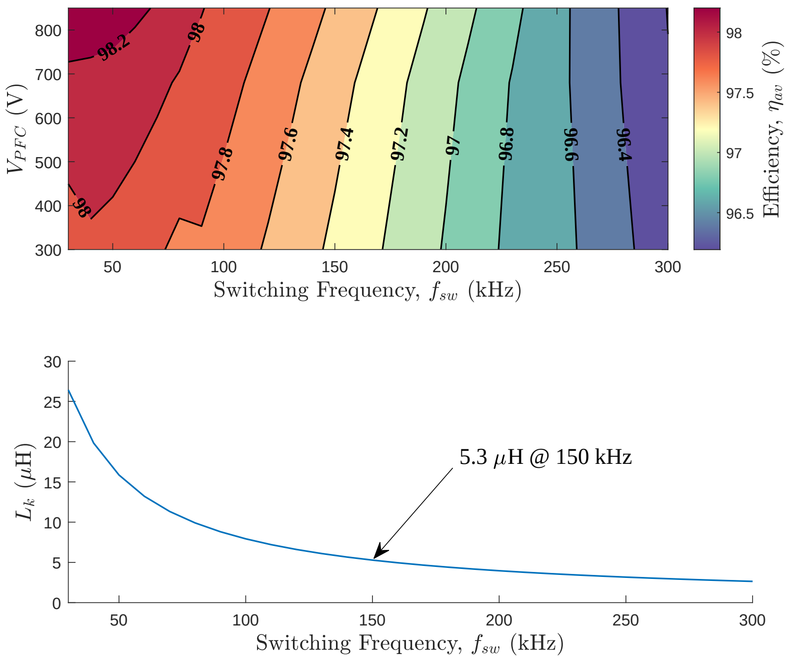

FIGURE 5.6: Results of the weighted efficiency algorithm.

the same high-frequency link impedance scaled to the frequency. Based on this component selection, the switching energy tables are defined. The transformer core size and material is also defined based on the required power handling requirement of the R3L-DAB converter.

As shown in Fig. 5.5, the algorithm generates a three-dimensional space of the average efficiency η_{av}, as a function of the input voltage V_{PFC} and the switching frequency f_{sw}. The explanation of the algorithm is as follows; The switching frequency sweep is defined between $f_{sw(min)} = 25$ kHz to $f_{sw(max)} = 300$ kHz. At first, the operating point $\vec{OP}$ is selected based on the discrete point on the charging profile and the selected V_{PFC}. The operating point is passed through the R3L-DAB's steady-state model to compute the steady state currents. The steady state current equations are used to evaluate the various losses discussed in the previous section, and are used to evaluate the efficiency at an operating point. The average efficiency of the R3L-DAB at a single input voltage, for varying V_{batt} and P_{out} is computed, while consequently calculating the efficiency for all values of V_{PFC} and f_{sw} to develop the trajectory map of the efficiency.

Fig. 5.6 shows the efficiency map of the R3L-DAB as a function of variation in the switching frequency and the PFC DC link voltage. It can be observed that the mean efficiency of this dataset is at 97%, and the increase in switching frequency of the R3L-DAB is not very detrimental to the average efficiency. However, the variation in required leakage inductance is minimal. To reduce the challenges in management of the system's leakage inductance, the leakage inductance is chosen at the inflection point of $\mathrm{d}L_k/\mathrm{d}f_{sw} < 0.5\mu H/10\mathrm{kHz}$, while being able to fit the external leakage inductance into the power electronics package.

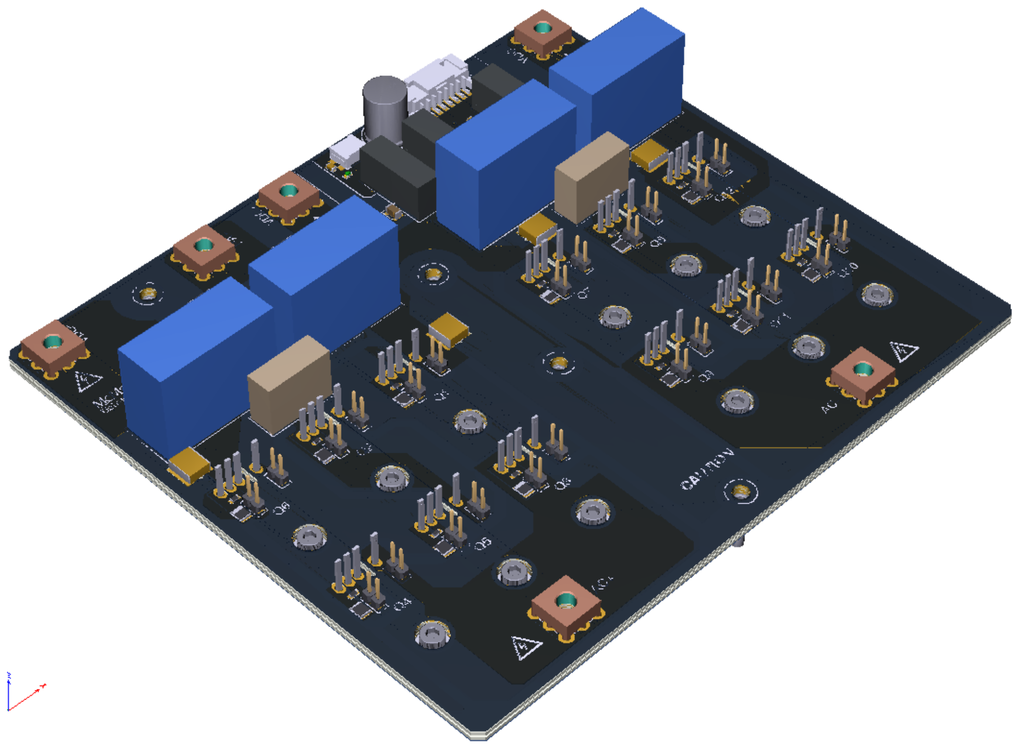

FIGURE 5.7: Isometric view of the Power Board.

5.4 DC-DC Converter Design

5.4.1 High-Voltage Power Board

The power board of the R3L-DAB converter is used to construct both the primary and secondary bridges. In order to provide design modularity and have flexibility for topological variations, an ANPC full-bridge converter is constructed. This ANPC full-bridge can be used to construct either a NPC converter or an RNPC converter. The isometric view of the Power Board is seen in Fig. 5.7.

The power board is constructed such as it can be mounted on a plate with liquid-cooling. All the MOSFETs are through-hole SiC devices in the TO-247-4 packages, to avail the provision of a Kelvin-source connection and reduced switching energies.

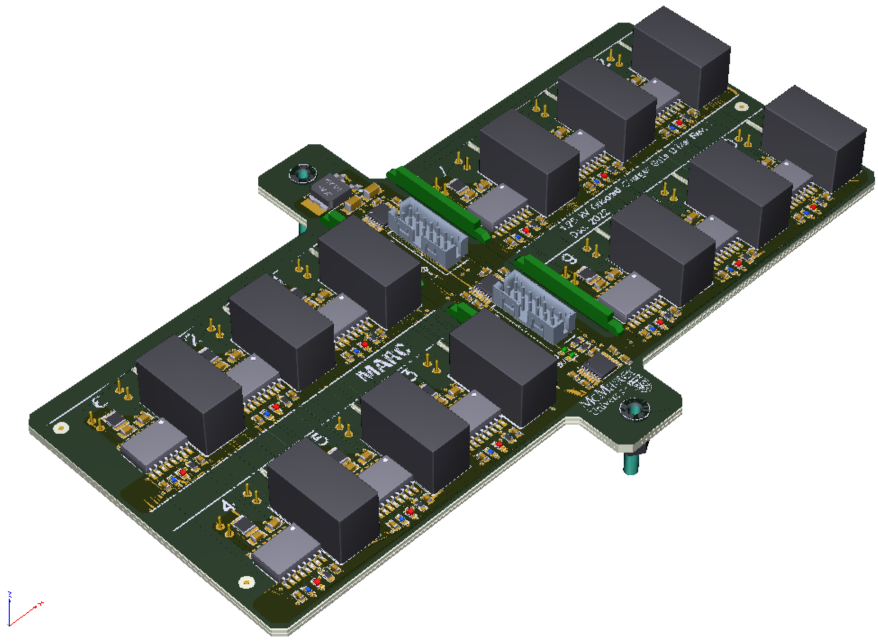

FIGURE 5.8: Isometric view of the Gate Driver Board.

The primary side MOSFETs are UJ4SC075009K4S (9 mΩ / 750 V) from Qorvo, while the secondary side MOSFETs are G3R20MT12K (20 mΩ / 1.2 kV) from GeneSiC. The clamp diodes are MSC030SDA070K (Microchip) and GD20MPS12A (GeneSiC) on the primary and secondary sides, respectively.

A companion gate driver board is designed to cascade on top of the power board, while accessing its gate, drain, kelvin source pins. The gate driver is equipped to control the entire ANPC converter. The choice of populating or not populating the gate driver and its companion circuit is based on the stage of use (NPC or RNPC stage). The gate driver power supply is MGJ2D151505SC (muRata), while the gate driver is 1ED3322MC12NXUMA1 (Infineon). The current source/sink capability of the gate driver is +6 A/ -8.5 A. The gate resistances of either bridges are curated based on the recommendations of the MOSFET manufacturers. The schematic of a single gate driver channel is shown in Fig. 5.9. Further details of the power converter realization are shown in Table 6.1.

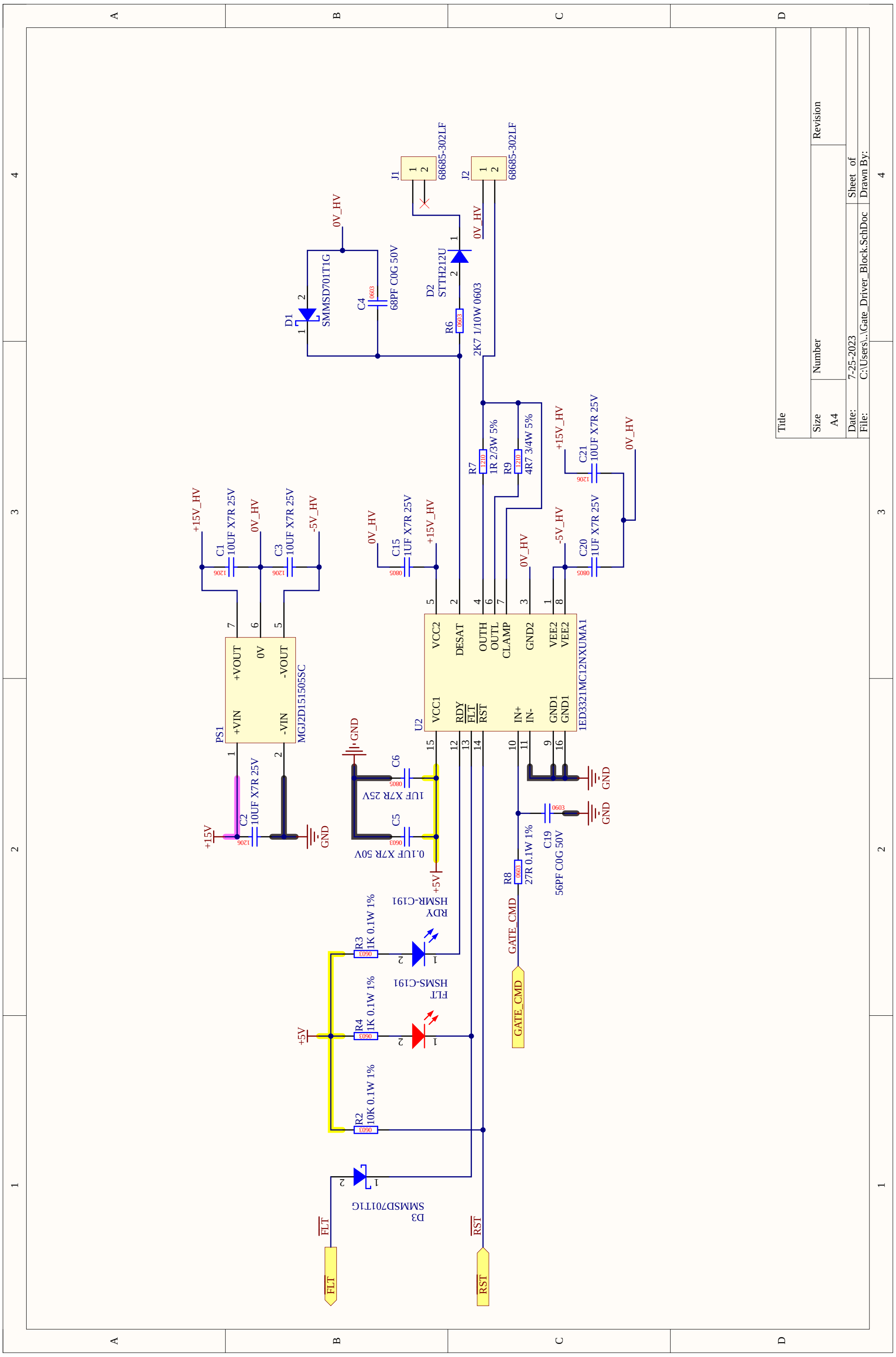

FIGURE 5.9: Gate driver channel schematic.

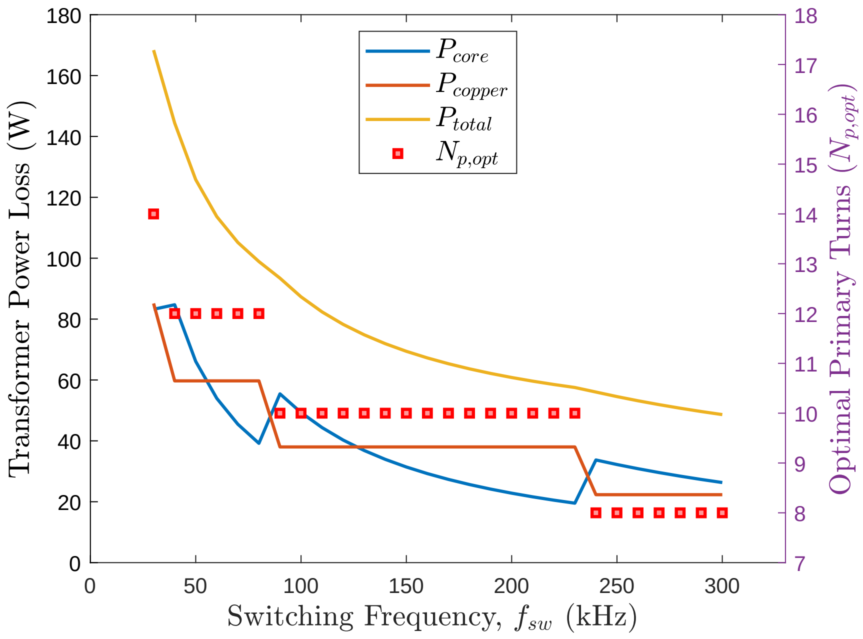

FIGURE 5.10: Optimal primary turns $N_{p,opt}$ over frequency variations.

5.4.2 Planar Transformer

The high-frequency link between the primary and secondary bridges is isolated using the transformer, with a secondary to primary turns ratio n. The turns ratio has been selected as $n = 2.8$. The Primary Winding Turns (N_p) and its optimal value $N_{p,opt}$ can be evaluated at every frequency using (5.7). The symbols in equation are defined as Copper resistivity (ρ), Mean Length per Turn (MLT), Number of layers per winding (n_l), Copper thickness (t_{cu}), Primary winding PCB trace width (w_{pri}), Secondary winding PCB trace width (w_{sec}), Core cross section area (A_c), Core effective volume (V_e), Secondary Winding Turns (N_s).

Fig. 5.10 shows the variation of the optimal primary turns as a function of operating frequency. The core parameters are based on the B66297G0000X197 core from TDK. The number of layers n_l are 10. The primary and secondary windings are separated by an FR-4 insulator. $N_{p,opt} = 10$, $N_s = 28$ are the chosen design specifications based on $f_{sw} = 150$ kHz. The specifications of the transformer are mentioned in Table. 6.1. The transformer measurements on the Keysight E4990A impedance analyzer for the magnetizing inductance L_{mag} and leakage inductance $L_{k,xfmr}$ are shown in Fig. 5.11.

$$N_{p,opt}(f_{sw}) = \min \Bigg(\underbrace{\mathrm{ceil}(\frac{N_p}{n})^3 \frac{i^2_{p(rms)}}{n_l} \left(\frac{\rho \mathrm{MLT}}{t_{cu} w_{sec}}\right)}_{\text{Secondary Copper Loss}}$$

$$\underbrace{N_p \frac{i^2_{p(rms)}}{n_l} \left(\frac{\rho \mathrm{MLT}}{t_{cu} w_{pri}}\right)}_{\text{Primary Copper Loss}} + \underbrace{k_{fe} f^{\alpha}_{sw} \left(\frac{V_{batt(max)}}{\mathrm{ceil}(nN_p) f_{sw} A_c}\right)^{\beta} V_e}_{\text{Core Loss}} \Bigg) \tag{5.7}$$

$$f_{sw} \in \{f_{sw(min)} \ldots f_{sw(max)}\}$$

$$N_p \in \{N_{p(min)} \ldots N_{p(max)}\}$$

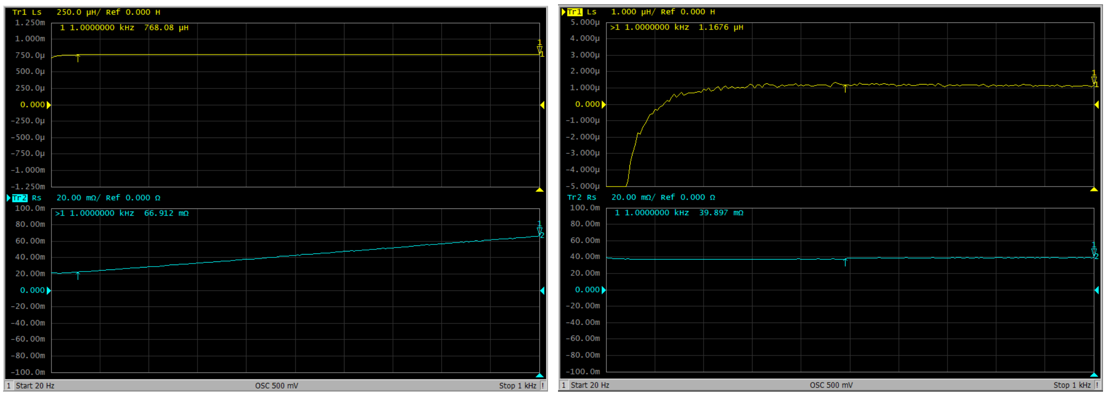

FIGURE 5.11: Transformer measurements (a) Magnetizing Inductance L_{mag} (b) Leakage inductance $L_{k,xfmr}$.

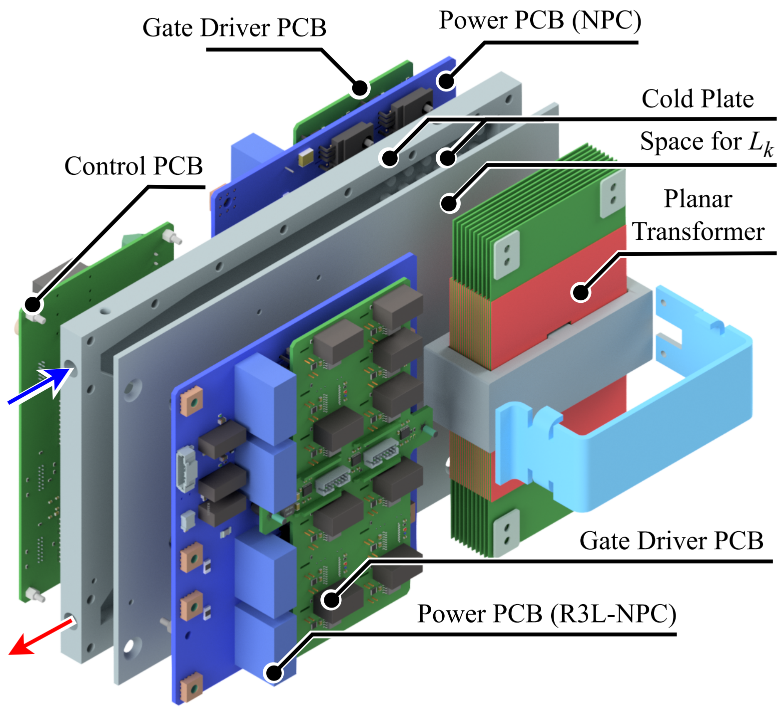

FIGURE 5.12: Exploded view of the construction of the R3L-DAB converter.

5.4.3 Power Electronics Packaging

The R3L-DAB converter is packaged around a cold-plate measuring 176 × 274 × 14 mm, that is designed for a flow-rate of 8 LPM, and a coolant of 50% deionized water and ethylene glycol. The power board of the RNPC converter, the external leakage inductance, the planar transformer, the power board of the NPC converter, and the control board are connected to the cold-plate, making the total dimensions of the envelope to 176 × 274 × 96 mm. The power density of the R3L-DAB converter prototype is 3.25 kW/L or 53.25 W/in^3. Fig 5.12 shows the exploded view of the R3L-DAB converter, while Fig. 5.13 shows the hardware demonstrator prototype of the R3L-DAB converter.

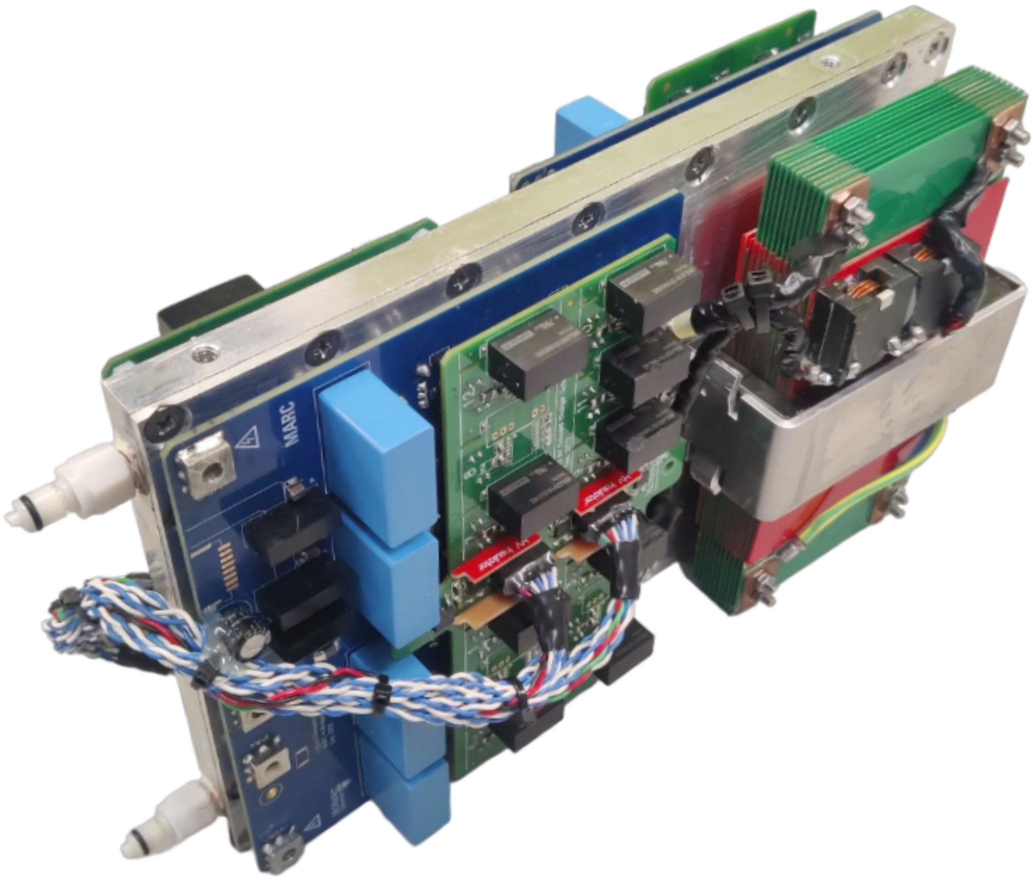

FIGURE 5.13: Hardware demonstrator of the 15 kW R3L-DAB converter.

Chapter 6

Experimental Results and Verification

This section discusses the experimental results of the R3L-DAB converter, and focuses primarily on its efficiency evaluation. Table 6.1 consolidates the information regarding the realization of the R3L-DAB converter, and thus, the Device Under Test (DUT). The Zimmer LMG671 Power Analyzer is used to measure the electrical efficiency of the R3L-DAB. The primary side current sensor is the LEM IT 700-S ULTRASTAB. The secondary side current sensor is the LEM IT 60-S ULTRASTAB.

The efficiency measurements are performed for the following variation of the PFC voltage; V_{PFC} = 300 V, 400 V, 680 V, 850 V. The battery side voltage variations are done based on the minimum, nominal and maximum voltages of the battery pack; V_{batt} = 890 V, 1095 V, 1250 V. The minimum achievable load resistance is 120 Ω, and is the reason power transfer tests are capped to 6.6 kW when V_{batt} = 890 V, and is 9.9 kW when V_{batt} = 1095 V. The power variations are performed by paralleling 1.2 kΩ resistors.

TABLE 6.1: Realization details of the R3L-DAB converter

	Parameter	**Specification**
Key Specs.	V_{PFC}	300 - 850 V
	V_{batt}	890 - 1250 V
	$P_{out(max)}$	15 kW
	f_{sw}	150 kHz
	L_k	5.3 μH
	η_{peak}	97.32 %
Primary (RNPC)	SiC MOSET	UJ4SC075009K4S (Qorvo)
	$R_{ds(on)}/V_{ds(max)}$	9 mΩ/ 750 V
	$V_{gs(on)}/V_{gs(off)}$	+15 V/ -5 V
	$R_{g(on)/R_{g(off)}}$	3.3 Ω/ 5.6 Ω
	R_s/C_s	5 Ω/ 560 pF
	SiC Diode	MSC030SDA070K (Microchip)
	SiC Diode's V_F/I_D	700 V/ 30 A
Secondary (NPC)	SiC MOSET	G3R20MT12K (GeneSiC)
	$R_{ds(on)}/V_{ds(max)}$	20 mΩ/ 1200 V
	$V_{gs(on)}/V_{gs(off)}$	+15 V/ -5 V
	$R_{g(on)/R_{g(off)}}$	12 Ω/ 2 Ω
	SiC Diode	GD20MPS12A (GeneSiC)
	SiC Diode's V_F/I_D	1200 V/ 20 A
Power Board Components	DC link capacitor	5 μF/ 800 V
		B32774D8505K000 (EPCOS)
	Bypass capacitor	0.1 μF/ 1500 V
		C2225C104KFRAC (KEMET)
	Gate driver	1ED3322MC12NXUMA1 (Infineon)
	Iso. power supply	MGJ2D151505SC (muRata)
Transformer	Turns ratio (n)	28:10 (2.8)
	Core & material	ELP 102/20/38 & N97
		B66297G0000X197 (TDK)
	L_{mag}	0.77 mH at 1 kHz
	$L_{k,xfmr}$	1.17 μH at 1 kHz
	Copper thickness	6 oz/ft^2 (210 μm)
	PCB prepreg	FR-4 (0.35 mm)
	n_l per winding	10
	Insulator thickness	0.35 mm
	Insulator breakdown	4130 V_{peak}
Cold Plate	Dimensions	176 $\times$ 274 $\times$ 14 mm
	Flow rate	8 LPM
	Coolant	50% DI water/ ethylene glycol
Mech. Dimensions	Dimensions	176 $\times$ 274 $\times$ 96 mm
	Power density	3.25 kW/L or 53.25 W/in^3

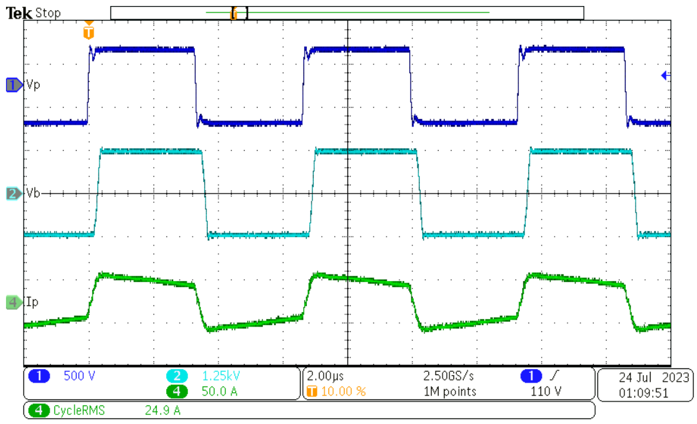

(A)

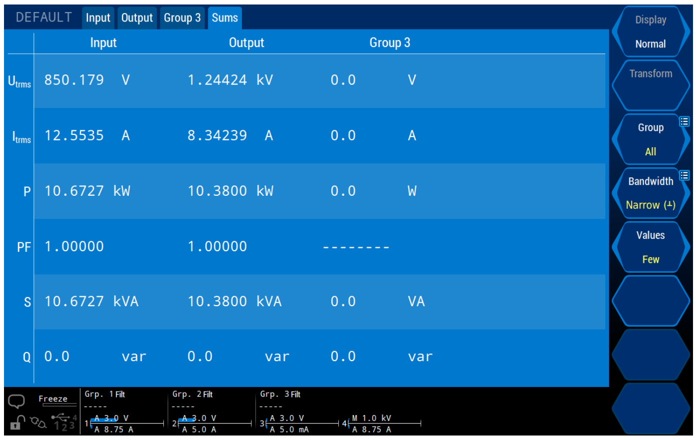

(B)

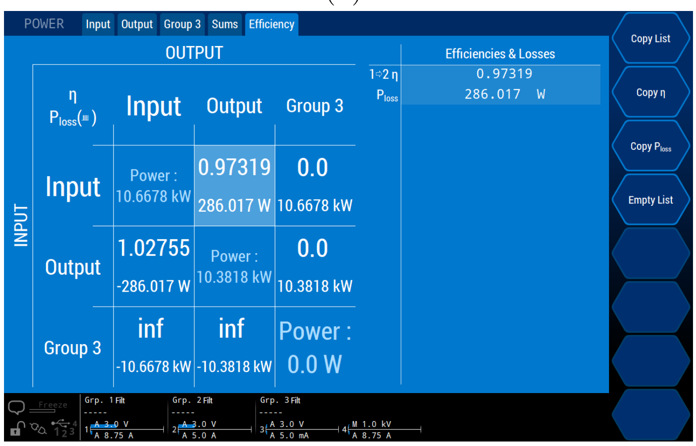

(C)

FIGURE 6.1: Peak efficiency operating point of the R3L-DAB converter (V_{PFC} = 850 V (H.B), V_{batt} = 1.25 kV, P_{out} = 10.38 kW) (a) Oscilloscope Capture (b) Power Analyzer Voltage Measurement (c) Power Analyzer Efficiency Measurement

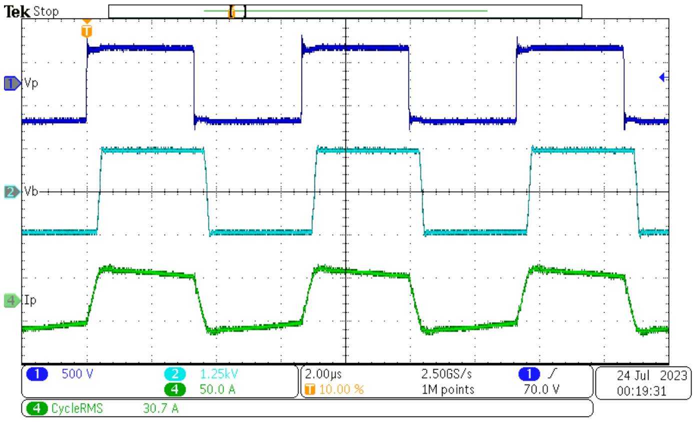

(A)

(B)

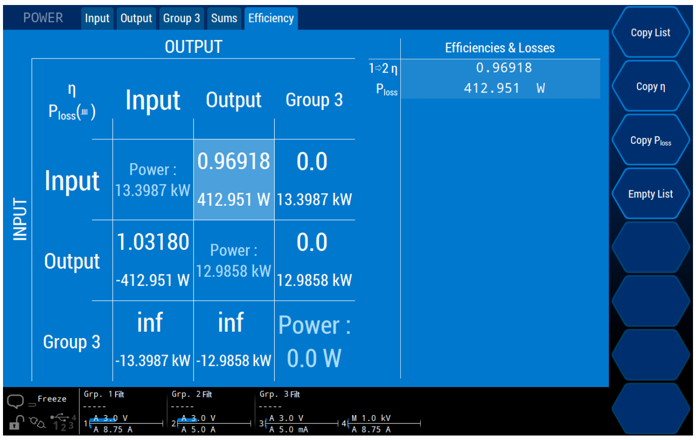

(C)

FIGURE 6.2: V_{PFC} = 850 V (H.B), V_{batt} = 1.25 kV, P_{out} = 12.98 kW (a) Oscilloscope Capture (b) Power Analyzer Voltage Measurement (c) Power Analyzer Efficiency Measurement

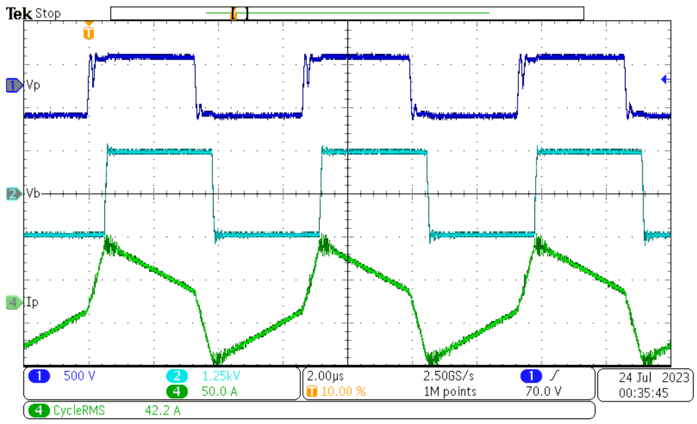

(A)

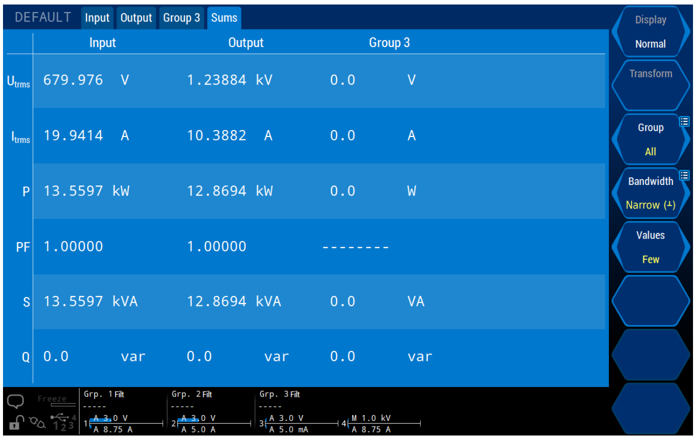

(B)

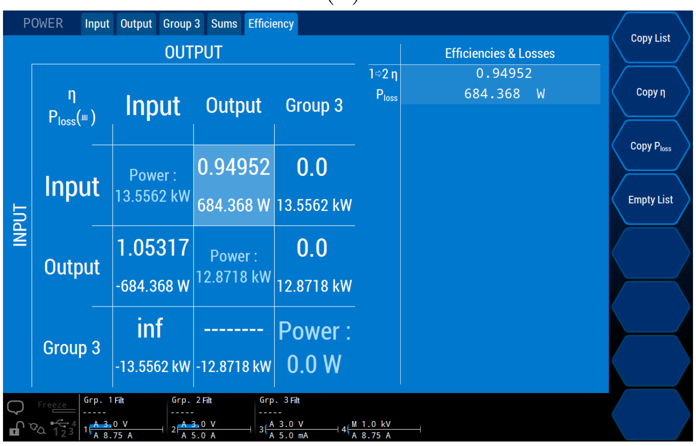

(C)

FIGURE 6.3: V_{PFC} = 680 V (H.B), V_{batt} = 1.25 kV, P_{out} = 12.86 kW (a) Oscilloscope Capture (b) Power Analyzer Voltage Measurement (c) Power Analyzer Efficiency Measurement

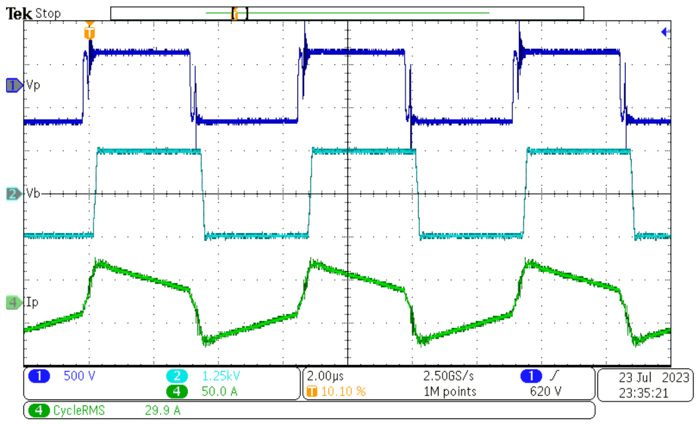

(A)

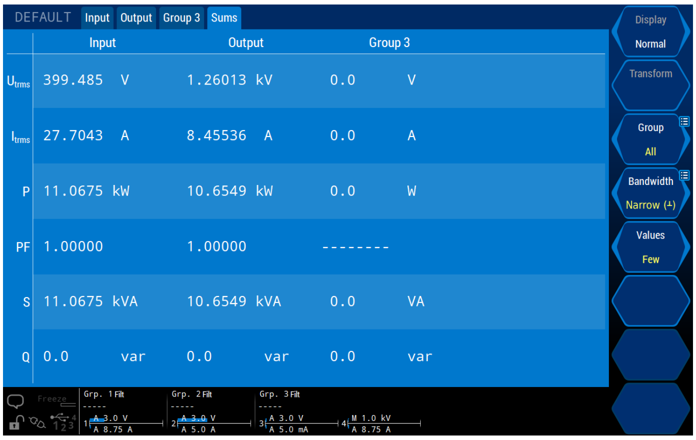

(B)

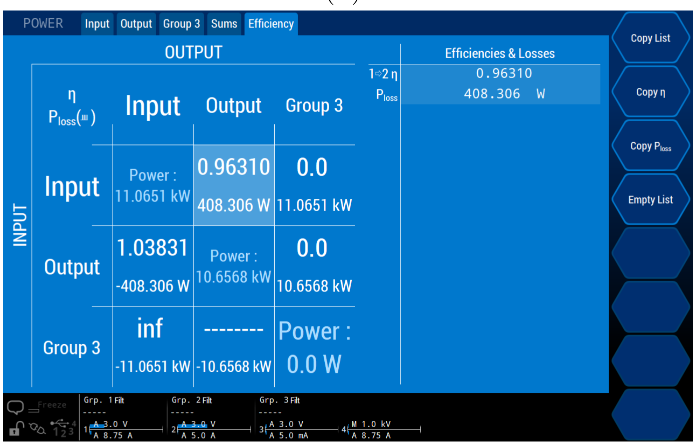

(C)

FIGURE 6.4: $V_{PFC} = 400$ V (F.B), $V_{batt} = 1.25$ kV, $P_{out} = 10.65$ kW (a) Oscilloscope Capture (b) Power Analyzer Voltage Measurement (c) Power Analyzer Efficiency Measurement

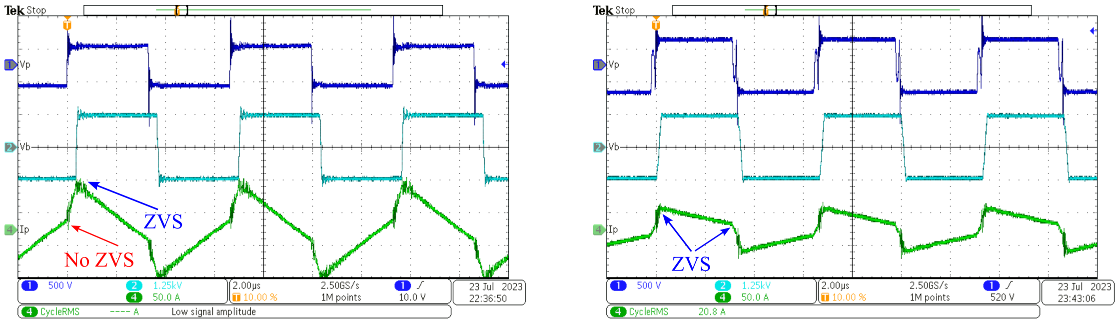

(A) (B)

FIGURE 6.5: R3L-DAB converter waveforms in the full-bridge mode when V_{batt} = 1.25 kV, P_{out} = 7.72 kW (a) V_{PFC} = 300 V (b) V_{PFC} = 300 V.

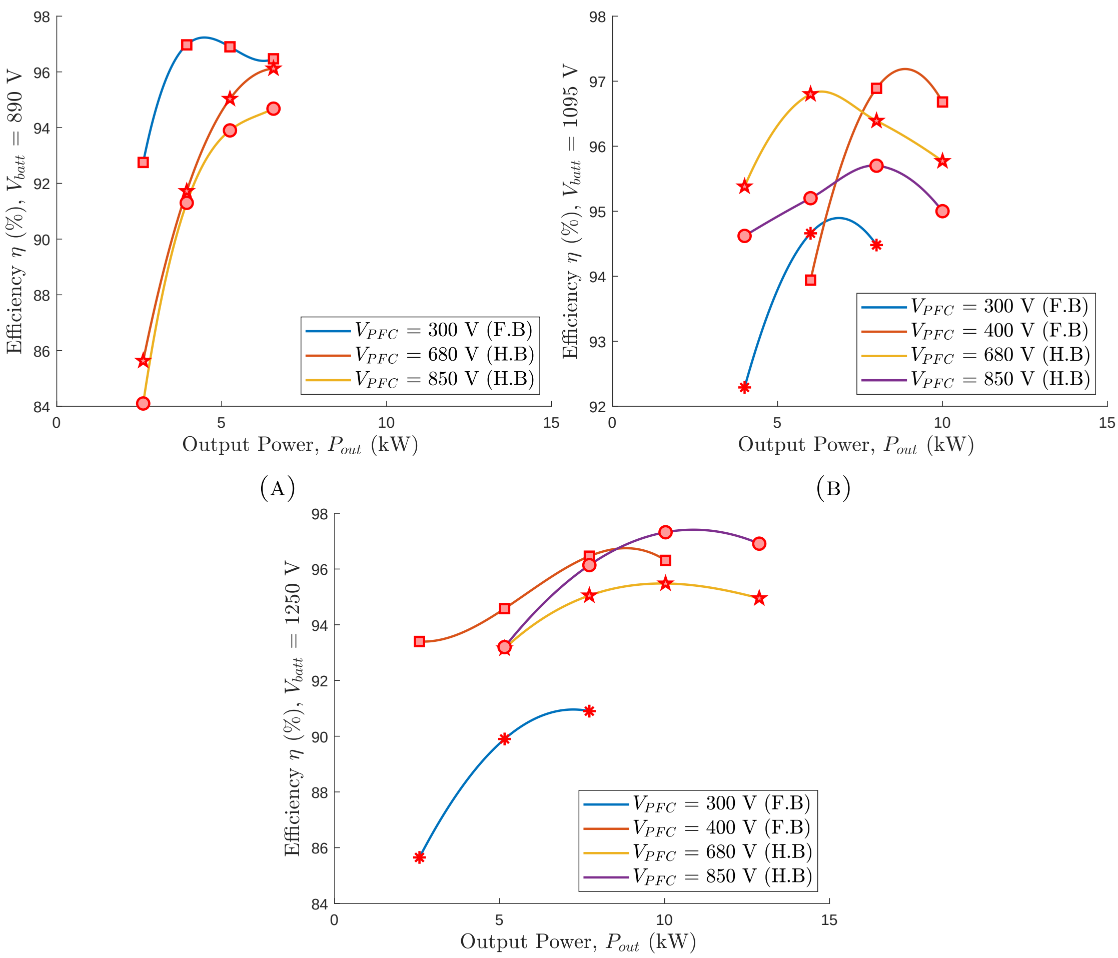

(A) (B) (C)

FIGURE 6.6: Efficiency map of the R3L-DAB converter (a) V_{batt} = 890 V (b) V_{batt} = 1095 V (c) V_{batt} = 1250 V.

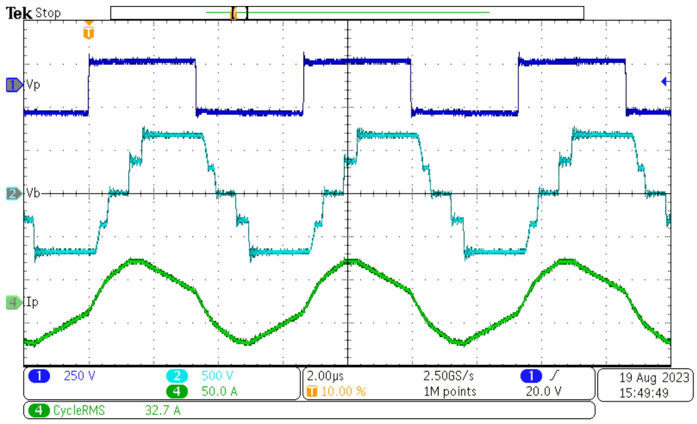

FIGURE 6.7: Five-level modulation on battery-bridge $V_{PFC} = 150$ V, $V_{batt} = 690$ V, $P_{out} = 4$ kW, $D_1 = 0.05$, $D_2 = 0.06$, $\varphi = 0.14$.

Fig. 6.1 shows the waveforms of the oscilloscope, voltage measurement of the power analyzer, and efficiency measurement of the power analyzer at the peak efficiency point of the R3L-DAB converter. Fig. 6.2, Fig. 6.3, and Fig. 6.4 show the waveforms of the oscilloscope, voltage measurement of the power analyzer, efficiency measurement of the power analyzer of varying PFC voltages at $V_{batt} =$ 1.25 kV, and measurable full-load conditions. The efficiency plots of the R3L-DAB across the input voltage, output voltage, and output power variations are shown in Fig. 6.6. It can be noted that the average efficiency of the R3L-DAB converter is approximately 95% with varying input and output voltage. The variation in input voltage does not cause detrimental impact in the converter's efficiency. The peak efficiency $\eta_{peak} = 97.32\%$ is measured when $V_{batt} = 1.25$ kV, $P_{out} = 10.38$ kW. The full-load efficiency of the R3L-DAB is 96.91%, when $P_{out} = 12.98$ kW.

Fig. 6.7 shows the five-level, mode 3 operation of the R3L-DAB converter while operating in the full-bridge mode. To clearly identify the distinction in voltage levels, the control point is $D_1 = 0.05$, $D_2 = 0.06$, $\varphi = 0.14$. $V_{PFC} = 150$ V, $V_{batt} = 690$ V, $P_{out} = 4$ kW. At this operating point, the conversion ratio $d =$

1.64, yet the R3L-DAB exhibits an efficiency of 93%. The control variables can be further optimized for minimized conduction and switching losses using numerical optimization methods [124].

Fig. 6.5 shows the operation of the R3L-DAB converter in the full-bridge mode when V_{batt} = 1.25 kV, P_{out} = 7.72 kW; (a) when V_{PFC} = 300 V (b) when V_{PFC} = 400 V. It can be observed that primary side loses ZVS when V_{PFC} = 300 V. When V_{PFC} = 400 V, the primary bridge regains ZVS. Based on the efficiency plot in Fig. 6.6(c), it can be observed that raising the V_{PFC} by 100 V results in an efficiency improvement of +5.56 %, and can be considered for system-level efficiency optimization, and synergistic regulation of the PFC DC link and DC-DC converter stage [127].

Chapter 7

Conclusions and Future Work

The thesis develops the prototype of a 15 kW Reconfigurable Three-Level Dual Active Bridge Converter for on-board charging of next-generation MHDVs with high-voltage powertrains. The prototype achieves a power density of 3.25 kW/L and a peak efficiency of 97.32 %.

Chapter 2 discusses the classification of electric vehicle charging, and its use cases. The status quo of powertrain voltages in existing BEVs has been discussed, to identify the future projection of powertrain voltage levels based on DC fast charging and on-board charging standards and their co-dependency.

Chapter 3 discusses the various architectures of on-board chargers, and their sub-systems such as the Power Factor Correction (PFC) stage and Bidirectional Isolated DC-DC Converter. A case study for comparing various topological variations of the dual active bridge converter is performed. The regulatory standards for qualification of on-board chargers are also discussed.

Chapter 4 introduces the Reconfigurable Three-Level Dual Active Bridge Converter. The operating principle of the Reconfigurable Neutral Point Clamped

(RNPC) is discussed. The modulation technique of the R3L-DAB is defined, and the steady-state analysis solving the equations of the instantaneous currents, and RMS currents is developed and the accuracy of the modeled equations is verified.

Chapter 5 focuses on the design of the R3L-DAB converter compatible for 1.25 kV on-board charging applications. The requirements for the DC-DC converter are defined. The steady-state analysis is incorporated with a power loss model to estimate the efficiency of the DC-DC converter. A design optimization procedure to choose the f_{sw}, L_k, and n based on the battery charging profile is proposed. The implementation details of the RNPC, planar transformer and the power electronics packaging are presented.

Chapter 6 shows the experimental verification of the R3L-DAB converter for comparison with simulation and modeling results. The efficiency map of the R3L-DAB converter under varying load conditions is developed.

Future Work

Apart from the original contributions made as a part of this thesis, the following research directions can be addressed in the future:

- As a part of this thesis, 2-level modulation of the R3L-DAB converter has been experimentally verified across a wide range of operation, and the two-level/five-level scheme is tested. The control variables D_1, D_2, φ can be used to reduce the RMS current stress, switching current stress of the R3L-DAB converter. Numerical optimization or analytical closed-form solutions for minimization of these parameters can aid in improvements of efficiency.

- Topological variations to reduce the switch count of the R3L-DAB converter can be explored. Some candidates such as half-bridge NPC converter or series stacked half-bridge converters can be studied to identify the cost-benefit of the converter, to make it viable for commercial applications.

- The power decoupling network for the DAB is a leakage inductance. Power decoupling via series resonant tanks/multi-resonant tanks for phase shift control, or CLLC converters for frequency control can be explored to understand deviation in efficiency.

- The analytical and power loss model can be made mature to perform numerical optimization via techniques like $\eta - \rho$ Pareto optimization, to provide the best trade-off between power density and efficiency.

Bibliography

[1] “Battery pack | tech talks | lucid motors,” *YouTube*, 2022. [Online]. Available: https://www.youtube.com/watch?v=2aDyjJ5wj64

[2] “Lucid air | specs,” *Lucid Motors*, 2021. [Online]. Available: https://www.lucidmotors.com/air/specs

[3] A. Nedelea, “Lucid air touring won’t be available until q4 2022,” *INSIDEEVs*, 2022. [Online]. Available: https://insideevs.com/news/587888/lucid-air-touring-available-q4-2022/

[4] “Battery and thermal management,” *Audi MediaCenter*, 2021.

[5] “Audi further improves the e-tron product line: Ac charging with 22 kw of power, greater driving convenience,” *Audi MediaCenter*, 2020.

[6] “Byd’s new blade battery set to redefine ev safety standards,” *BYD*, 2020.

[7] “Byd han ev specifications & configurations,” *BYD*, 2020. [Online]. Available: https://quantumauto.com.do/wp-content/uploads/2021/07/Han-EV.pdf

[8] “Sophisticated thermal management, up to 800-volt system voltage,” *Porsche newsroom*, 2021. [Online]. Available: https://media.porsche.com/mediakit/taycan/en/porsche-taycan/die-batterie

[9] "Quick, comfortable, intelligent and universal," *Porsche newsroom*, 2021. [Online]. Available: https://media.porsche.com/mediakit/taycan/en/porsche-taycan/das-laden

[10] F. Lambert, "Tesla confirms new 82 kwh battery pack in model 3, thanks to new cells," *electrek*, 2020. [Online]. Available: https://electrek.co/2020/11/10/tesla-model-3-82-kwh-battery-pack-new-cells/

[11] "Support: Onboard charger," *Tesla*, 2018. [Online]. Available: https://www.tesla.com/support/home-charging-installation/onboard-charger

[12] A. Adler, "Exclusive first ride: Nikola electric truck can turn on a dime," *FreightWaves*, 2021. [Online]. Available: https://www.freightwaves.com/news/exclusive-first-ride-nikola-electric-truck-can-turn-on-a-dime

[13] "Tesla semi," *Tesla*, 2021. [Online]. Available: https://www.tesla.com/en_ca/semi

[14] "Byd k9 40' transit," *BYD*, 2022. [Online]. Available: https://en.byd.com/wp-content/uploads/2019/07/4504-byd-transit-cut-sheets_k9-40_lr.pdf

[15] "Byd k11 60' transit," *BYD*, 2022. [Online]. Available: https://en.byd.com/bus/k11m/

[16] "Battery electric truck," *Scania*, 2022. [Online]. Available: https://www.scania.com/group/en/home/products-and-services/trucks/battery-electric-truck.html

[17] B. Bilgin, P. Magne, P. Malysz, Y. Yang, V. Pantelic, M. Preindl, A. Korobkine, W. Jiang, M. Lawford, and A. Emadi, "Making the case for electrified transportation," *IEEE Transactions on Transportation Electrification*, vol. 1, no. 1, pp. 4–17, 2015.

[18] "2021 north american trade value reaches $1.3 trillion, up 8% from pre-pandemic 2019, up 25% from 2020," 2022.

[19] I. Aghabali, J. Bauman, P. J. Kollmeyer, Y. Wang, B. Bilgin, and A. Emadi, "800-v electric vehicle powertrains: Review and analysis of benefits, challenges, and future trends," *IEEE Transactions on Transportation Electrification*, vol. 7, no. 3, pp. 927–948, 2021.

[20] "Projections for the electric truck market volume worldwide between 2018 and 2026," 2023. [Online]. Available: https://www.statista.com/statistics/1273761/electric-truck-worldwide-market-forecast/

[21] I. E. Agency. (2022) Global electric vehicle outlook 2022. [Online]. Available: https://iea.blob.core.windows.net/assets/ad8fb04c-4f75-42fc-973a-6e54c8a4449a/GlobalElectricVehicleOutlook2022.pdf

[22] H. Tu, H. Feng, S. Srdic, and S. Lukic, "Extreme fast charging of electric vehicles: A technology overview," *IEEE Transactions on Transportation Electrification*, vol. 5, no. 4, pp. 861–878, 2019.

[23] M. Etezadi-Amoli, K. Choma, and J. Stefani, "Rapid-charge electric-vehicle stations," *IEEE Transactions on Power Delivery*, vol. 25, no. 3, pp. 1883–1887, 2010.

[24] T. R. Tanim, M. G. Shirk, R. L. Bewley, E. J. Dufek, and B. Y. Liaw, "Fast charge implications: Pack and cell analysis and comparison," *Journal of Power Sources*, vol. 381, pp. 56–65, 2018.

[25] M. Yilmaz and P. T. Krein, "Review of battery charger topologies, charging power levels, and infrastructure for plug-in electric and hybrid vehicles," *IEEE Transactions on Power Electronics*, vol. 28, no. 5, pp. 2151–2169, 2013.

[26] M. Shirk and J. Wishart, "Effects of electric vehicle fast charging on battery life and vehicle performance," Idaho National Lab.(INL), Idaho Falls, ID (United States), Tech. Rep., 2015.

[27] M. Hoshi, "Electric vehicles and expectations for wide bandgap power devices," in *2016 28th International Symposium on Power Semiconductor Devices and ICs (ISPSD)*, 2016, pp. 5–8.

[28] G. E. outlook 2022, "Trends in charging infrastructure," 2022. [Online]. Available: https://www.iea.org/reports/global-ev-outlook-2022/trends-in-charging-infrastructure

[29] C. Dharmakeerthi, N. Mithulananthan, and T. Saha, "Impact of electric vehicle fast charging on power system voltage stability," *International Journal of Electrical Power & Energy Systems*, vol. 57, pp. 241–249, 2014.

[30] K. Qian, C. Zhou, and Y. Yuan, "Impacts of high penetration level of fully electric vehicles charging loads on the thermal ageing of power transformers," *International Journal of Electrical Power & Energy Systems*, vol. 65, pp. 102–112, 2015.

[31] H. Zhang, Z. Hu, Z. Xu, and Y. Song, "An integrated planning framework for different types of pev charging facilities in urban area," *IEEE Transactions on Smart Grid*, vol. 7, no. 5, pp. 2273–2284, 2016.

[32] A. G. Boulanger, A. C. Chu, S. Maxx, and D. L. Waltz, "Vehicle electrification: Status and issues," *Proceedings of the IEEE*, vol. 99, no. 6, pp. 1116–1138, 2011.

[33] ChargeHub, "Guide on how to charge your electric car with charging stations," 2022. [Online]. Available: https://chargehub.com/en/electric-car-charging-guide.html

[34] P. Morrissey, P. Weldon, and M. O'Mahony, "Future standard and fast charging infrastructure planning: An analysis of electric vehicle charging behaviour," *Energy Policy*, vol. 89, pp. 257–270, 2016.

[35] "Sae j1772-2001 sae electric vehicle conductive charge coupler," *SAE International*, 2001. [Online]. Available: https://webstore.ansi.org/Standards/SAE/sae17722001j1772

[36] "We have begun regular production of the tesla roadster," *Tesla Blog*, 2008. [Online]. Available: https://www.tesla.com/blog/we-have-begun-regular-production-tesla-roadster

[37] T. Chen, X.-P. Zhang, J. Wang, J. Li, C. Wu, M. Hu, and H. Bian, "A review on electric vehicle charging infrastructure development in the uk," *Journal of Modern Power Systems and Clean Energy*, vol. 8, no. 2, pp. 193–205, 2020.

[38] "President biden, usdot and usdoe announce $5 billion over five years for

national ev charging network, made possible by bipartisan infrastructure law," *U.S. Department of Transportation*, 2022.

[39] L. Wang, Z. Qin, T. Slangen, P. Bauer, and T. van Wijk, "Grid impact of electric vehicle fast charging stations: Trends, standards, issues and mitigation measures - an overview," *IEEE Open Journal of Power Electronics*, vol. 2, pp. 56–74, 2021.

[40] S. Tetik, "Megawatt charging system (mcs)," *CharIN*, 2022. [Online]. Available: https://www.charin.global/technology/mcs/

[41] "Megawatt charging system for electric vehicles," *SAE International*, 2021. [Online]. Available: https://www.sae.org/standards/content/j3271/

[42] "New chademo 3.0 aims to harmonize global ev quick-charging standards," *SAE International*, 2020. [Online]. Available: https://www.sae.org/news/2020/05/chademo-3.0-to-harmonize-global-ev-quick-charging-standards

[43] M. Khalid, F. Ahmad, B. K. Panigrahi, and L. Al-Fagih, "A comprehensive review on advanced charging topologies and methodologies for electric vehicle battery," *Journal of Energy Storage*, vol. 53, p. 105084, 2022.

[44] "Ul 2580: Batteries for use in electric vehicles," *Underwriters Laboratories*, vol. 3, 2022.

[45] D. Marcos, J. Perez, P. Zubizarreta, M. Garmendia, I. P. de Arenaza, J. Crego, and J. A. Cortajarena, "A safety concept for an automotive lithium-based battery management system," in *2019 Electric Vehicles International Conference (EV)*, 2019, pp. 1–6.

[46] "Iso 26262-2:2018, road vehicles — functional safety — part 2: Management of functional safety," *International Organization for Standardization*, vol. 2, 2018.

[47] "Amc1411-q1: Automotive, 2-v input, precision voltage sensing reinforced isolated amplifier with high cmti," in *Texas Instruments*, 2021. [Online]. Available: https://www.ti.com/product/AMC1411-Q1

[48] "High-voltage contactors: Safely connect and disconnect," *TE Connectivity*.

[49] L. Saw, A. A. O. Tay, and L. W. Zhang, "Thermal management of lithium-ion battery pack with liquid cooling," in *2015 31st Thermal Measurement, Modeling & Management Symposium (SEMI-THERM)*, 2015, pp. 298–302.

[50] G. Bauer, C.-W. Hsu, M. Nicholas, and N. Lutsey, "Charging up america: Assessing the growing need for u.s. charging infrastructure through 2030," 07 2021.

[51] "Sae j1772-2017 sae electric vehicle conductive charge coupler," *SAE International*, 2017. [Online]. Available: https://www.sae.org/standards/content/j1772_201710/

[52] "Tesla mobile connector," in *Tesla*. [Online]. Available: https://www.tesla.com/support/home-charging-installation/mobile-connector

[53] "Iec 62196-2:2016, plugs, socket-outlets, vehicle connectors and vehicle inlets - conductive charging of electric vehicles - part 2: Dimensional compatibility and interchangeability requirements for a.c. pin and contact-tube accessories," *International Electrotechnical Commission*, 2016. [Online].

Available: https://webstore.iec.ch/publication/24204

[54] "Gb/t 20234.1-2015: Connection set for conductive charging of electric vehicles – part 1: General requirements," *Standardization Administration of China*, 2015.

[55] "Sae j3068-2018 electric vehicle power transfer system using a three-phase capable coupler," *SAE International*, 2018. [Online]. Available: https://www.sae.org/standards/content/j3068_201804

[56] "Charging and the wunderbox | tech talks | lucid motors," *YouTube*, 2022. [Online]. Available: https://www.youtube.com/watch?v=Ga0qMqUG2X4

[57] "The challenge of range anxiety from dc fast-charging incompatibility." [Online]. Available: https://www.vicorpower.com/industries-and-innovations/automotive/dc-fast-charging

[58] M. A. H. Rafi and J. Bauman, "A comprehensive review of dc fast-charging stations with energy storage: Architectures, power converters, and analysis," *IEEE Transactions on Transportation Electrification*, vol. 7, no. 2, pp. 345–368, 2021.

[59] S. Srdic and S. Lukic, "Toward extreme fast charging: Challenges and opportunities in directly connecting to medium-voltage line," *IEEE Electrification Magazine*, vol. 7, no. 1, pp. 22–31, 2019.

[60] "Sae j3105-2020 electric vehicle power transfer system using conductive automated connection devices," *SAE International*, 2020. [Online]. Available: https://www.sae.org/standards/content/j3105_202001/

[61] T. Bohn and H. Glenn, "A real world technology testbed for electric vehicle smart charging systems and pev-evse interoperability evaluation," in *2016 IEEE Energy Conversion Congress and Exposition (ECCE)*, 2016, pp. 1–8.

[62] J. Parmar, P. Das, and S. M. Dave, "Study on demand and characteristics of parking system in urban areas: A review," *Journal of Traffic and Transportation Engineering (English Edition)*, vol. 7, no. 1, pp. 111–124, 2020, special Issue: Modeling and detecting traffic dynamics: granular, pedestrian and vehicular flow.

[63] "Tesla spotted using mobile powerpacks at first tesla semi megacharger station," *electrek*, 2022. [Online]. Available: https://electrek.co/2022/01/10/tesla-spotted-mobile-powerpacks-first-tesla-semi-megacharger-station/

[64] S. Jaman, B. Verbrugge, O. H. Garcia, M. Abdel-Monem, B. Oliver, T. Geury, and O. Hegazy, "Development and validation of v2g technology for electric vehicle chargers using combo ccs type 2 connector standards," *Energies*, vol. 15, no. 19, 2022. [Online]. Available: https://www.mdpi.com/1996-1073/15/19/7364

[65] B. Singh, B. Singh, A. Chandra, K. Al-Haddad, A. Pandey, and D. Kothari, "A review of three-phase improved power quality ac-dc converters," *IEEE Transactions on Industrial Electronics*, vol. 51, no. 3, pp. 641–660, 2004.

[66] J. W. Kolar and T. Friedli, "The essence of three-phase pfc rectifier systems—part i," *IEEE Transactions on Power Electronics*, vol. 28, no. 1, pp. 176–198, 2013.

[67] A. Kouchaki and M. Nymand, "High efficiency three-phase power factor

correction rectifier using sic switches," in *2017 19th European Conference on Power Electronics and Applications (EPE'17 ECCE Europe)*, 2017, pp. P.1–P.10.

[68] R. Wang, S. Yuan, C. Liu, D. Guo, and X. Shao, "A three-phase dual-output t-type three-level converter," *IEEE Transactions on Power Electronics*, vol. 38, no. 2, pp. 1844–1859, 2023.

[69] "Tida-01606: 10-kw, bidirectional three-phase three-level (t-type) inverter and pfc reference design," 2018. [Online]. Available: https://www.ti.com/tool/TIDA-01606

[70] T. Friedli, M. Hartmann, and J. W. Kolar, "The essence of three-phase pfc rectifier systems—part ii," *IEEE Transactions on Power Electronics*, vol. 29, no. 2, pp. 543–560, 2014.

[71] J. C. Hernandez, L. P. Petersen, and M. A. E. Andersen, "A comparison between boundary and continuous conduction modes in single phase pfc using 600v range devices," in *2015 IEEE 11th International Conference on Power Electronics and Drive Systems*, 2015, pp. 1019–1023.

[72] Y.-S. Kim, W.-Y. Sung, and B.-K. Lee, "Comparative performance analysis of high density and efficiency pfc topologies," *IEEE Transactions on Power Electronics*, vol. 29, no. 6, pp. 2666–2679, 2014.

[73] M. Schweizer and J. W. Kolar, "Design and implementation of a highly efficient three-level t-type converter for low-voltage applications," *IEEE Transactions on Power Electronics*, vol. 28, no. 2, pp. 899–907, 2013.

[74] F. E. U. Reis, R. P. Torrico-Bascopé, F. L. Tofoli, and L. D. Santos Bezerra, “Bidirectional three-level stacked neutral-point-clamped converter for electric vehicle charging stations,” *IEEE Access*, vol. 8, pp. 37 565–37 577, 2020.

[75] L. Zhang, X. Yuan, X. Wu, C. Shi, J. Zhang, and Y. Zhang, “Performance evaluation of high-power sic mosfet modules in comparison to si igbt modules,” *IEEE Transactions on Power Electronics*, vol. 34, no. 2, pp. 1181–1196, 2019.

[76] “Tida-010210: 11-kw, bidirectional, three-phase anpc based on gan reference design,” 2022. [Online]. Available: https://www.ti.com/tool/TIDA-010210

[77] M. Safayatullah, M. T. Elrais, S. Ghosh, R. Rezaii, and I. Batarseh, “A comprehensive review of power converter topologies and control methods for electric vehicle fast charging applications,” *IEEE Access*, vol. 10, pp. 40 753–40 793, 2022.

[78] Q.-X. Guan, C. Li, Y. Zhang, S. Wang, D. D. Xu, W. Li, and H. Ma, “An extremely high efficient three-level active neutral-point-clamped converter comprising sic and si hybrid power stages,” *IEEE Transactions on Power Electronics*, vol. 33, no. 10, pp. 8341–8352, 2018.

[79] M. Najjar, A. Kouchaki, J. Nielsen, R. Dan Lazar, and M. Nymand, “Design procedure and efficiency analysis of a 99.3% efficient 10 kw three-phase three-level hybrid gan/si active neutral point clamped converter,” *IEEE Transactions on Power Electronics*, vol. 37, no. 6, pp. 6698–6710, 2022.

[80] “Ul 2202: Standard for electric vehicle (ev) charging system equipment,”

Underwriter Laboratories, 2018. [Online]. Available: https://www.shopulstandards.com/ProductDetail.aspx?UniqueKey=20342

[81] M. Jahnes, L. Zhou, M. Eull, W. Wang, and M. Preindl, "Design of a 22kw transformerless ev charger with v2g capabilities and peak 99.5% efficiency," *IEEE Transactions on Industrial Electronics*, pp. 1–10, 2022.

[82] S. Mukherjee, J. M. Ruiz, and P. Barbosa, "A high power density wide range dc–dc converter for universal electric vehicle charging," *IEEE Transactions on Power Electronics*, vol. 38, no. 2, pp. 1998–2012, 2023.

[83] R. A. Friedemann, F. Krismer, and J. W. Kolar, "Design of a minimum weight dual active bridge converter for an airborne wind turbine system," in *2012 Twenty-Seventh Annual IEEE Applied Power Electronics Conference and Exposition (APEC)*, 2012, pp. 509–516.

[84] J. W. Kolar, T. Friedli, F. Krismer, A. Looser, M. Schweizer, R. A. Friedemann, P. K. Steimer, and J. B. Bevirt, "Conceptualization and multiobjective optimization of the electric system of an airborne wind turbine," *IEEE Journal of Emerging and Selected Topics in Power Electronics*, vol. 1, no. 2, pp. 73–103, 2013.

[85] M. Moonem and H. Krishnaswami, "Analysis and control of multi-level dual active bridge dc-dc converter," in *2012 IEEE Energy Conversion Congress and Exposition (ECCE)*, 2012, pp. 1556–1561.

[86] M. A. Moonem, C. L. Pechacek, R. Hernandez, and H. Krishnaswami, "Analysis of a multilevel dual active bridge (ml-dab) dc-dc converter using

symmetric modulation," *Electronics*, vol. 4, no. 2, pp. 239–260, 2015. [Online]. Available: https://www.mdpi.com/2079-9292/4/2/239

[87] Y. Xuan, X. Yang, W. Chen, T. Liu, and X. Hao, "A three-level dual-active-bridge converter with blocking capacitors for bidirectional electric vehicle charger," *IEEE Access*, vol. 7, pp. 173 838–173 847, 2019.

[88] A. Agarwal, S. K. Rastogi, and S. Bhattacharya, "Performance evaluation of two-level to three-level three-phase dual active bridge (2l-3l dab3)," in *2022 IEEE Applied Power Electronics Conference and Exposition (APEC)*, 2022, pp. 361–368.

[89] "22kw bi-directional high efficiency active front end (afe) converter." [Online]. Available: https://www.wolfspeed.com/products/power/reference-designs/crd-22dd12n/

[90] "25kw bi-directional active front end (afe) ac-dc converter reference design." [Online]. Available: https://www.wolfspeed.com/products/power/reference-designs/crd25ad12n-fmc/

[91] "11 kw sic bi-directional dc/dc converter board for ev charging and ess applications." [Online]. Available: https://www.infineon.com/cms/en/product/evaluation-boards/ref-dab11kizsicsys/

[92] "22kw bi-directional high efficiency dc/dc converter." [Online]. Available: https://www.wolfspeed.com/products/power/reference-designs/crd-22dd12n/

[93] M. J. Kasper, J. A. Anderson, G. Deboy, Y. Li, M. Haider, and J. W. Kolar, "Next generation gan-based architectures: From 240w usb-c adapters to 11kw ev on-board chargers with ultra-high power density and wide output voltage range," in *PCIM Europe 2022; International Exhibition and Conference for Power Electronics, Intelligent Motion, Renewable Energy and Energy Management*, 2022, pp. 1–10.

[94] "On-board charger." [Online]. Available: https://innolectric.ag/on-board-charger-2-2/?lang=en

[95] "On-board charger - hpc series." [Online]. Available: https://innolectric.ag/on-board-charger-2-2/?lang=en

[96] "Ieee 519-2014 ieee recommended practice and requirements for harmonic control in electric power systems," *IEEE*, 2014. [Online]. Available: https://standards.ieee.org/ieee/519/3710/

[97] V. Rodriguez, "Automotive component emc testing: Cispr 25, iso 11452–2 and equivalent standards," *IEEE Electromagnetic Compatibility Magazine*, vol. 1, no. 1, pp. 83–90, 2012.

[98] P. S. Crovetti and F. Fiori, "A critical assessment of the closed-loop bulk current injection immunity test performed in compliance with iso 11452-4," in *2010 IEEE International Symposium on Electromagnetic Compatibility*, 2010, pp. 177–182.

[99] A. Hofer and S. Cecil, "Numerical simulation of field distribution regarding automotive component emc-testing according to iso 11452–2," in *2022 International Symposium on Electromagnetic Compatibility – EMC Europe*, 2022,

pp. 399–404.

[100] N. A. Thomson, Y. Xiu, and E. Rosenbaum, "Soft-failures induced by system-level esd," *IEEE Transactions on Device and Materials Reliability*, vol. 17, no. 1, pp. 90–98, 2017.

[101] "Iso 15118-1:2013, road vehicles — vehicle to grid communication interface — part 1: General information and use-case definition," *International Organization for Standardization*, vol. 1, 2013.

[102] S. Mukherjee, A. Kumar, and S. Chakraborty, "Comparison of dab and llc dc–dc converters in high-step-down fixed-conversion-ratio (dcx) applications," *IEEE Transactions on Power Electronics*, vol. 36, no. 4, pp. 4383–4398, 2021.

[103] M. Kheraluwala, R. Gascoigne, D. Divan, and E. Baumann, "Performance characterization of a high-power dual active bridge dc-to-dc converter," *IEEE Transactions on Industry Applications*, vol. 28, no. 6, pp. 1294–1301, 1992.

[104] N. Keshmiri, D. Wang, B. Agrawal, R. Hou, and A. Emadi, "Current status and future trends of gan hemts in electrified transportation," *IEEE Access*, vol. 8, pp. 70 553–70 571, 2020.

[105] "Tesla model 3 power conversion system," 2018. [Online]. Available: https://www.youtube.com/watch?v=3ARHdRwfxjY

[106] J. W. Kolar, J. Biela, S. Waffler, T. Friedli, and U. Badstuebner, "Performance trends and limitations of power electronic systems," in *2010 6th*

International Conference on Integrated Power Electronics Systems, 2010, pp. 1–20.

[107] N. Noroozi, A. Emadi, and M. Narimani, "Performance evaluation of modulation techniques in single-phase dual active bridge converters," *IEEE Open Journal of the Industrial Electronics Society*, vol. 2, pp. 410–427, 2021.

[108] I. Voss, T. Aichinger, T. Basler, P. Friedrichs, and R. Rupp, "Reliability and ruggedness of sic trench mosfets for long-term applications in humid environment," in *PCIM Europe 2018; International Exhibition and Conference for Power Electronics, Intelligent Motion, Renewable Energy and Energy Management*, 2018, pp. 1–4.

[109] "Discrete silicon carbide mosfets." [Online]. Available: https://www.wolfspeed.com/products/power/sic-mosfets

[110] "Sic fets selector guide." [Online]. Available: https://unitedsic.com/group/sic-fets/

[111] "Sic mosfets." [Online]. Available: https://www.rohm.com/products/sic-power-devices/sic-mosfet#easyPartFinder

[112] "Silicon carbide coolsic™ mosfets." [Online]. Available: https://www.rohm.com/products/sic-power-devices/sic-mosfet#easyPartFinder

[113] "Discrete silicon carbide mosfets." [Online]. Available: https://genesicsemi.com/sic-mosfet/

[114] R. Pradhan, M. Narimani, and A. Emadi, "Converter topology comparison for a two-stage level-2 onboard charger in 800-v ev powertrains," in *IECON*

2022 – 48th Annual Conference of the IEEE Industrial Electronics Society, 2022, pp. 1–6.

[115] "Power quality: Energy efficiency reference." [Online]. Available: https://www.bchydro.com/content/dam/BCHydro/customer-portal/documents/power-smart/business/programs/power-quality-reference-guide.pdf

[116] O. Zayed, A. Elezab, A. Abuelnaga, and M. Narimani, "A dual-active bridge converter with a wide output voltage range (200-1000 v) for ultra-fast dc-connected ev charging stations," *IEEE Transactions on Transportation Electrification*, pp. 1–1, 2022.

[117] V. Cirimele, R. Torchio, J. L. Villa, F. Freschi, P. Alotto, L. Codecasa, and L. D. Rienzo, "Uncertainty quantification for sae j2954 compliant static wireless charge components," *IEEE Access*, vol. 8, pp. 171 489–171 501, 2020.

[118] J. Laskowski, "Sae tir j2954/2 paves the way for heavy-duty ev charging without a plug & static and dynamic wireless power transfer," *SAE International*, 2022. [Online]. Available: https://www.sae.org/news/press-room/2022/12/sae-2022-j2954-2

[119] B. Zhao, Q. Song, J. Li, W. Liu, G. Liu, and Y. Zhao, "High-frequency-link dc transformer based on switched capacitor for medium-voltage dc power distribution application," *IEEE Transactions on Power Electronics*, vol. 31, no. 7, pp. 4766–4777, 2016.

[120] V. Sidorov, A. Chub, D. Vinnikov, and F. Z. Peng, "Survey of topology morphing control techniques for performance enhancement of galvanically

isolated dc-dc converters," *IEEE Open Journal of the Industrial Electronics Society*, vol. 3, pp. 751–777, 2022.

[121] A. Poorfakhraei, M. Narimani, and A. Emadi, "Improving power density of a three-level anpc structure using the electro-thermal model of inverter and a modified spwm technique," *IEEE Open Journal of Power Electronics*, vol. 3, pp. 741–754, 2022.

[122] H. Karneddi and D. Ronanki, "Reconfigurable battery charger with a wide voltage range for universal electric vehicle charging applications," *IEEE Transactions on Power Electronics*, pp. 1–5, 2023.

[123] R. Baranwal, D. Patil, Z. Zhang, L. Qian, M. Horejs, and G. Zhu, "Resonant power converter for wide voltage switching," Sep. 8 2022, US Patent App. 17/632,020.

[124] A. Filba-Martinez, S. Busquets-Monge, J. Nicolas-Apruzzese, and J. Bordonau, "Operating principle and performance optimization of a three-level npc dual-active-bridge dc–dc converter," *IEEE Transactions on Industrial Electronics*, vol. 63, no. 2, pp. 678–690, 2016.

[125] Y. Yan, H. Gui, and H. Bai, "Complete zvs analysis in dual active bridge," *IEEE Transactions on Power Electronics*, vol. 36, no. 2, pp. 1247–1252, 2021.

[126] D. Zhang, M. Guacci, M. Haider, D. Bortis, J. W. Kolar, and J. Everts, "Three-phase bidirectional buck-boost current dc-link ev battery charger featuring a wide output voltage range of 200 to 1000v," in *2020 IEEE Energy Conversion Congress and Exposition (ECCE)*, 2020, pp. 4555–4562.

[127] Y. Li, J. A. Anderson, M. Haider, J. Schäfer, J. Miniböck, J. Huber, G. Deboy, and J. W. Kolar, "Optimal synergetic operation and experimental evaluation of an ultra-compact gan-based three-phase 10 kw ev charger," *IEEE Transactions on Transportation Electrification*, pp. 1–1, 2023.